On Mars thermosphere, ionosphere and exosphere: 3D computational study of suprathermal particles

by

Arnaud Valeille

A dissertation submitted in partial fulfillment
of the requirements for the degrees of
Doctor of Philosophy
(Atmospheric and Space Science and Scientific Computing)
in the University of Michigan
2009

Doctoral Committee:

Research Professor Michael R. Combi, Chair
Research Professor Stephen W. Bougher
Professor Edward W. Larsen
Professor Andrew F. Nagy

"*The time will come when diligent research over long periods will bring to light things which now lie hidden. A single lifetime, even though entirely devoted to the sky, would not be enough for the investigation of so vast a subject... And so this knowledge will be unfolded only through long successive ages. There will come a time when our descendents will be amazed that we did not know things that are so plain to them… Many discoveries are reserved for the ages still to come, when the memory of us will have been effaced. Our universe is a sorry little affair unless it has in it something for every age to investigate… Nature does not reveal her mysteries once and for all.*"

- Seneca, Natural Questions, Book 7, First century.

2009

A mes parents,

Marie-Louise et Georges

Acknowledgements

First and foremost, I would like to thank my dissertation committee chair and academic advisor, Prof. Mike Combi. His continuous guidance, support, encouragement have made this work possible. I am grateful to him for giving me the intellectual freedom and challenge to follow two different Master programs at the same time in the Atmospheric and Space Science department (AOSS), College of Engineering and in the Mathematics department, College of Literature Science and Art (LSA), both at the University of Michigan. These additional interdisciplinary classes were highly beneficial and allowed me to follow this joint PhD program in both Space Science and Scientific Computing.

I would like to thank my dissertation committee, Prof. Mike Combi, Prof. Steve Bougher, Prof. Andy Nagy and Prof. Edward Larsen. Their careful reading, expert suggestions and valuable comments have strongly improved this thesis.

I am very thankful to Prof. Steve Bougher for sharing his wisdom with me, for his very detailed reviews and pertinent comments. I believe that we had a very rich collaboration in the three and half years I spent in the department and I learned a lot from him.

I would like to express my admiration for Prof. Andy Nagy. He has more than forty years of experience in both theoretical and experimental studies of planetary upper atmospheres and worked as principal and co-investigator of a variety of instruments flown on pioneering missions to space. I feel extremely lucky to have worked with him. He has permitted an international exchange with my French school *Supaero* and allows me to be part of today's one of the best Space Science program in the world.

This study of the Martian upper atmosphere would not have been possible without the use of the solid work on the general core created by Valeriy Tenishev and previously

used for simulations around comets. Valeriy helped me substantially on using and modifying his code and on its adaptation to Mars.

I was delighted to meet the scientists from whom Space Science benefits so much, and I would like to thank them for their inspiring discussions. These chances came from the many opportunities I had to attend scientific conferences in different part of North America, including: Spring AGU 2007 (Acapulco, Mexico), DPS 2007 (Orlando, FL, USA), Fall AGU 2007 (San Francisco, CA, USA), COSPAR 2008 (Montreal, Canada), DPS 2008 (Ithaca, NY, USA) and Fall AGU 2008 (San Francisco, CA, USA).

This thesis is mostly built on four papers that benefited from excellent reviews of seven reviewers specialized in the field. I would like to thank them for their assistance in evaluating these papers.

For funding this work, I gratefully acknowledge the National Aeronautics and Space Administration (NASA). Support for this work comes from the NASA Mars Fundamental Research grant NNG05GL80G and the Mars Data Analysis Program grant NNX07AO84G. Computations were performed on the massively parallel Columbia computer at the High-End Computing (HEC) Program's NASA Advanced Supercomputing (NAS) Facility.

Finally, I would like to thank the French elite *Classes préparatoires* (equivalent of first years of undergraduate) education system for its cold scientific rigor and the US graduate education system for its supportive research freedom. I feel extremely lucky having both experiences.

Foreword

The meaning of life is deeply mixed with the scientific and philosophical conceptions of survival and happiness. At the end of the 20th century, based upon insight gleaned from the gene-centered view of evolution, biologists George C. Williams, Richard Dawkins, David Haig, among others, conclude that if there is a primary function to life, it is the replication of DNA and the survival of one's genes. Attempts to find meaning in subjective sensory experience may involve a focus on immediate experience and gratification, as in various forms of hedonism or *carpe diem* philosophies, or in long-term efforts at the creation of an aesthetically pleasing life, as with Epicureanism. If the purpose of life involves these two concepts of seeking happiness and being useful to the next generation, then the fundamental human essence, feeling and motivation, that is the hunger for knowledge, could be seen as the main purpose of its existence. Therefore, driven by its insatiable curiosity, mankind is invariably confronted to the metaphysical questions: ‘What is the origin of life?’ and ‘How the universe was created?’.

Table of Contents

List of Figures

List of Tables

List of Abbreviations

AL	Aphelion, low solar activity
ALP	Aphelion, low solar activity, polar meridian
AU	Astronomical unit
CE	Charge exchange
DR	Dissociative recombination
DSMC	Direct Simulation Monte Carlo
EH	Equinox, high solar activity
EHP	Equinox, high solar activity, polar meridian
EI	electron impact ionization
EL	Equinox, low solar activity
ELE	Equinox, low solar activity, equator
ELP	Equinox, low solar activity, polar meridian
ENA	Energetic Neutral Atoms
EUV	Extreme ultraviolet
IR	Infra Red
MEX	Mars Express
MGCM	Mars General Circulation Model
MTGCM	Mars Thermosphere General Circulation Model
MGS	Mars Global Surveyor
NASA	National Aeronautics and Space Administration
NIR	Near Infra Red
NLTE	Non-Local Thermodynamic Equilibrium
PH	Perihelion, high solar activity
PHP	Perihelion, high solar activity, polar meridian
PI	Photoionization
PL	Perihelion, low solar activity
SIDC	Solar Influences Data Analysis Center
SZA	Solar Zenith Angle
TES	Thermal Emission Spectrometer
UV	Ultraviolet

ABSTRACT

Unlike Earth and Venus, Mars with a weak gravity allows an extended corona of hot light species and the escape of its lighter and hotter constituents in its exosphere. Being the most important reaction, the dissociative recombination of O_2^+ is responsible for most of the production of hot atomic oxygen deep in the dayside thermosphere/ionosphere. The physics of the Martian upper atmosphere is complicated by the change in the flow regime from a collisional to collisionless domain with increasing altitude. Previous studies of the Martian hot corona used simple extrapolations of 1D thermospheric/ionospheric parameters and could not account for the full effects of realistic conditions, which are shown here to be of significant influence on the exosphere both close to and far away from the exobase.

In this work, a 3D physical and chemical kinetic model of the Martian upper atmosphere has been computed and employed in combination with various thermospheric/ionospheric inputs to present, for the first time, a complete 3D self-consistent description of the exosphere via a global probabilistic technique.

A 3D analysis and shape of the Martian hot corona is provided, along with density and temperature profiles of cold and hot constituents as functions of position on the planet (altitude, latitude and longitude). In addition, several of the limiting cases spanning spatial and temporal domains are examined. The variations in the Martian upper atmosphere over modern and past conditions are investigated. These characteristic conditions lead to significant variations in the thermosphere/ionosphere temperatures, dynamical heating, winds and ion/neutral density distributions, which in turn affect the exosphere general structure, the hot corona shape, and the ion/neutral loss rates on all timescales.

Spatial, seasonal, solar cycle and evolutionary driven variations, although exhibiting very different timescales, are all shown to exert an influence on the atmospheric loss of the same order. Atmospheric loss and ion production, calculated locally all around the planet, provide valuable information for plasma models, refining the understanding of the ion loss, atmospheric sputtering, and interaction with the solar wind in general.

Chapter I
Introduction

The formation of the Solar System is estimated to have begun 4.6 billion years (Gyr) ago with the gravitational collapse of a small part of a giant molecular cloud. Most of the collapsing mass collected in the centre, forming the Sun, while the rest flattened into a protoplanetary disc, out of which the planets, moons, asteroids, and other small Solar System bodies formed.

The Solar System consists of the Sun and those celestial objects bound to it by gravity. Four terrestrial inner planets (Mercury, Venus, Earth, and Mars) and four gas giant outer planets (Jupiter, Saturn, Uranus, and Neptune) are separated by the asteroid belt (see Figure 1.1). The four inner or terrestrial planets have dense, rocky compositions, few or no moons, and no ring systems. They are composed largely of minerals with high melting points, such as the silicates, which form their crusts and mantles, and metals, such as iron and nickel, which form their cores. Three of the four inner planets (Venus, Earth and Mars) have substantial atmospheres; all have impact craters and tectonic surface features, such as rift valleys and volcanoes.

Mars (1.5 AU) is smaller than Earth and Venus (0.107 Earth masses). It possesses a tenuous atmosphere of mostly carbon dioxide (CO_2). Mars has a rocky icy surface with frozen CO_2 on the caps. Its surface, peppered with vast volcanoes, such as *Olympus Mons* and rift valleys, such as *Valles Marineris*, shows geological activity that may have persisted until very recently. Its red color comes from rust in its iron-rich soil (Figure 1.2). Mars has two tiny natural satellites (Deimos and Phobos) thought to be captured asteroids.

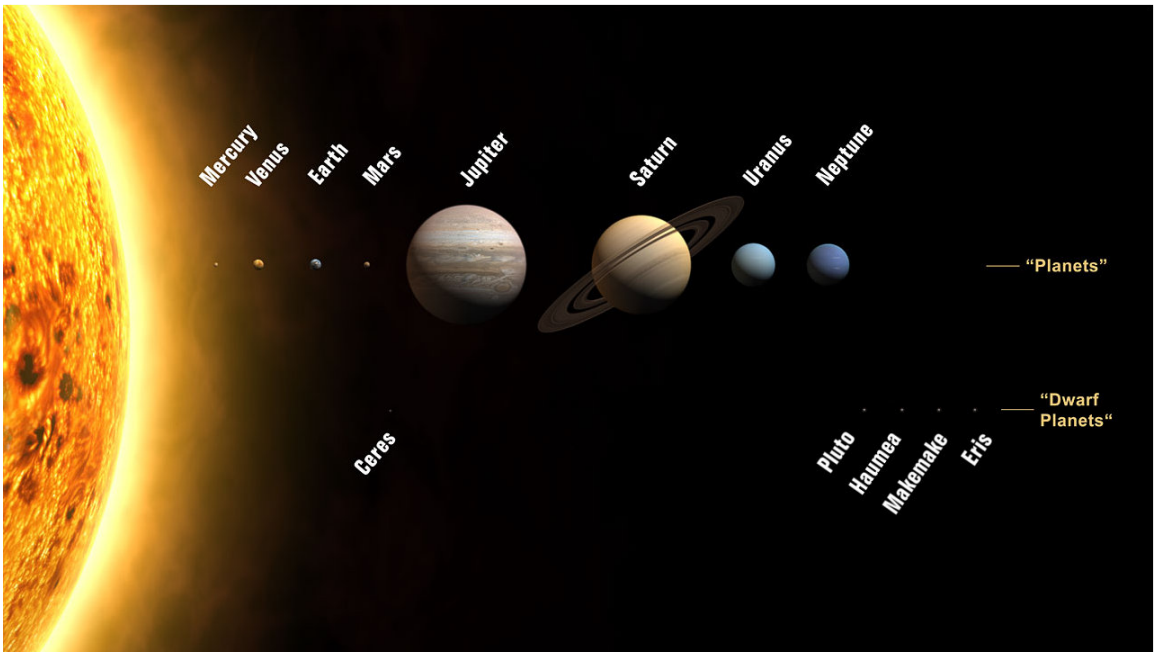

Figure 1.1. Planets and dwarf planets of the Solar System. Sizes are to scale, but relative distances from the Sun are not [Source: NASA; http://sse.jpl.nasa.gov/planets/index.cfm].

Mars remains a high-priority target for exobiological investigations. The reason for this is the possibility that Mars and Earth experienced similar climatic conditions early in their history and that because life started on Earth, it might also have started on Mars. Then as the planets evolved, life flourished on Earth but became extinct on Mars [*Haberle* 1998].

Today Mars is a dry desert world, despite some signs that water may have once flowed freely across its surface. Where did the water go? Unlike Venus, Mars with a weak gravity allows an extended corona of hot light species and the escape of its lighter constituents, in its exosphere.

The Martian exosphere plays, therefore, a crucial role in the global escape of the Martian atmosphere, and thus to the history of water on Mars [*Chassefière and Leblanc* 2004; *Leblanc et al.* 2006]. However, even today the information about the hot species that form the Martian corona of is very limited because of the lack of observational data, the only *in situ* measurements coming from the Viking 1 & 2 mission descents of 1976. Since then, a number of theoretical quantitative works have been reported in an attempt to describe its extended hot atomic corona. In the last 30 years, a great improvement in

the computational simulations has been made and the models tend to be more complex and accurate.

This work presents the first self-consistent 3D description of the Mars thermosphere and exosphere and studies its variation through seasons and solar activity. The evolution of the upper atmosphere (*i.e.* upper thermosphere and exosphere) is also investigated and allows an estimate of the global loss of water over Martian history. Much of the work in this thesis appears in two papers already accepted for publication in a special issue of the refereed planetary journal *Icarus* [*Valeille et al.* 2009a, 2009b] and in two papers that have been submitted for publication in the *Journal for Geophysical Research* [*Valeille et al.* 2009c, 2009d].

Figure 1.2. View of Mars from Hubble Space Telescope on June 26, 2001. The colors have been carefully balanced to give a realistic view of Mars' hues as they might appear through a telescope [Source: NASA Image PIA03154; Image Credit: NASA and The Hubble Heritage Team (STScI/AURA); Acknowledgment: J. Bell (Cornell U.)].

I.1. Past studies

Originally the hot Martian corona was modeled using Venus as an analogy, and those simulations were extended to Mars [*Nagy et al.* 1981; *Nagy and Cravens* 1988; *Nagy et al.* 1990; *Hodges* 2000]. The pioneering work on the hot corona and their role in the solar wind interaction with Mars [*Nagy et al.* 1988; *Nagy and Cravens*, 1988; *Ip* 1990; *Nagy et al.* 1990; *Lammer and Bauer* 1991; *Hodges* 1994; *Fox and Hac* 1997; *Kim et al.* 1998], considered the exobase as a theoretical level delimitating the collision-dominated thermosphere from the collisionless exosphere in order to take into account the change in collision regime in the flow. Calculations were conducted separately for each region in 1D spherical symmetry. The hot species energy distribution, computed by a two-stream transport model [*Nagy and Banks* 1970] in the thermosphere, was applied as a boundary condition at the exobase to calculate the oxygen density profile in the exosphere based on the Liouville equation [*Chamberlain* 1963].

The main limitation of these models is that they assume a strict separation between collision and collisionless domains, disregarding the collision transitional domain (between the collision-dominated thermosphere and the collisionless exosphere), where the momentum exchange within the flow is still important but the collision frequency is not high enough to maintain equilibrium. Moreover the escape fluxes generated do not include the exospheric production of hot species and their collisions with the thermospheric and exospheric background species, which account for a non-negligible part of the total escape rate [*Hodges* 2000; *Valeille et al.* 2009a].

A self-consistent description of the Martian upper atmosphere requires construction of a global physical model that accounts for kinetic processes of both the collisional upper thermosphere and collisionless exosphere, but also in the collision transitional domain. Among the most recent proposed approaches, *Hodges* [2000] considered a thick atmospheric region where hot species are produced and collide with the background species before reaching the collisionless exospheric region beyond.

Taking into account the change in the collision regime in the flow, a number of theoretical quantitative works have been reported over the past ten years in an attempt to describe the extended hot atomic corona in 1D spherical symmetry [*Lammer et al.* 2000; *Nagy et al.* 2001; *Krestyanikova and Shematovitch* 2005; *Cipriani et al.* 2007]. However,

those studies are most often specific to the subsolar point, cannot account for the important diurnal variations, and therefore are inherently constrained to a local description of the altitude profile.

Keeping these considerations in mind, a few studies extended their 1D spherically symmetric thermosphere inputs to higher dimensions by simple extrapolation. Distributions varying as a cosine function of Solar Zenith Angle (SZA) were first assumed to extend the inputs to 2D axisymmetry with respect to the Mars-Sun axis [*Kim et al.* 2001]. The inclusion of planetary rotation or diurnal tides added some 3D influences to the results [*Hodges* 2000; *Chaufray et al.* 2007]. However, while the improvements in the exosphere models were considerable, the spatial and temporal distribution of the results still presented the same limitations that were inherent in the 1D thermosphere inputs (taken from independent, and therefore non-consistent, studies), upon which they were based [*Hanson et al.* 1977; *Nier and Mc Elroy* 1977; *Zhang et al.* 1990; *Fox* 1993a; *Kim et al.* 1998; *Krasnopolsky* 2002].

It has been extensively demonstrated [*e.g. Bell et al.* 2007; *Bougher et al.* 2000, 2006, 2008, 2009a] that the thermosphere exhibits diurnal patterns (such as dynamical effects and abrupt changes in the ionosphere structure), as well as local variations (temperature and wind distributions, planet rotation, polar warming, hemispheric asymmetries) that cannot be treated by simple extrapolation of a 1D thermosphere.

Processes that shape the exosphere and the Martian hot corona originate deep in the thermosphere/ionosphere and interact with it. Therefore, independently of the complexity of the exosphere model used for calculations, the limitations are inherent to the thermosphere/ionospheric inputs employed. It is therefore highly desirable to employ a global kinetic model that includes a self-consistent description of both regions to provide a rigorous description of the exosphere, the hot corona, and the atmospheric loss.

I.2. Present study

In an effort to address this need, the initial studies couple self-consistently a 2D axisymmetric exosphere description with 3D thermosphere/ionosphere inputs by using a combination of the Direct Simulation Monte Carlo (DSMC) kinetic model and the Mars Thermosphere General Circulation Model (MTGCM) both for modern [*Valeille et al.* 2009a] and ancient [*Valeille et al.* 2009b] Mars conditions. Without any further approximations, the MTGCM provides all the parameters needed to evaluate the state of the background thermosphere and ionosphere and the production of hot oxygen atoms at any point around the planet. Exospheric results are presented as a function of SZA.

A full 3D DSMC, which includes the coronal particles and describes the heating of the thermosphere, was thought to be computationally too expensive in the past [*Leblanc and Johnson* 2001]. After design of a 3D unstructured mesh and improvement of our DSMC model, a complete 3D description of both the thermosphere/ionosphere and exosphere can be accomplished within a reasonable computational timeframe. The results are presented and discussed in this study.

In addition to allowing a better understanding of the Martian neutral hot corona, a 3D study of the exosphere provides more insightful inputs for ionospheric studies, such as the local exobase and ion peak height determination, local ion production, atom-to-molecule ratio variations at the exobase, and information on the nightside where few measurements exist. All these exosphere parameters are critical for current 3D plasma models, as mentioned in various studies [*Brecht 1997a, 1997b*; *Acuña et al.* 1998; *Leblanc and Johnson* 2001, 2002; *Ma et al.* 2002, 2004; *Modolo et al.* 2005; *Fang et al.* 2008] that would in turn give more detailed results on ion loss, atmospheric sputtering, and interaction with the solar wind in general. Also certain features, such as magnetic crustal fields, which influence ion loss [*e.g. Fang et al.* 2009], are localized and therefore can only be modeled in 3D.

The study of *Valeille et al.* [2009a] couples for the first time 3D thermospheric/ionospheric inputs [*e.g. Bougher et al.* 2006, 2008, 2009a] with a 2D exospheric description. It suggests, in particular, that varying Equatorial longitude and polar latitude cuts, *i.e.* calculations from 0° to 180° SZA along the Equator or through the Poles, present the greatest contrasts of thermospheric/ionospheric features and are

essentially the two extreme spatial dimensions of the Martian upper atmosphere environment (*i.e.* thermosphere/ionosphere and exosphere).

The same study quantifies not only the influence of the solar cycle, but also of seasons on the thermosphere/ionosphere and exosphere by characterizing the two extreme cases of net solar forcing for modern conditions, *i.e.* at the orbital position of Aphelion for solar Low (or sometimes called minimum) activity (AL) and at the orbital position of Perihelion for solar High (or sometimes called maximum) activity (PH). Conclusions show that seasonal variations are comparable with the influence of solar activity, and that they both need to be addressed for a better understanding of the Martian upper atmosphere and its interactions with its surrounding environment.

The same approach is used to study the evolution of the thermosphere/ionosphere and exosphere over Martian history in the study of *Valeille et al.* [2009b]. The inclusion of dynamics shows that it plays a very important role in the heating/cooling mechanisms of the ancient thermosphere and that past 1D models, which inherently neglect dynamics [*Zhang et al.* 1993b; *Lammer et al.* 2003], may have overestimated the exospheric temperatures and therefore the structure of the upper atmosphere in general. The study of *Valeille et al.* [2009b] further concludes that variations due to ancient solar conditions and modern solar activity are comparable and therefore that studies of the ancient atmosphere should take into account solar low and high conditions to bracket the limiting cases (or consider a solar cycle average in the past), as suggested in the recent study of *Chassefière et al.* [2007].

The work of *Valeille et al.* [2009c] couples a 3D thermosphere/ionosphere model with a 3D exosphere code and studies spatial variations with altitude and with angular position on the planet (diurnal and local features) in the upper atmosphere. The simulation is run at fixed orbital position of equinox for solar low conditions (EL case), to allow comparison with the only *in situ* measurements available today from the Viking 1 and 2 mission descents [*e.g. Hanson et al.*, 1977; *Nier and Mc Elroy* 1977]. It concludes that the thermospheric/ionospheric parameters exhibit local asymmetries that affect the entire structure of the upper atmosphere.

A complete description by a steady-state simulation requires two types of parameters to be investigated: spatial and temporal. So, while the study of *Valeille et al.* [2009c]

describes the spatial distribution of the upper atmosphere in the fixed EL case, the study of *Valeille et al.* [2009d] focuses on the variation of the thermosphere/ionosphere and exosphere parameters over all the principal timescales. Temporal perturbations can be distinguished by their characteristic time: short-scale (~1 hr), long-scale (~1-10 yr) and evolutionary-scale (~1 Gyr). A recent paper [*Kaneda et al.* 2007, 2009] indicates a possible mechanism that can cause a short-term (about 2000-seconds period) enhancement of the hot oxygen escape rate in response to a sudden increase in the solar wind dynamic pressure.

I.3. Thesis outline

In this thesis, I am presenting the work on the Martian thermosphere/ionosphere and exosphere regions conducted during the last three years at the Atmospheric, Oceanic and Space Science department of the University of Michigan.

The purpose of this first introductory chapter is to present the current status of the scientific research on the subject and its motivations.

General analytical solutions of the description of an exosphere are first given by assuming a collisionless exosphere and particle motion in a gravitational field (Chapter II). Different velocity distributions (including thermal and suprathermal, isotropic and Maxwellian distributions) are considered at a critical level where the particles are injected. This constitutes a general mathematical approach and can be applied to any planet. These theoretical problems are also simulated in the code and provide an excellent benchmark for validation of our code. They also provide a firm physical context for understanding some of the detailed features in the realistic but necessarily complicated model results.

Both thermospheric/ionospheric and exospheric models constituting our global approach, as well as how they are coupled, are then presented along with the main assumptions in the chemical and physical processes of the Martian upper atmosphere [*Valeille et al.* 2009a, 2009b, 2009c, 2009d] (Chapter III). Our global approach will then

be explained, and preliminary results on the hot oxygen production in the upper thermosphere will be discussed.

Calculations for fixed orbital position of equinox and for solar low conditions (EL case) are presented and discussed (Chapter IV). These specific conditions (corresponding to Viking measurements) have been systematically used in the past by modelers and serve as an example to illustrate the general structure and attributes of a 3D exosphere produced by a self-consistent 3D thermosphere/ionosphere model [*Valeille et al.* 2009a, 2009c]. Comparisons with other relevant studies of the last ten years are also presented.

Modern long-term periodic variations (timescales of about 1-10 yr) are first investigated (Chapter V). Along with the expected variability of the hot oxygen corona with solar cycle, this study is the first to show that differences in the results in general, and in the escape fluxes specifically, are important between the different orbital positions considered: equinox, perihelion and aphelion. These season driven variations are of the same order as solar cycle driven variations [*Valeille et al.* 2009a, 2009d].

The loss of water from Mars can be evaluated by studying the evolution of the escape rate of atomic oxygen over time (Chapter VI). Throughout Martian history, the evolution of solar radiation has led to significant variations in the macroscopic parameters of the thermosphere/ionosphere, which in turn governs the hot species population of the exosphere and especially the atmospheric loss rates [*Valeille et al.* 2009b, 2009d].

Secondary processes of creation of hot atomic oxygen (O), as well as the population and escape of other neutral exospheric hot species, such as hydrogen (H) and carbon (C), are investigated in a preliminary way. Future work is also discussed (Chapter VII).

Finally, the main results of the study are summarized in the conclusions (Chapter VIII) and their implication for other fields.

Chapter II

Ballistic motion of a particle in a gravitational field in spherical coordinates

In this chapter, a general analytical solution of the description of an exosphere is given by considering the motion of a single particle in the gravitational field of a spherical body in a collisionless domain. This mathematical approach can be applied for any body and for any particle independently of its energy (thermal or non-thermal).

The case of Mars will be used for numerical applications and illustration purpose in the remainder of this chapter. These assumptions are reasonable in the particular example of Mars as long as the domain of study is situated within a lower boundary, above which the particles flow can be characterized as collisionless, and an upper boundary, above which the gravitational field of other celestial bodies has to be taken into account and where the two-body approximation is no longer valid.

This theoretical exercise provides a solid benchmark for the most important processes of the exospheric code, which will be presented in detail in the next chapter and used all along this study in order to obtain a better understanding of the Martian upper atmosphere.

II.1. Equation of motion

In spherical coordinates (C, $\mathbf{e_r}$, $\mathbf{e_\Theta}$, $\mathbf{e_\Phi}$), with the center C of the planet taken as origin, the position, **r**, of a particle is written,

$$\vec{r} = r\vec{e}_r \tag{2.1}$$

Its velocity, **v**, is then, by differentiation,

$$\vec{v} = \frac{d\vec{r}}{dt} = \dot{r}\vec{e}_r + r\dot{\Theta}\vec{e}_\Theta + r\sin\Theta\,\dot{\Phi}\vec{e}_\Phi \tag{2.2}$$

Its acceleration, **a**, is therefore,

$$\vec{a} = \frac{d^2\vec{r}}{dt^2} = \begin{cases} \left(\ddot{r} - r\dot{\Theta}^2 - r\sin^2\Theta\,\dot{\Phi}^2\right)\vec{e}_r \\ \left(2\dot{r}\dot{\Theta} + r\ddot{\Theta} + r\sin\Theta\cos\Theta\,\dot{\Phi}^2\right)\vec{e}_\Theta \\ \left(2\,\dot{r}\sin\Theta\dot{\Phi} + 2r\cos\Theta\,\dot{\Theta}\dot{\Phi} + r\sin\Theta\ddot{\Phi}\right)\vec{e}_\Phi \end{cases} \tag{2.3}$$

Furthermore, the derivative of the angular momentum, **L**, is,

$$\frac{d\vec{L}}{dt} = \frac{d\vec{r}}{dt} \times m\vec{v} + \vec{r} \times m\frac{d\vec{v}}{dt} = \vec{0} + \vec{r} \times m\vec{a} \tag{2.4}$$

where m is the mass of the particle.

The gravity **g** of the planet, which is assumed to be the only force that acts on the particle, is radial. Newton's law then gives,

$$m\vec{a} = m\vec{g}(\vec{r}) = -m\frac{\mu}{r^2}\vec{e}_r \tag{2.5}$$

where $\mu = GM$, is the standard gravitational parameter, with G, gravitational constant (~ 6.67×10^{-11} $m^3\,kg^{-1}\,s^{-2}$) and M, mass of the planet (for Mars, it would be M ~ 6.42×10^{23} kg and then $\mu \sim 4.28 \times 10^{13}$ $m^3\,s^{-2}$).

It follows that the angular momentum **L** is conserved,

$$\frac{d\vec{L}}{dt} = -m\frac{\mu}{r}(\vec{e}_r \wedge \vec{e}_r) = \vec{0} \tag{2.6}$$

leading to,

$$\vec{L}(\vec{r}) = \vec{r} \times m\vec{v} = \begin{cases} 0 \\ -mrv_\Phi(\vec{r}) = \vec{L}(\vec{r}_0) = \vec{r}_0 \times m\vec{v}_0 = \begin{cases} 0 \\ -mr_0 v_{\Phi_0}(\vec{r}_0) \\ mr_0 v_{\Theta_0}(\vec{r}_0) \end{cases} \\ mrv_\Theta(\vec{r}) \end{cases} \tag{2.7}$$

where **v** and $\mathbf{v_0}$ are the particle velocity at the current and initial position **r** and $\mathbf{r_0}$, respectively. The position $\mathbf{r_0}$, where the particle is initially injected with the velocity $\mathbf{v_0}$, is situated at a critical level r_0, above which it is assumed that there are no collisions, no source and no sink of particles.

With these relations of conservation, and defining the perpendicular speed as,

$$v_\perp^2 = \sqrt{v_\Theta^2 + v_\Phi^2} \tag{2.8}$$

Equation (2.3) can be rewritten with expressions (2.7) and (2.8),

$$m\vec{a} = m\left(\ddot{r} - \frac{r_0^2 v_{\perp 0}^2}{r^3}\right)\vec{e}_r \tag{2.9}$$

And Newton's law (2.5) becomes,

$$\ddot{r} = \frac{r_0^2 v_{\perp 0}^2}{r^3} - \frac{\mu}{r^2} \tag{2.10}$$

II.2. Escaping and non-escaping particles

The particles can be divided in two exclusive groups: the escaping and non-escaping particles. The escaping particles are the ones with sufficient initial speed v_0 to "break free" from the gravitational field without any additional impulse (*i.e.* so that gravity will never manage to pull it back). This definition results in a condition on v_0 expressed via the equation of conservation of energy E(r), obtained by integrating Newton's law (2.5) over the infinitesimal element dr from r_0 to ∞,

$$E(r_0) = \frac{1}{2} m v_0^2 - m\frac{\mu}{r_0^2} = E(\infty) = \frac{1}{2} m v_\infty^2 \geq 0 \tag{2.11}$$

The minimum initial speed v_0 that satisfies this inequality is obtained for $v_\infty = 0$ and is equal to and defines the escape speed v_{esc},

$$v_{esc}(r) = \sqrt{2\mu/r} \tag{2.12}$$

the speed where the kinetic energy of an object is equal to the magnitude of its gravitational potential energy. Escape speed is independent of the mass of the particle. It depends only on the mass M of the planet and the distance where it is calculated. For illustration purpose, escape speeds for each planet of the solar system are presented in Table 2.1. Calculations are made either at the surface of the planet (for terrestrial inner planets) or at the altitude corresponding to a local pressure of 1 atm (for gas giant outer planets).

Table 2.1. Escape speeds at the planets of the solar system

	Terrestrial inner planets				Gas giant outer planets			
	Mercury	Venus	Earth	Mars	Jupiter	Saturn	Uranus	Neptune
R (x Earths)	0.38	0.95	1.00	0.53	11.21	9.45	4.01	3.88
M (x Earths)	0.06	0.82	1.00	0.11	317.18	95.15	14.54	17.15
Vesc (km s^{-1})	4.24	10.36	11.18	5.01	59.49	35.49	21.30	23.50

It is important to note that the general frame (C, $\mathbf{e_x}$, $\mathbf{e_y}$, $\mathbf{e_z}$) of this study is fixed by pointing towards arbitrary fixed stars and that steady-state is assumed. Therefore, initial conditions can be different for a particle defined in the frame associated with the planet. In this particular case, planetary rotation has to be taken into account, and the escape speed relative to the surface of a rotating body depends on direction, in which the escaping body travels. The surface speed decreases with the cosine of the geographic latitude, and this is the reason why space launch facilities are often located as close to the Equator as feasible (*e.g.* the American Cape Canaveral in Florida and the European Guiana Space Centre, only 5° from the Equator in French Guiana).

For simplicity sake, the frame of study adopted in this chapter is the general frame as defined above. Most of past works on Mars exosphere are either one- or two-dimensional and therefore can inherently account for neither planetary rotation nor winds. These parameters play however an important role on determining the initial speed v_0 of a particle and therefore affect its entire motion. Their effects will be treated in the following chapters.

II.3. Maximum altitude reached by non-escaping particles

While escaping particles have sufficient initial speed to escape the gravitational field of the planet, other particles (with $v_0 < v_{esc}$) are trapped in the gravitational field and will come back eventually to their initial altitude r_0.

Conservation of energy (2.11) can also be obtained after multiplying both sides of Equation (2.10) by $\dot{r}$ and integrating between time t, where the particle is at r and t_0 where it was at r_0,

$$\frac{\dot{r}^2}{2} - \frac{\dot{r}_0^2}{2} = -\frac{r_0^2 v_{1_0}^2}{2}\left(\frac{1}{r^2} - \frac{1}{r_0^2}\right) + \mu\left(\frac{1}{r} - \frac{1}{r_0}\right) \tag{2.13}$$

Using the expression of v_{esc} from Equation (2.11), and defining the angle θ_0 on $[0, \pi/2]$ of the vector $\mathbf{v_0}$ with respect to the local vertical (*i.e.* radial direction) $\mathbf{e_r}$,

$$\dot{r}^2 = v_0^2 \cos^2\theta_0 - v_0^2 \sin^2\theta_0 \left(\frac{r_0^2}{r^2} - 1\right) + v_{esc}^2(r_0)\left(\frac{r_0}{r} - 1\right) \tag{2.14}$$

The domain of definition $\mathfrak{D}$ of this equation is $\mathfrak{D} = [r_0, \infty[$ for escaping particles, but is $\mathfrak{D} = [r_0, r_{max}]$ and finite for non-escaping particles.

r_{max} is the maximum distance from the center of the planet they reach before they fall back down ballistically towards the critical level r_0. It corresponds to $\dot{r} = 0$ in Equation (2.13), and by writing $a = r_0/r$ on]0, 1], is the solution of the quadratic equation,

$$\sin^2 \theta_0 \, a^2 - X_0 a + (X_0 - 1) = 0 \tag{2.15}$$

where $X_0 = (v_{esc}(r_0)/ v_0)^2$ is the escape parameter, square of the ratio of the escape speed over the particle speed at the critical level r_0. It is strictly positive (X_0]0, ∞[) and allows to make the distinction between non-escaping particles ($X_0 > 1$), and escaping particles ($X_0 \leq 1$). It equals 1 at the local escape speed (*i.e.* $v_0 = v_{esc}(r_0)$) and commonly used with the most probable speed (*i.e.* $v_0 = v_{th}(r_0)$) to quantify, for instance, Jeans escape. The trivial case ($v_0 = 0$) will be put aside in the remaining of this chapter (for the sake of X_0 definition).

For $\theta_0 \neq 0$ and $v_0 \neq 0$, the roots a_- and a_+ of Equation (2.15) are,

$$a_\pm = \frac{X_0 \pm \sqrt{X_0^2 - 4 \sin^2 \theta_0 (X_0 - 1)}}{2 \sin^2 \theta_0} \tag{2.16}$$

For non-escaping particles, only one root is acceptable within the domain of definition of a. By multiplying numerator and denominator by denominator conjugate expression, r_{max} can be written,

$$r_{max}(r_0, \vec{v}_0) = \frac{X_0 + \sqrt{X_0^2 - 4 \sin^2 \theta_0 (X_0 - 1)}}{2(X_0 - 1)} r_0 \tag{2.17}$$

This function is plotted in Figure 2.1. For a given initial speed, particles with lower pitch angle reach higher altitudes. In all cases, $v_0 = v_{esc}(r_0)$ is the asymptotic value where r_{max} is infinity. The particles can be classified in two groups. The ballistic component consists of particles ejected from r_0, while the orbiting component consists of particles circling the planet in elliptic orbits not intersecting the base of the domain. Two extreme cases can be distinguished. Radial particles ($\theta_0 = 0$, in dark blue in Figure 2.1) attain the highest altitudes, whereas perpendicular particles ($\theta_0 = \pi/2$, in light blue in Figure 2.1) need a initial speed superior to $v_{esc}(r_0)/\sqrt{2}$ (*i.e.* ~3.5 km s^{-1} at the Martian surface) in order to take off. In a computational simulation, the size of the domain of study is limited. In Figure 2.1, the distances from the center of the planet of three and ten Martian radii are

represented corresponding to the respective 3D and 2D simulation domains presented in the next chapter.

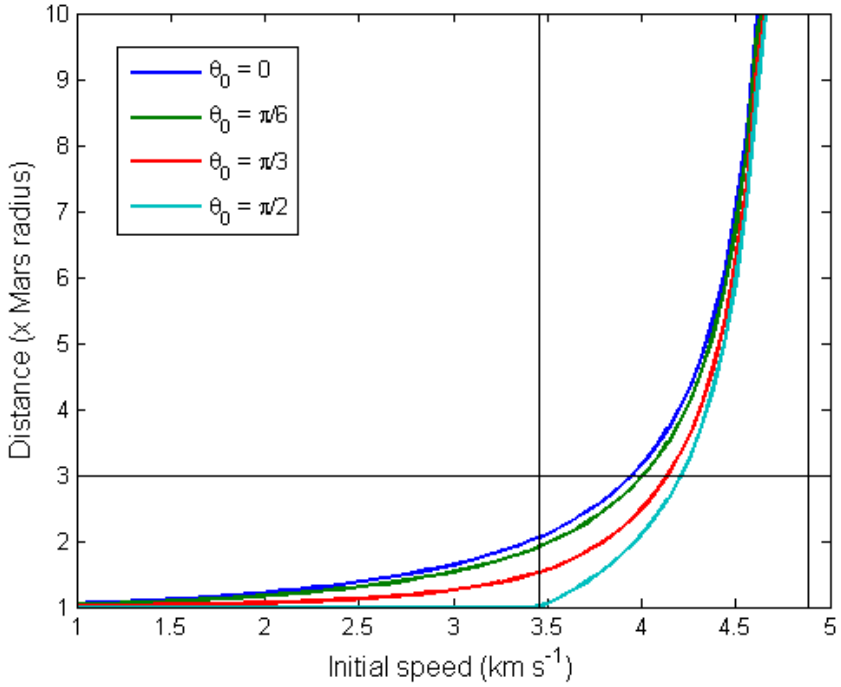

Figure 2.1. Maximum altitude reached by non-escaping particles. The two black vertical lines correspond to $v_{esc}(r_0)$ and $v_{esc}(r_0)/\sqrt{2}$.

For an initially purely perpendicular particle, two cases must be considered,

If $0 \leq v_0 \leq v_{esc}(r_0)/\sqrt{2}$,

$$r_{max}(r_0, \vec{v}_0) = r_0 \tag{2.19}$$

If $v_{esc}(r_0)/\sqrt{2} \leq v_0 < v_{esc}(r_0)$,

$$r_{max}(r_0, \vec{v}_0) = \frac{1}{X_0 - 1} r_0 \tag{2.20}$$

Both solutions (2.19) and (2.20) correspond to elliptical orbits, but only (2.20) belongs to the family of ellipses that have a semi-major axis bigger than the radius of the planet (see Figure 2.2).

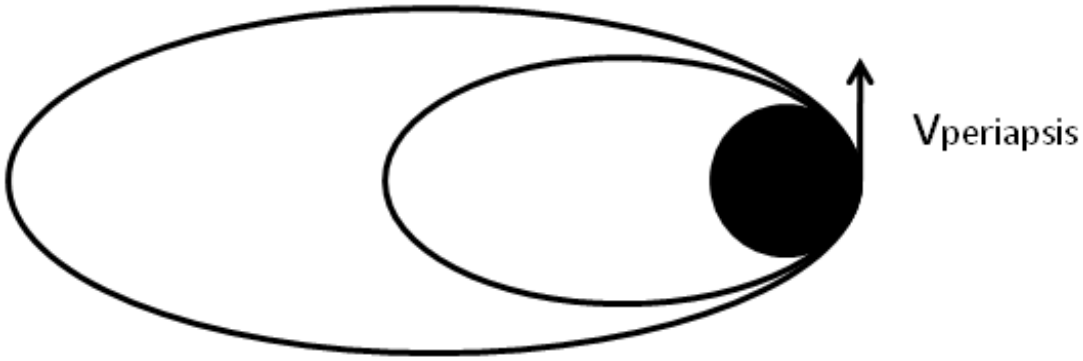

Figure 2.2. Family of elliptical satellite orbits.

II.4. Velocity profile

From Equations (2.7) and (2.14), the velocity can be written, on the same respective domain of definition $\mathfrak{D}$,

$$\vec{v}(\vec{r}) = \begin{cases} v_0\sqrt{1-\left(\frac{r_0}{r}\sin\theta_0\right)^2 - X_0\left(1-\frac{r_0}{r}\right)}\,\vec{e}_r \\ \frac{r_0}{r}\,v_{\theta_0}(\vec{r}_0)\vec{e}_\theta \\ \frac{r_0}{r}\,v_{\varphi_0}(\vec{r}_0)\vec{e}_\varphi \end{cases} \tag{2.21}$$

The speed v can then be written,

$$v(r) = \sqrt{v_0^2 - \left(v_{esc}^2(r_0) - v_{esc}^2(r)\right)} \tag{2.22}$$

For escaping particle, the velocity becomes radial and reaches saturation,

$$\lim_{r\to\infty}\vec{v}(r) = v_\infty\vec{e}_r = \sqrt{v_0^2 - v_{esc}^2(r_0)}\,\vec{e}_r \tag{2.23}$$

corresponding to the asymptote on Figure 2.3 (black line).

More precisely, with a Taylor expansion of first order on r_0/r,

$$\vec{v}(r) \sim_{r\to\infty} v_\infty\vec{e}_r + \frac{r_0}{r}\vec{v}_{cor} + O\left(\left(\frac{r_0}{r}\right)^2\right) \tag{2.24}$$

with,

$$\vec{v}_{cor} = \frac{1}{2}\frac{v_{esc}^2(r_0)}{v_\infty}\vec{e}_r + v_{\perp_0}(r_0)\vec{e}_\perp \tag{2.25}$$

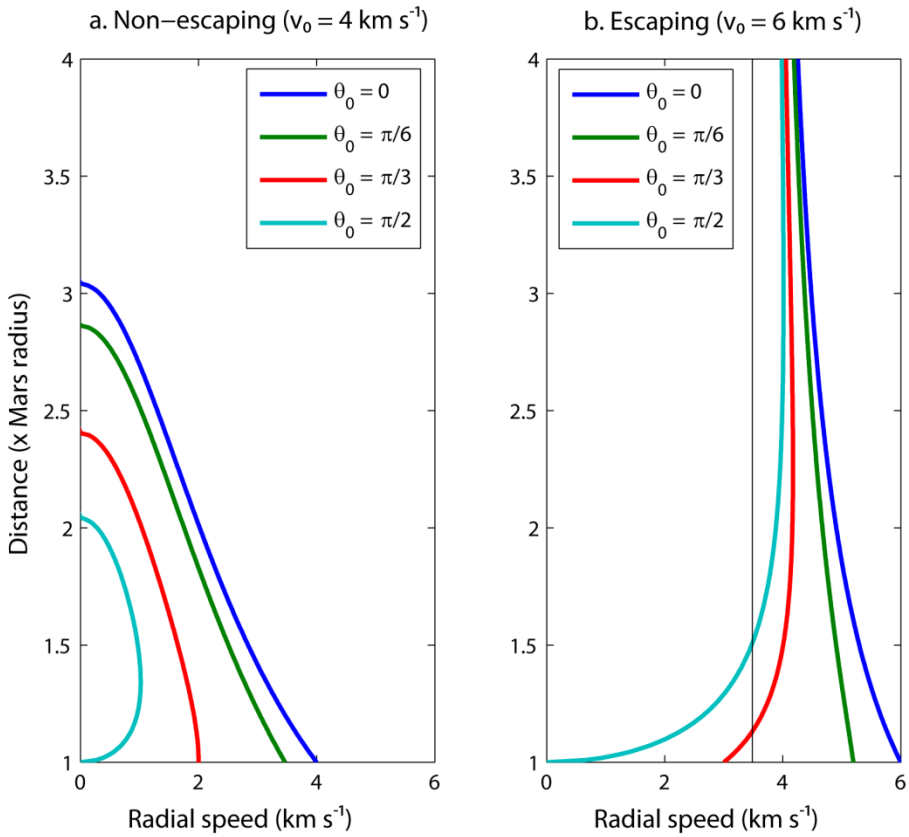

Figure 2.3. Radial component of the velocity for non-escaping (a) and escaping (b) particles for various initial pitch angle θ_0. The black vertical line in (b) corresponds to v_∞.

Figure 2.3 shows the radial component of the velocity for both non-escaping (v_0 = 4 km s^{-1}, Figure 2.3a) and escaping (v_0 = 6 km s^{-1}, Figure 2.3b) particles for various initial pitch angles. Non-escaping ballistic particles decelerate until their radial speed becomes null at r_{max} and then fall back down. Initially perpendicular particles on elliptical orbits see their radial speed first increases, then decreases, until they reach r_{max}, where it turns negative. Radial speeds of all escaping particles either increase or decrease and ultimately tend to the asymptotic value of v_∞.

II.5. Time of flight and angular displacement

II.5.1. Time of flight

With different initial speeds v_0 and directions θ_0, particles will spend a different time t_0 (from a very wide range) in the domain of study. A particle exits the domain of study when it crosses the upper boundary, r_{ext}, or the lower boundary, r_0. It is important to note that because the domain of study is finite, particles that exit the domain at the upper boundary are escaping particles and nearly-escaping particles, *i.e.* non-escaping particles that have a maximum altitude above the upper limit ($r_{max} > r_{ext}$). The study of the time of flight t_0 allows a better understanding of the ionization and collision processes in the exosphere/upper-ionosphere. Indeed, for instance, the probability of photoionization of a particle, p_{PI}, is proportional to the time t_0 spent by the particle in the system,

$$p_{PI} = 1 - e^{-\frac{t_0}{t_{PI}}} \sim \frac{t_0}{t_{PI}} \tag{2.26}$$

where t_{PI} is the local photoionization time (increasing with increasing heliocentric distance), and $t_{PI} >> t_0$. In the same way, a probability of collision could be estimated.

For escaping and nearly-escaping particles, the time of flight in the system is given by,

$$t_0 = t(r_0, \vec{v}_0) = \int_{r_0}^{r_{ext}} \frac{dr}{v_{\parallel}(r)} \tag{2.27}$$

For non-escaping particles, the time of flight in the system is given by,

$$t_0 = t(r_0, \vec{v}_0) = 2\int_{r_0}^{r_{max}} \frac{dr}{v_{\parallel}(r)} \tag{2.28}$$

With the expression of the radial velocity (2.21), the identities (2.27) and (2.28) can be rewritten, respectively,

$$t_0 = \frac{1}{v_0}\int_{r_0}^{r_{ext}} \frac{rdr}{\sqrt{-(r_0 \sin\theta_0)^2 + (X_0 r_0)r + (1-X_0)r^2}} \tag{2.29}$$

$$t_0 = \frac{2}{v_0}\int_{r_0}^{r_{max}} \frac{rdr}{\sqrt{-(r_0 \sin\theta_0)^2 + (X_0 r_0)r + (1-X_0)r^2}} \tag{2.30}$$

Figures 2.4a and 2.4b show that particles that spend the most time in the system have non-escaping high velocities (v_0 between 3.5 and 5.0 km s^{-1}).

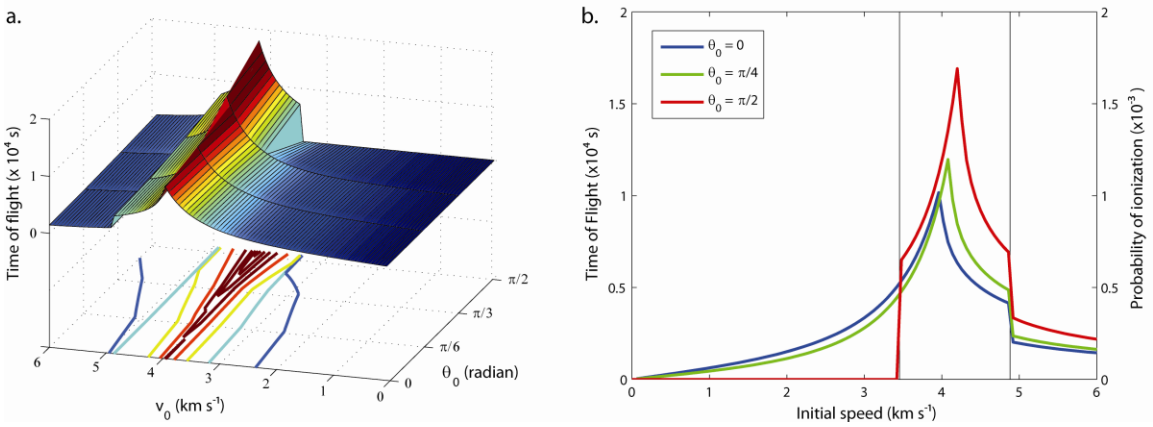

Figure 2.4. Time of flight in a 3-Martian-radius domain of study for particles with initial speed v_0 up to 6.0 km s^{-1}.

II.5.2. Angular displacement and deviation

II.5.2.1. Angular displacement

Similarly, with different initial speeds v_0 and directions θ_0, particles undergo different angular displacements β_0 in their motion in the domain of study. β_0 is the angle between the position where the particle is injected initially and the final position where the particle exits the system. This is particularly important to understand (in a 2D axisymmetric simulation for instance) the apparent paradox of a nightside population in a problem where particles are created on the dayside of the planet only.

For escaping and nearly-escaping particles, the angular displacement in the system is given by,

$$\beta_0 = \beta(r_0, \vec{v}_0) = \int_{r_0}^{r_{ext}} \frac{v_{\perp 0}(r_0) r_0 dt}{r^2} \tag{2.31}$$

For non-escaping particles, the angular displacement in the system is given by,

$$\beta_0 = \beta(r_0, \vec{v}_0) = 2\int_{r_0}^{r_{max}} \frac{v_{\perp 0}(r_0) r_0 dt}{r^2} \tag{2.32}$$

With the expression of the radial velocity (2.21), the identities (2.27) and (2.28) can be rewritten, respectively,

$$\beta_0 = r_0 \sin\theta_0 \int_{r_0}^{r_{ext}} \frac{dr}{r\sqrt{-(r_0 \sin\theta_0)^2 + (X_0 r_0) r + (1 - X_0) r^2}} \tag{2.33}$$

$$\beta_0 = 2\, r_0 \sin\theta_0 \int_{r_0}^{r_{max}} \frac{dr}{r\sqrt{-(r_0 \sin\theta_0)^2 + (X_0 r_0) r + (1 - X_0) r^2}} \tag{2.34}$$

Figure 2.5a shows the angular displacement β_0 for particles with different initial speeds v_0 and directions θ_0 (in solid lines) for a 3-Martian-radius domain.

II.5.2.2. Angular deviation

The angle of deviation $\Delta\beta$ is defined in this study as the differential effect of an additional perpendicular push, $\mathbf{v}_{add}$, added to the initial velocity, $\mathbf{v}_0$, of a particle, *i.e.*,

$$\Delta\beta = \beta_1 - \beta_0 = \beta(r_0, \vec{v}_0 + \vec{v}_{add}) - \beta(r_0, \vec{v}_0) \quad (2.35)$$

This constitutes the theoretical explanation of the effect of thermospheric winds and/or planetary rotation on the exospheric distribution of a celestial body.

Figure 2.5a shows (in dashed lines) the angular displacement β_1 due to an additional perpendicular push of $v_{add} = v_{PR} = 240$ m s^{-1} added to the initial velocity, $\mathbf{v}_0$, of a particle in a 3-Martian-radius domain. This corresponds to the Equatorial rotation speed at the Martian surface. Horizontal thermospheric wind speeds would be about twice faster ($v_{add} = v_{TW} \sim 500$ m s^{-1}). Because the two effects are in opposite directions (on Mars, planetary rotation is directed towards east, whereas thermospheric winds are towards west), their cumulative effect is somewhat similar to the planetary rotation alone ($v_{add} = v_{TW} - v_{PR} \sim v_{PR}$). The angular deviation $\Delta\beta$ due to the planetary rotation is presented in Figure 2.5b.

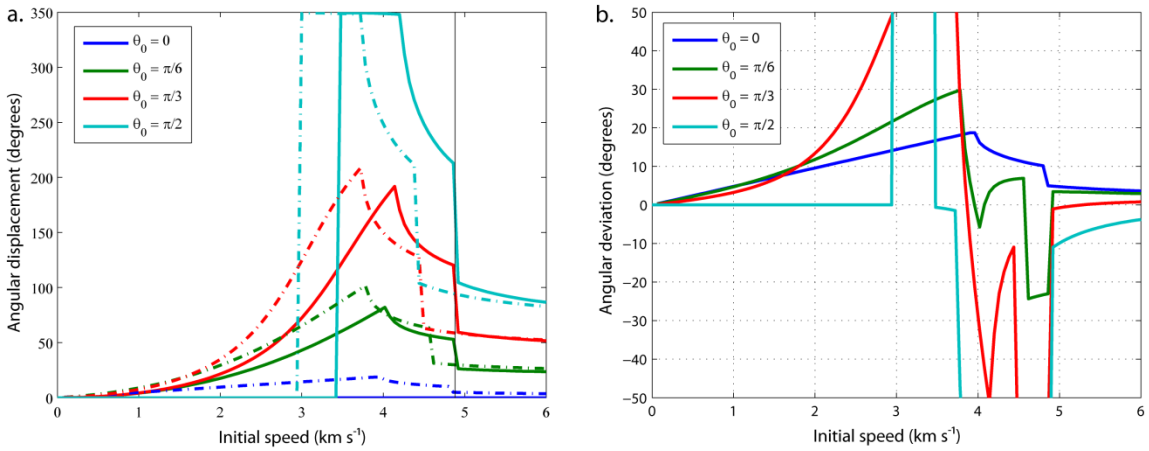

Figure 2.5. Angular displacement (a) and angular deviation (b) due to an additional perpendicular push added to the initial velocity of the particle.

II.6. Density profile

II.6.1. General case

According to Liouville's theorem, one can write,

$$f(\vec{r},\vec{v}) = f(\vec{r}_0,\vec{v}_0) \tag{2.36}$$

where f is the velocity distribution function in spherical coordinates. This asserts that the phase-space distribution function is constant along the trajectories of the system - that is that the density of system points in the vicinity of a given system point travelling through phase-space is constant with time.

For simplicity sake, a uniform distribution of injected particles all around the planet relative to the initial position $\mathbf{r_0}$ in the spatial frame (r, Θ, Φ) is used here. By symmetry of the problem, all expressions in the remainder of this chapter are then functions of the scalar distance, r, rather than the vector position, **r**.

The conservation of energy (2.13) and angular momentum (2.7) relations give the relationships between v, v_0, θ and θ_0,

$$\begin{bmatrix} v^2 - v_{esc}^2(r) = v_0^2 - v_{esc}^2(r_0) \\ rv\sin\theta = r_0 v_0 \sin\theta_0 \end{bmatrix} \tag{2.37}$$

Decoupling this $\{(v,\theta);(v_0,\theta_0)\}$ system leads to the following relations,

$$\begin{bmatrix} v(r) = \sqrt{v_0^2 - \left(v_{esc}^2(r_0) - v_{esc}^2(r)\right)} \\ \sin\theta = \frac{v_0}{\sqrt{v_0^2 - \left(v_{esc}^2(r_0) - v_{esc}^2(r)\right)}} \frac{r_0}{r} \sin\theta_0 \end{bmatrix} \tag{2.38}$$

The density n(r) at the position, r, can then be written,

$$\begin{aligned} n(r) &= \varepsilon \int_0^\infty \int_0^{2\pi} \int_0^{\pi/2} f(r,\vec{v})\, \delta^3 v \\ &= \varepsilon \int_0^\infty \int_0^{2\pi} \int_0^{\pi/2} f(r,\vec{v})\, v^2 \sin\theta \, dv d\theta d\varphi \end{aligned} \tag{2.39}$$

The factor ε equals 1 when the density, n(r), refers to escaping particles, whereas it equals 2 for non-escaping particles. Indeed, escaping particles are only moving in the upward direction away from the planet ($\theta < \pi/2$), whereas (for an infinitesimal volume in the domain of definition) half of the non-escaping are moving away from the planet ($\theta < \pi/2$) and the other half towards the planet ($\theta > \pi/2$).

This results in a discontinuity in the densities of escaping particles in the vicinity of the critical level altitude, r_0. Indeed, below the level, the velocity distribution is assumed

isotropic (half the population moving upward, half the population moving downward), whereas above it, all the population is moving upward.

Rewriting relation (2.34) exclusively in term of the initial conditions leads to,

$$n(r) = \varepsilon \iiint_{\vec{v}_0 \epsilon Def_J} f(r_0, \vec{v}_0) |J_{\vec{v}(\vec{v}_0)}| \, v^2 \sin\theta \, dv_0 d\theta_0 d\varphi_0 \tag{2.40}$$

where $|J_{\vec{v}(\vec{v}_0)}|$ is the determinant of the Jacobian matrix from the current frame R to the initial frame R_0. Def_J is the domain of definition of $J_{\vec{v}(\vec{v}_0)}$. For a non-escaping particle, it includes the condition that at any altitude level, the particle must have an upward velocity of zero (corresponding to r_{max}) or greater (below r_{max}). It is also important to note that v does not depend on θ_0.

$$\left|J_{\vec{v}(\vec{v}_0)}\right| = \left|\frac{\partial v}{\partial v_0} \times \frac{\partial \theta}{\partial \theta_0}\right| = \left|\frac{r_0 v_0^2 \cos\theta_0}{r v^2 \cos\theta}\right| \tag{2.41}$$

With Equation (2.36), part of the expression in the integral in (2.35) can be developed to,

$$\begin{aligned} v^2 \sin\theta \left|J_{\vec{v}(\vec{v}_0)}\right| &= \frac{r_0 v_0^2 \cos\theta_0}{r} \tan\theta \\ &= \frac{r_0 v_0^2 \cos\theta_0}{r} \frac{r_0 v_0 \sin\theta_0}{\sqrt{r^2 v^2 - (r_0 v_0 \sin\theta_0)^2}} \\ &= \frac{r_0^2}{r^2} \frac{v_0^2 \cos\theta_0 \sin\theta_0}{\sqrt{1 - \left(\frac{r_0}{r}\sin\theta_0\right)^2 - \frac{v_{esc}^2(r_0)}{v_0^2}\left(1 - \frac{r_0}{r}\right)}} \end{aligned} \tag{2.42}$$

And, using the above definition of the escape parameter, X_0, the expression of the density (2.35) can be simplified to,

$$n(r) = \varepsilon \frac{r_0^2}{r^2} \iiint_{\vec{v}_0 \epsilon Def_J} \frac{f(r_0, \vec{v}_0) v_0^2 \cos\theta_0 \sin\theta_0}{\sqrt{1 - \left(\frac{r_0}{r}\sin\theta_0\right)^2 - X_0\left(1 - \frac{r_0}{r}\right)}} dv_0 d\theta_0 d\varphi_0 \tag{2.43}$$

Given Equation (2.38), the density, n(r), at a location, r, can be calculated if the velocity distribution function, $f(r_0, \mathbf{v_0})$, is known. Analytic expressions for n(r) are obtained assuming various distributions at the critical level r_0.

II.6.2. Constant initial velocity v_0

If all particles are injected with the same upward velocity $\mathbf{v_0} = \mathbf{v_0}'$ ($\theta < \pi/2$), the velocity distribution function is, at r_0,

$$f(r_0, \vec{v}_0) \, v_0^2 \sin\theta_0 = \frac{n(r_0)}{2} \delta(v_0 - v_0') \delta(\theta_0 - \theta_0') \delta(\varphi_0 - \varphi_0') \tag{2.44}$$

The factor ½ comes again from the above assumption that below the level r_0, half of the particles move upward (and then are actually injected in the domain of study) and half of them move downward. This assumption is made for the sake of the continuity in the densities of returning particles. δ is the Dirac delta function, defined as,

$$\delta(x) = \begin{cases} \infty \; for \; x = 0 \\ 0 \; for \; x \neq 0 \end{cases} \tag{2.45}$$

and which is also constrained to satisfy the identity,

$$\int_{-\infty}^{+\infty} \delta(x)dx = 1 \tag{2.46}$$

Expressions (2.35) and (2.36) lead then to,

$$n(r) = \varepsilon n(r_0)\frac{r_0^2}{r^2}\iiint_{\vec{v}_0 \epsilon Def_J} \frac{\cos\theta_0 \delta(v_0 - v_0')\delta(\theta_0 - \theta_0')\delta(\varphi_0 - \varphi_0')}{\sqrt{1-\left(\frac{r_0}{r}\sin\theta_0\right)^2 - X_0\left(1-\frac{r_0}{r}\right)}} dv_0 d\theta_0 d\varphi_0$$

$$= \frac{\varepsilon}{2} n(r_0)\frac{r_0^2}{r^2}\frac{\cos\theta_0}{\sqrt{1-\left(\frac{r_0}{r}\sin\theta_0\right)^2 - X_0\left(1-\frac{r_0}{r}\right)}} \tag{2.47}$$

This expression could also have been obtained by using the conservation of the upward flux between r_0 and r, in the limit of the domain of definition,

$$4\pi r^2 v_{\parallel}(r)n(r) = 2\varepsilon\pi r_0^2 v_{\parallel}(r_0)n(r_0) \tag{2.48}$$

For the particular case of radial injection (θ_0' = 0) of non-escaping particles (ε = 2), the expression (2.38) becomes,

$$n(r) = n(r_0)\frac{r_0^2}{r^2}\frac{1}{\sqrt{1-X_0\left(1-\frac{r_0}{r}\right)}} \tag{2.49}$$

This case presents the advantage to be an excellent benchmark for a simulation as it provides a validation of the resolution and precision of the computational results. Figures 2.6a and 2.6b compare theory and Monte Carlo computations for 1D and 2D simulations, respectively. The parameters r_0 and n_0 are arbitrary, whereas v_0 is chosen in order for the particles to reach a reasonable maximum altitude (r_1 on Figure 2.6) compared to the characteristic dimensions of the domain of study. Note that for very fast escaping particles, X_0 tends to 0 and the expression (2.49) becomes logically the r^2 decrease of the density n.

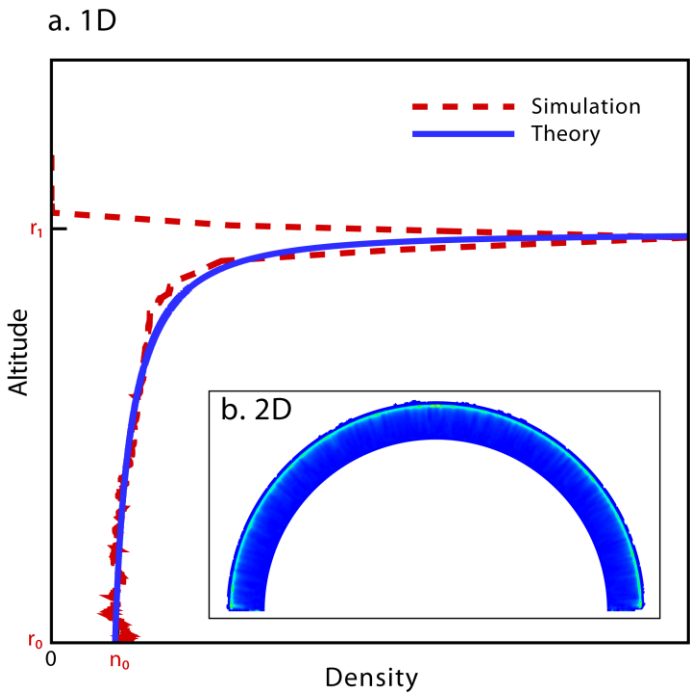

Figure 2.6. Density profile for radial non-escaping particles computed by 1D (a) and 2D (b) spherical simulations. Results from the simulation (a, red dashed line) can be compared with the theory (a, blue solid line).

II.6.3. Isotropic distribution (constant initial speed v_0)

If all particles are injected isotropically into the upward 2π steradian with the same upward speed $v_0 = v_0'$, the velocity distribution function is, at r_0,

$$f(r_0, \vec{v}_0) = \frac{\delta(v_0 - v_0')}{4\pi v_0^2} n(r_0) \tag{2.50}$$

Expressions (2.35) and (2.36) lead then to,

$$n(r) = \frac{\varepsilon n(r_0)}{4\pi} \frac{r_0^2}{r^2} \iiint_{\vec{v}_0 \epsilon Def_J} \frac{\delta(v_0 - v_0') \cos\theta_0 \sin\theta_0}{\sqrt{1 - \left(\frac{r_0}{r}\sin\theta_0\right)^2 - X_0\left(1 - \frac{r_0}{r}\right)}} dv_0 d\theta_0 d\varphi_0$$

$$= \frac{\varepsilon}{2} \frac{r_0^2}{r^2} n(r_0) \int_0^{\theta_{lim}(r)} \frac{\sin\theta_0 \cos\theta_0}{\sqrt{1 - \left(\frac{r_0}{r}\sin\theta_0\right)^2 - X_0\left(1 - \frac{r_0}{r}\right)}} d\theta_0 \tag{2.51}$$

where θ_{lim}, function of r and the initial state (r_0, $\mathbf{v_0}$), is the initial angle of a particle that reaches its maximum altitude at r (*i.e.* for which $r = r_{max}(r_0, \mathbf{v_0})$). It is defined, for non-escaping particles (finite r_{lim}) as,

$$\theta_{lim}(r) = \arcsin\left(\frac{r}{r_0}\sqrt{1 - X_0\left(1 - \frac{r_0}{r}\right)}\right)$$

$$= \arcsin\left(\sqrt{\frac{r}{r_0}\frac{r_{lim} - r}{r_{lim} - r_0}}\right) \quad (2.52)$$

For escaping particle, θ_{lim} is constant and equals $\pi/2$.

With the change of variable $s = \sin\theta_0$ monotonic from $[0, \theta_{lim}(r)]\mathbb{C}[0, \pi/2]$ to $[0, \sin\theta_{lim}(r)]\mathbb{C}[0,1]$, (2.28) becomes,

$$n(r) = \frac{\varepsilon}{2}\frac{r_0^2}{r^2} n(r_0) \int_0^{\sin\theta_{lim}(r)} \frac{s}{\sqrt{1 - \left(\frac{r_0}{r}s\right)^2 - X_0\left(1 - \frac{r_0}{r}\right)}}\, ds \quad (2.53)$$

II.6.3.1. For non-escaping particles

With $A_r^2 = 1 - X_0\left(1 - \frac{r_0}{r}\right) = \left(\frac{r_0}{r}\sin\theta_{lim}(r)\right)^2$ and the change of variable $y = \frac{r_0}{r}\frac{s}{A_r} = \frac{s}{\sin\theta_{lim}(r)}$ monotonic from $[0, \sin\theta_{lim}(r)]\mathbb{C}[0,1]$ to $[0,1]$,

$$n(r) = n(r_0) A_r \int_0^1 \frac{y}{\sqrt{1 - y^2}}\, dy \quad (2.54)$$

With the change of variable $z = \arcsin y$ monotonic from $[0,1]$ to $[0, \pi/2]$ when $\frac{r_0}{r} \leq A_r$, *i.e.* when $r \geq r_{lim} - r_0$,

$$n(r) = A_r n(r_0) \int_0^{\pi/2} \sin z\, dz = A_r n(r_0) \quad (2.55)$$

When $r = r_0$, $A_r = 1$, and $n(r) = n(r_0)$.

And, as $\lim_{r \to r_{lim}} A_r = 0$, we found $\lim_{r \to r_{lim}} n(r) = 0$,

$$n(r) = \sqrt{1 - X_0\left(1 - \frac{r_0}{r}\right)}\, n(r_0) \quad (2.56)$$

Figure 2.7 shows a hypothetical density profile of an isotropic injection ($n_0 = 10^5$ cm^{-3}) for r_0 corresponding to an altitude of 200 km for non-escaping particles ($v_0 = 4$ km s^{-1}) .

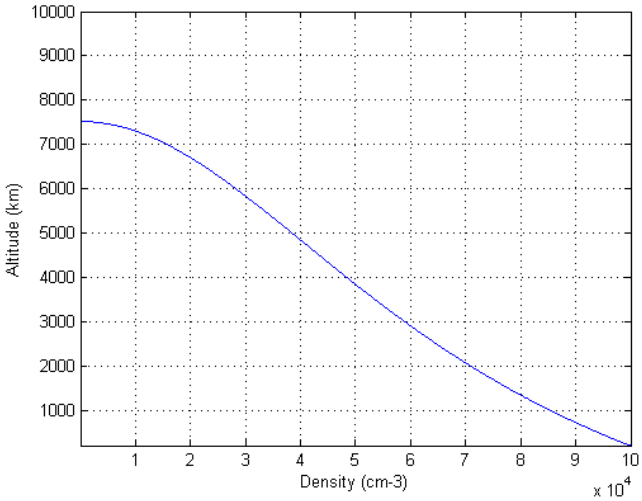

Figure 2.7. Density profile of an isotropic injection of non-escaping particles at the critical level r_0.

II.6.3.2. For escaping particles

With $A_r^2 = 1 - X_0\left(1 - \frac{r_0}{r}\right)$ and the change of variable $Y = \frac{r_0}{r}\frac{s}{A_r}$monotonic from [0,1] to $\left[0, \frac{r_0}{r}\frac{1}{A_r}\right] \mathrm{C} \left[0, \frac{1}{A_{r_0}}\right] = [0,1]$,

$$n(r) = \frac{1}{2} n(r_0) A_r \int_0^{\frac{r_0}{r}\frac{1}{A_r}} \frac{y}{\sqrt{1-y^2}}\, dy \tag{2.57}$$

With the change of variable $z = \arcsin \mathrm{y}$ monotonic from $\left[0, \frac{r_0}{r}\frac{1}{A_r}\right] \mathrm{C}[0,1]$ to $\left[0, \arcsin\left(\frac{r_0}{r}\frac{1}{A_r}\right)\right] \mathrm{C}[0, \pi/2]$,

$$n(r) = \frac{1}{2} n(r_0) A_r \int_0^{\arcsin\left(\frac{r_0}{r}\frac{1}{A_r}\right)} \sin z\, dz$$

$$n(r) = \frac{1}{2} A_r \left(1 - \sqrt{1 - \left(\frac{r_0}{r}\frac{1}{A_r}\right)^2}\right) n(r_0) \tag{2.58}$$

When $r = r_0$, $A_{r_0} = 1$, and $n(r) = \frac{1}{2} n(r_0)$.

With $A_\infty = \lim_{r\to\infty} A_r = \sqrt{1 - X_0}$, the expression of the density n(r) can be found,

$$\lim_{r\to\infty} n(r) \sim \frac{n(r_0)}{2A_\infty}\left(\frac{r_0}{r}\right)^2 \tag{2.59}$$

This result can be also found by conservation of the normal flux and the asymptotic expression of the velocity (2.23).

Figure 2.8 shows a hypothetical density profile of an isotropic injection ($n_0 = 10^5$ cm^{-3}) for r_0 corresponding to an altitude of 200 km for non-escaping particles (v_0 = 6 km s^{-1}) at Mars. It can be compared with Figure 2.7.

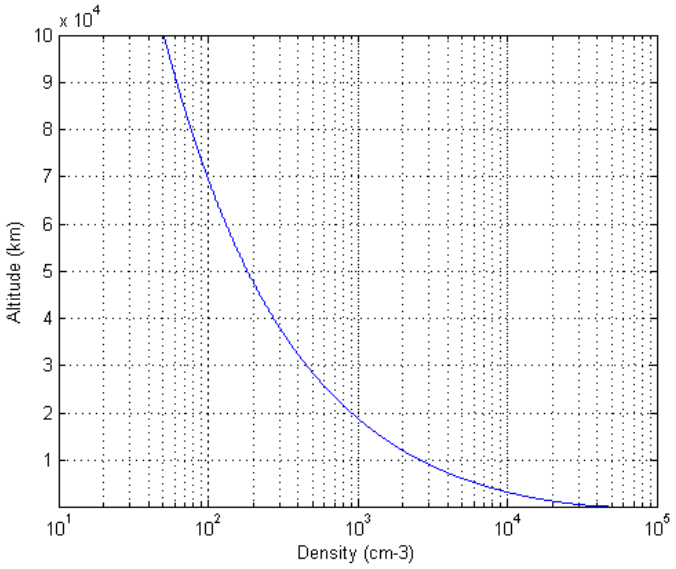

Figure 2.8. Density profile of an isotropic injection of escaping particles at the critical level r_0.

II.6.4. Thermal (Maxwellian) distribution

Finally, a Maxwellian velocity distribution is assumed for the base of the domain of study, which ejects particles in it. The density distribution is then calculated numerically.

$$f(\vec{r}_0, \vec{v}_0) = 8\pi^2 r_0^2 \left(\frac{m}{2\pi kT}\right)^{\frac{3}{2}} n(r_0) e^{-m/2kT\, v_0^2}\, v^2 \sin\theta\, dv_0 d\theta_0 d\varphi_0 \tag{2.60}$$

The green line represented in Figure 2.9 would be the density profile for a Maxwellian distribution in a thick isothermal atmosphere. Its expression is given by the barometric formula,

$$n_h(r) = n_0 e^{-\left(1-\frac{r_0}{r}\right)E} \tag{2.61}$$

with,

$$E = \frac{r_0}{H_0} \tag{2.62}$$

where H_0 is the scale height at r_0,

$$H_0 = H(r_0) = \frac{kT_0}{mg_0} \tag{2.63}$$

If it is assumed that there is no collision above the critical level r_0, the density profile would be [see *Opik and Singer* 1959, 1961; *Shen* 1963],

$$n_T(r) = n_h(r) - n_c(r) \tag{2.64}$$

with,

$$n_c(r) = n_0\sqrt{\left(1 - \left(\frac{r_0}{r}\right)^2\right)}\, e^{-\frac{E}{\left(1+\frac{r_0}{r}\right)}} \tag{2.65}$$

n_T differs from the barometric formula (2.61) by a term $n_c(r)$. This term n_C is zero when $r = r_0$, it increases with r, and its asymptotic value is n_0e^{-E}. Note that n_T gives zero density at infinity, which is different from that obtained assuming hydrostatic approximation.

Finally, if it is taken into account that the escaping particles were counted twice, the density profile is written,

$$n_a(r) = n_T(r) - n_s(r) \tag{2.66}$$

with,

$$n_s(r) = n_0 \frac{\left(\frac{r_0}{r}\right)^2}{2\sqrt{\pi E}} \frac{(1+E)e^{-E}}{H(E)-1+\sqrt{1-\frac{2}{3}H(E)\frac{r_0}{r}}} \tag{2.67}$$

where,

$$H(E) \underset{E\to\infty}{\sim} 1 + \frac{2}{E} \tag{2.68}$$

Here $n_a(r)$ is the actual density distribution of a collisionless exosphere. It is plotted in blue in Figure 2.9 along with the barometric formula (green dashed-dotted line). The density distribution of a real exosphere should lie between the two curves, depending on the efficiency of the collision process in the exosphere.

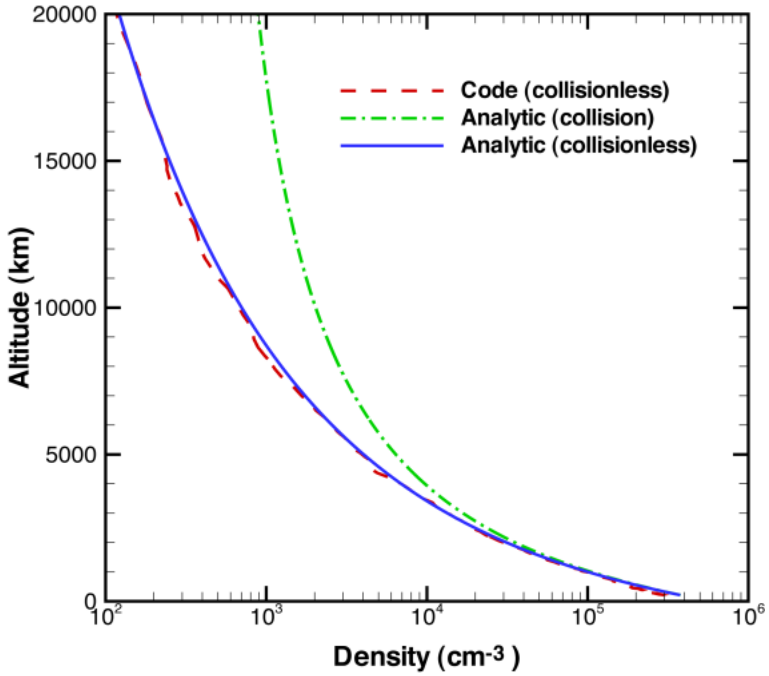

Figure 2.9. Density profiles of a thermal injection of particles at a critical level r_0. The numerical results (red dashed line) are compared to the theory for collision and collisionless domains (blue solid line and green dashed-dotted line, respectively). Parameters are set for hydrogen in EL conditions (n_0 = 3.95 x 10^5 cm^{-3}, T_0 = 200 K, r_0 corresponding to an altitude of 200 km).

In the Martian case, most collisions happen in the transitional domain (up to 600 km altitude) and below the exobase at r_0. It is then logical that the solution given by the code (in dashed red line in Figure 2.9), matches the collisionless analytic solution (in solid blue line in Figure 2.9). As in Figure 2.6, this serves as a verification of the Monte Carlo code that is described in detail in Chapter III.

Chapter III
Model and assumptions

In this chapter, both thermospheric/ionospheric and exospheric models used together in our approach, as well as how they are coupled, are presented. The main assumptions in the chemical and physical processes of the Martian upper atmosphere [*Valeille et al.* 2009a, 2009b, 2009c, 2009d] are described. Our global approach is then explained and preliminary results on the hot oxygen production in the upper thermosphere are discussed.

III.1. Thermosphere/ionosphere models

III.1.1. 1D thermosphere/ionosphere models

Even today the information about Mars upper atmosphere is very limited because of the lack of observational data, the only *in situ* measurements coming from the Viking 1 & 2 mission descents of 1976 (Figures 3.1a and 3.1b).

Neutral mass spectrometers carried on the aeroshells of Viking 1 and Viking 2 indicate that carbon dioxide is the major constituent of the Martian atmosphere in the altitude range of 120 to 200 km. The atmosphere contains detectable concentrations of nitrogen, argon, carbon monoxide, molecular oxygen, atomic oxygen, and nitric oxide. The upper atmosphere exhibits a complex and variable thermal structure and is well mixed to heights in excess of 120 km [*McElroy et al.* 1976]. Scale height extrapolations to 300 km altitude are shown in Figure 3.1a.

The first *in situ* measurements of the ionosphere of another planet were obtained by the retarding potential analyzers of the Viking Landers. These results are represented in Figure 3.1b. Both landers entered the ionosphere layer near 44° SZA, and more structure was observed in the height profiles of ionospheric quantities on Viking 2, although the profiles were similar in shape to those of Viking 1 [*Hanson et al.* 1977].

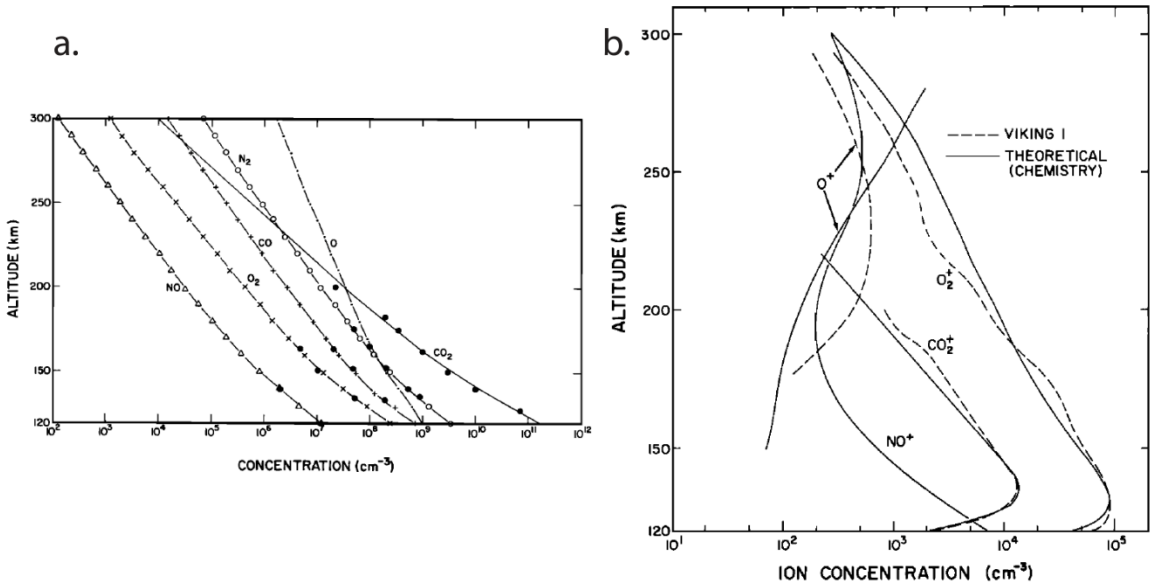

Figure 3.1. Upper thermospheric fits of the neutral (a) and ion (b) measurements made by Viking 1 & 2 descent missions in 1976 (extended to 300 km) [Source: *Hanson et al.* 1977].

A 1D description of Mars thermosphere can then be easily obtained by inferring a temperature and a density from the Viking measurements at an altitude, r_0, above the homopause and assuming a exponential decrease above it (see Chapter II),

$$n(r) = n_0 e^{-\left(\frac{r-r_0}{H_0}\right)} \tag{3.1}$$

where H_0 is the scale height at r_0, *i.e.*

$$H_0 = H(r_0) = \frac{kT_0}{mg_0} \tag{3.2}$$

Combinations of these thermosphere/ionosphere inputs [*Hanson et al.* 1977; *Nier and Mc Elroy* 1977; *Zhang et al.* 1990; *Fox* 1993a; *Kim et al.* 1998; *Krasnopolsky* 2002] were then used by 1D spherical exospheric studies [*Lammer et al.* 2000; *Nagy et al.* 2001; *Krestyanikova and Shematovitch* 2005; *Cipriani et al.* 2007] to describe the Martian

upper atmosphere. Chamberlain's theory [*Chamberlain* 1963] estimates the exospheric densities using Liouville's theorem, conservation of energy and angular momentum given the velocity distribution (*i.e.* the temperature) at the exobase (see Chapter II). Past 1D studies used a fixed exobase altitude and neutral temperature all around the planet, resulting in a 1D spherical thermal atmosphere. Reality is of course more complex, and the 3D MTGCM [*Bougher et al.* 2006, 2008, 2009a] suggests an important spatial variation of temperature at the exobase. The results show that the difference between Equatorial midnight and polar noon is of the same order as that due to solar cycle variations, making the validity of Chamberlain approach questionable.

III.1.2. 2D thermosphere/ionosphere models

Adoption of a 2D model for a description of an upper atmosphere supposes axisymmetry with respect to the Sun-Mars axis. The day-to-night difference is indeed the most obvious spatial variation expected for most celestial body.

As far as we know, the work presented in this thesis is the first and only study that uses an actual 3D thermosphere model to describe the Martian upper atmosphere [*Valeille et al.* 2009a, 2009b, 2009c, 2009d]. Past studies of high dimension [*Hodges* 2000; *Kim et al.* 2001; *Chaufray et al.* 2007] used instead a cosine extrapolation of 1D thermospheric inputs (Chapman layer).

III.1.2.1. 2D Chapman layer extrapolation of 1D thermospherics inputs

Past studies of high dimension [*Hodges* 2000; *Kim et al.* 2001; *Chaufray et al.* 2007] use very similar cosine fits of 1D inputs from various thermosphere studies to extrapolate to a 2D exospheric description on a first step, then uniformly along the azimuth to 3D.

For instance, the study of *Chaufray et al.* [2007] uses the ion profiles of *Krasnopolsky* [2002], which have been computed at 60° SZA. These profiles are assumed to be also a first order approximation for SZA < 60°. Due to rare *in situ* measurements of the Martian nightside ionosphere, they use a profile obtained by radio occultation during the Viking 1 mission for SZA = 120° [*Zhang et al.* 1990], and they also assumed that the production of

hot O from O_2^+ is negligible at 180° SZA. The other 2D studies [*Hodges* 2000; *Kim et al.* 2001] use very similar cosine fits.

The O_2^+ density profile variation with the solar zenith angle is therefore given by,

$$\begin{cases} n(O_2^+) = n_{60} & for\ 0 < SZA < 60 \\ n(O_2^+) = (n_{60} - n_{120})\cos SZA + \frac{(n_{60}+n_{120})}{2} & for\ 60 < SZA < 120 \\ n(O_2^+) = 2n_{120}\cos SZA + 2n_{120} & for\ 120 < SZA < 180 \end{cases} \quad (3.3)$$

3D thermospheric inputs from the MTGCM [*Bougher et al.* 2006, 2008, 2009a] used in this work show what a 3D density profile would look like and suggest an important spatial variation along SZA, but also from Equator to Pole, making the validity of the 1D extrapolations inappropriate for an accurate description of the sources of hot oxygen atoms in the Martian thermosphere.

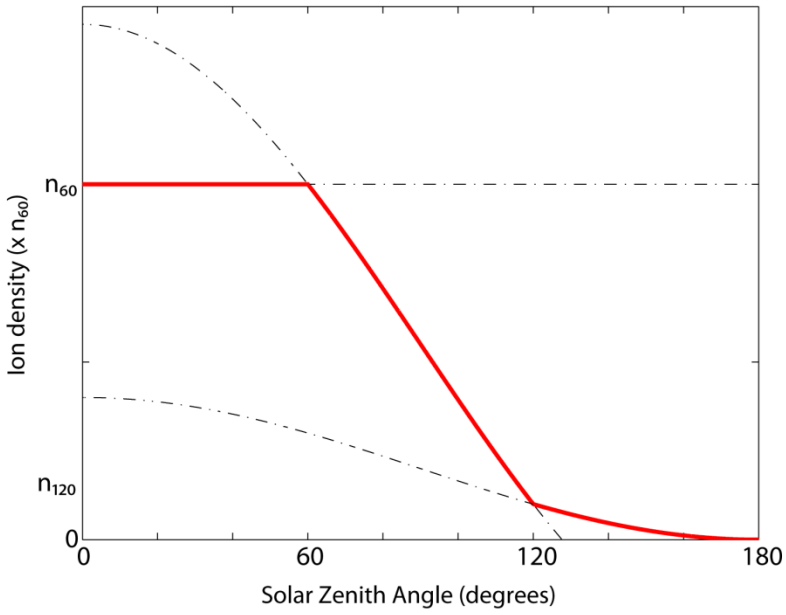

Figure 3.2. The distribution of O_2^+ ions with SZA (red line) assumed in the study of *Chaufray et al.* [2007] (the black lines are the functions used between 0-60°, 60-120°, 120-180° SZA, respectively).

III.1.2.2. 2D 'cuts' of 3D thermospherics inputs

In a very different approach, the recent studies of *Valeille et al.* [2009a, 200b], realize a pseudo-3D description using 'cuts' (*i.e.* integrated study path) through the Martian upper thermosphere from 3D thermospheric inputs (from the MTGCM). The results of this method are therefore 2D axisymmetric, but they can be run along different cuts and then compared to each other in order to describe non-axisymmetric features.

III.1.3. 3D MTGCM

The modern MTGCM is a finite difference primitive equation model that self-consistently solves for time-dependent neutral temperatures, neutral-ion densities, and three component neutral winds over the globe [*Bougher et al.* 1999, 2000, 2002, 2004, 2006, 2008, 2009a]. Prognostic equations for the major neutral species (CO_2, CO, N_2, and O) and selected minor neutral species (Ar, He, O_2, NO, N(4S)) are included. Prognostic and diagnostic thermospheric fields are simulated on 33-pressure levels above 1.32 μbar (corresponding to altitudes of ~70-200 km for low solar activity), with a 5° latitude x 5° longitude grid resolution. The vertical coordinate is log-pressure, with a vertical spacing of 0.5 scale heights.

Key adjustable parameters, which can be varied for individual MTGCM cases, include the F10.7 or E10.7 index (solar EUV/FUV flux variation), heliocentric distance (orbital variation), and solar declination (seasonal variation). At present, a simple dayside photochemical ionosphere is formulated within the MTGCM [*Bougher et al.* 2004], based upon the key ion-neutral reactions and rates of *Fox and Sung* [2001], and making use of empirical electron and ion temperatures adopted from the Viking mission. To provide solar cycle variation, the scheme adopted by *Fox et al.* [1996] is used, for which values of electron and ion temperatures are guided by Viking measurements, but tied to neutral temperatures.

A fast non-Local Thermodynamic Equilibrium (NLTE) 15-μm cooling scheme is implemented, along with corresponding near Infra Red (IR) heating rates [*Bougher et al.* 2006]. These improvements are based upon detailed one-dimensional NLTE model calculations for the Mars upper atmosphere [*e.g. Lopez-Valverde et al.* 1998].

Calculations of the MTGCM solar heating, dissociation, and ionization rates are also now improved with the implementation of the Solar2000 flux scheme [*Tobiska et al.* 2000].

The MTGCM is driven from below by the National Aeronautics and Space Administration (NASA) Ames Mars General Circulation Model (MGCM) code [*Haberle et al.* 1999] at the 1.32 μbar level (near 60-80 km). A detailed upward coupling between the MGCM and MTGCM across this boundary captures migrating, as well as non-migrating, upward propagating tides. It allows the thermal expansion and contraction of the Mars lower atmosphere with the passage of the seasons and dust events [*Bougher et al.* 2004, 2006; *Bell et al.* 2007] to extend to the thermosphere. Key prognostic (temperatures, zonal and meridional winds) and diagnostic (geopotential height) fields are passed upward at every MTGCM grid point on 2-minute time step intervals. No downward coupling from the MTGCM to the MGCM is presently activated. However, the inclusion of the Ames MGCM provides a realistic lower atmosphere that is critical for achieving an appropriate simulation of the Mars upper atmosphere within the MTGCM domain [*Bougher et al.* 2006, 2008]. Adjustable parameters in the MGCM-MTGCM include: solar flux conditions and the lower atmosphere dust prescription. Ten Martian day simulations are typically conducted for various Mars seasonal and solar cycle conditions. Model histories are archived at 1-hour intervals throughout the Martian day to capture the impact of longitude forcing upon time-dependent (specific local time) features.

It is well-documented that the dust opacity within Mars's atmosphere undergoes a strong seasonal variability as well as inter-annual variations [*Liu et al.* 2003; *Smith* 2004; *Bell et al.* 2007]. Both the horizontal and the vertical dust distributions are variable parameters that are specified in the lower atmosphere MGCM code according to recent Mars Global Surveyor (MGS) Thermal Emission Spectrometer (TES) observations [*Smith* 2004]. Lower atmosphere dust has profound impacts on MGCM-MTGCM simulated thermospheric fields [*Bell et al.* 2007].

The MGCM-MTGCM framework incorporates a detailed photochemical ionosphere, which captures the major ions, O_2^+, CO_2^+, O^+, and NO^+ below ~200 km [*Bougher et al.* 2004]. This formulation is critical to the self-consistent simulation of dayside atomic oxygen densities in the MGCM-MTGCM upper atmosphere. Atomic oxygen abundances

are inferred from UV airglow observations [*Stewart et al.* 1992; *Huestis et al.* 2008], and the uncertainty in the measurements impacts the simulation of CO_2 15-μm cooling rates in the Mars dayside and nightside upper atmospheres [*Huestis et al.*, 2008; *Bougher et al.* 2009a]. Additional MTGCM details can be found in *Bougher et al.* [2004, 2006, 2008].

III.2. Exosphere model

III.2.1. DSMC method

Today the DSMC method is the *de facto* standard numerical method for rarefied gas dynamics. Examples of the application of the method for simulation of gas flows in the cometary coma are described in the literature [*Combi* 1996; *Markelov et al.* 2006; *Crifo et al.* 2005]. One of the most important features of direct simulation methods, which are based on the Monte Carlo methodology, is that they do not require the formulation of integro-differential equations that describe the evolution of the distribution function and, as a result, can be used to solve the Boltzmann equation with a collision integral accounting for elastic and inelastic collisions.

Within the DSMC approach, the state of a rarefied gas flow is determined by the collisional dynamics of a finite number of model particles and, hence, holds the potential for providing information about gas flows, where the collision rate is not sufficient to maintain an equilibrium distribution. The key feature of the method is the separation of the translational motion from the intermolecular interaction. The general scheme of Monte Carlo models can be described by means of so-called Markov chains.

The evolution of the distribution function $f(\boldsymbol{v}, t)$ as a Markov process [*Hochstim* 1970; *Ichimaru* 1973] is described in the form of the integral,

$$f(\boldsymbol{v}, t + \Delta t) = \int f(\boldsymbol{v} - \Delta\boldsymbol{v}, t) P_{\Delta t}(\boldsymbol{v} - \Delta\boldsymbol{v}, \Delta\boldsymbol{v}) d(\Delta\boldsymbol{v}) \tag{3.3}$$

where $P_{\Delta t}(\boldsymbol{v}, \Delta\boldsymbol{v})$ is the probability for a particle having the velocity $\mathbf{v}$ at time t to have the velocity $\mathbf{v} + \Delta\mathbf{v}$ at time $t + \Delta t$. The probability $P_{\Delta t}$ obeys the normalization,

$$\int P_{\Delta t}(\boldsymbol{v}, \Delta\boldsymbol{v}) d(\Delta\boldsymbol{v}) = 1 \tag{3.4}$$

In order to apply Equation (3.3) to a real gas, a reasonable model for the transition probabilities has to be developed. Note that this formulation does not require a

simultaneous change of the velocity coordinates of both partners during a collision. In this sense, it allows description of a much wider class of relaxation processes than the Boltzmann collision integral does. In most cases of practical interest, models of microscopic processes that define the transition probability are available for rarefied gases. So, in principle, the relaxation of the distribution function in a gas can be modeled by means of the Markov chains and a numerical algorithm that is based on imitation of relaxation processes can be developed within the frame of the Monte Carlo method.

The result of a Monte Carlo numerical simulation is an averaged value of a function that gives a measurable quantity over a region of a phase space, like density, velocity, or even a velocity distribution function itself. The numerical schemes of the DSMC method [*Bird* 1994] are based on physical assumptions that form the basis for the phenomenological derivation of the Boltzmann equation. The key concept in the development of collision relaxation schemes is the total collision frequency ν. Using a probability density ω of transition from ($\mathbf{v}_i$, $\mathbf{v}_j$) to ($\mathbf{v}_i$', $\mathbf{v}_j$') for a pair of particles, the collision frequency can be defined as,

$$\nu = \frac{n}{N}\sum_{i<j}\int \omega(\mathbf{v}_i\mathbf{v}_j \to \mathbf{v}_i'\mathbf{v}_j')d^3\mathbf{v}_i d^3\mathbf{v}_j = \frac{n}{N}\sum_{i<j}\sigma_t(g_{ij})g_{ij} \qquad (3.5)$$

where g_{ij} is the relative speed between particles i and j, and $\sigma_t(g_{ij})$ is the total collision cross section. The total collision frequency given by Equation (3.5) depends on velocities of all particles. In principle, it should be recalculated after each collision, which is a rather time-consuming procedure since the summation is performed over N(N-1)/2 possible collision pairs. In order to get the correct relaxation dynamics in a gas flow, the characteristic size of computational cells must be smaller than the value of the local mean free path.

Due to the DSMC method, the translational motion is decoupled from the intermolecular interaction. During a free-molecular motion, particles change their spatial location. At the relaxation stage, the velocity coordinates of a pair of particles from the same cell can be changed due to a chosen probabilistic relaxation (*i.e.* collision) model. The conservation laws are satisfied because the post-collision velocities are determined with the use of conservation of mass, momentum and energy in every intermolecular interaction.

The code used in this thesis was adapted from the comet-coma dusty-gas DSMC code of *Tenishev et al.* [2008], which includes a very general DSMC core of routines and modules that can be applied to a wide range of applications.

III.2.2. DSMC kinetic model

The DSMC model is a 3D simulator that solves for the coupled thermosphere/ionosphere and exosphere systems using an altitude-based coordinate system. Instead of assuming a strict separation between collision and collisionless domains, the DSMC model considers a collision transitional domain where the momentum exchange within the flow is still important but the collision frequency is not high enough to maintain equilibrium in the flow. It provides a complete set of the exospheric macroscopic parameters for hot oxygen, its escape flux, and its return flux to the thermosphere.

With the DSMC method, a gas flow is represented by a set of (usually millions) model particles moving in phase space. A probabilistic technique is used to sample the state of collision partners after a momentum exchange event, to simulate scattering and chemical reactions. This approach is based on solving the Boltzmann equation and, hence, is valid for all gas flow regimes presented in the domain of study.

The code consists of a general core and a specific module for assumptions and inputs relative to Mars. It can adapt to the dimension of the thermosphere/ionosphere inputs, and therefore can be either 1D, 2D or 3D. The one-dimensional spherical case is used mostly for validation purposes and to compare with theory and previous exospheric studies (Figure 3.2). The calculations are usually made along the radial direction at the subsolar point and therefore are only functions of altitude. For test purposes, calculations of different past approaches [*Hodges* 2000; *Nagy et al.* 2001] were performed and compared with the DSMC code, and the match gave a good validation of our computational approach and computer code. In the two-dimensional case, the global distributions of the atmosphere and ionosphere are approximated as being axisymmetric about the Sun-planet line and hence are functions of SZA and altitude. The horizontal wind parameter corresponds either to the zonal or meridional component of the MTGCM for simulations

along the Equator or the Pole, respectively. The MTGCM includes effects of planetary rotation in its thermospheric description. However, being a pure 3D effect, the rotation effect was not included in the axisymmetric calculations. It has no influence for simulations along the Pole and its effect is averaged out for Equatorial simulations. In the three-dimensional case, a full simulation is possible, including dynamical effects, planetary rotation, hemispheric asymmetries and any 3D localized features in general.

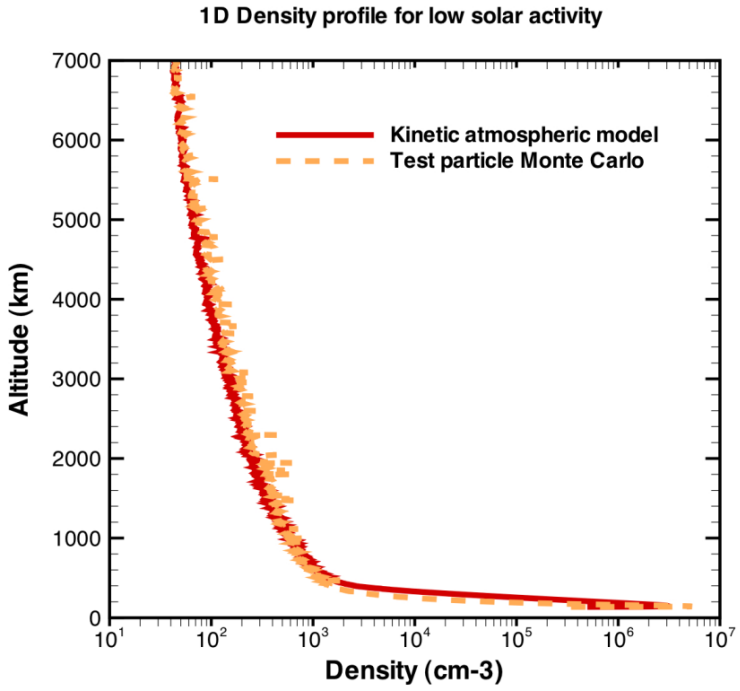

Figure 3.3. Validation of the code using 1D thermospheric inputs. The density profile obtained from the DSMC code is represented in red solid line, whereas results from a simple code using 1D Chamberlain approach are in dashed orange line.

III.3. Unstructured mesh

Mars exosphere calculations were done using either a 2D axisymmetric mesh to 10 radii or a 3D mesh to 3 radii to compute an exospheric description. Both are presented in this section.

III.3.1. 2D mesh

The 2D mesh is an unstructured mesh of triangular cells that allows a pertinent description of the domain around complex 2D bodies, and can be easily adapted to the physical features of the problem. The mesh presents uniformly spaced cells matching the resolution of the MTGCM in the transitional domain, followed by exponentially distributed cells beyond the exobase, as shown in Table 3.1, allowing an approximate constant number of atmospheric particles per cell (around 20 particles per cell). The typical size of a cell, which is determined by the local mean free path, varies typically from a minimum of 1 km to a maximum of 1000 km, corresponding to the bottom (135 km altitude) and top (10 Martian radii) of the mesh respectively, resulting in a total of about 200,000 cells or 4 million particles simulated. The size of the simulation domain was limited to 10 Martian radii to keep the two-body approximation valid.

III.3.2. 3D mesh

The code uses an unstructured mesh of tetrahedral cells that allows a pertinent description of the domain around complex 3D bodies (a section of it is shown on Figure 3.4). It can be easily adapted to the physical features of the problem, and takes into account the variations of the outputs of interest.

The mesh is first generated in hexagonal cells. The three spatial dimensions of a typical cell of the mesh shall match the three local characteristic lengths of the 3D problem. The angular resolution matches that of the thermosphere model, being a 5° x 5° grid (*i.e.* about 300 km x 300 km at the Equatorial surface) all across the simulation domain. However, to capture the critical variations in density with altitude satisfactorily, the radial resolution should be less than about one half to one third of the local temperature scale height in the transitional domain. The mesh presents uniformly spaced cells distributed radially from the inner boundary (at 135 km) to 200 km with a 4 km altitude resolution, followed by exponentially distributed cells beyond the 200 km altitude, as shown in Table 3.1. This allows for an approximately constant number of atmospheric particles per cell (mostly ~20-40 particles per cell). Each of those stretched hexagonal cells is then split into six tetrahedral cells.

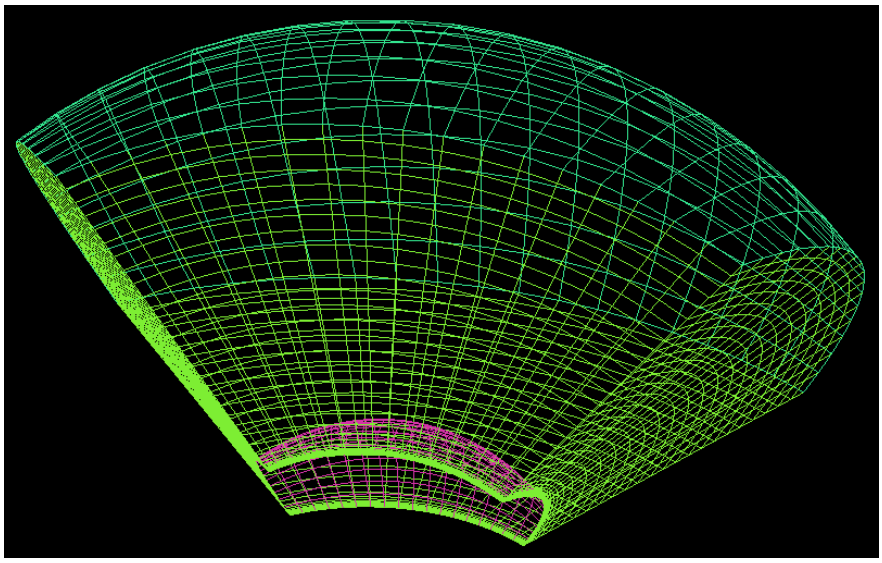

Figure 3.4. Section of the 3D tetrahedral mesh. The lower boundary at an altitude of 135 km is represented in pink, the internal cells in light green, and the upper boundary at the altitude of 2 radii (*i.e.* 3 radii from the center of the planet) in dark green.

It should be noted that to keep the same 5° x 5° angular resolution from 2D to 3D, a factor 72 in the number of the cells is needed when building a mesh. A factor 3 should be also considered to go from 2D triangular to 3D tetrahedral cells. To keep a reasonable computing time and expense, a limitation in the size of the mesh and a decrease in the radial distribution compared to the 2D mesh [*Valeille et al.* 2009a, 2009b] are adopted. The 2D results are however reproduced by corresponding 3D simulations within less than a 5% error. The two main processes for the generation of the exospheric population, *i.e.* production (via O_2^+ DR) and collision (with O and CO_2 background species), are well simulated. The size of the simulation domain is limited to a 3-Mars-radius domain of interest for most studies in order to limit the computational time and to keep the two-body approximation valid. A total of about 500,000 cells, or 30 million particles, is simulated.

Table 3.1. Illustration of the necessity of combining hydrodynamic and kinetic models to describe rigorously both transitional and collisionless regions [adapted from *Valeille et al.* 2009a]

	Kn<<1	Kn~1	Kn>>1
Model	DSMC (Boltzmann equations)		
Inputs	MTGCM		no
Mesh	Structured		Unstructured
Location	Thermosphere		Exosphere
Collision	Transitional domain		Collisionless
Hot O Production	yes		no
Altitude (km)	135	200 600	7000

The Knudsen number, $Kn = \lambda / H$, is a dimensionless number defined as the ratio of the molecular mean free path length λ to the scale height H, a representative physical length scale. Collisionless kinetic theory models, used to describe the exosphere, are valid in the limit $Kn \to \infty$; whereas hydrodynamic models, such as the MTGCM, are used to describe the thermosphere and are valid when the mean free path λ is very small and $Kn \to 0$. However the Boltzmann equation of kinetic theory is valid for the whole range of Knudsen numbers and is solved by the DSMC code.

III.4. O_2^+ Dissociative Recombination (DR)

For present Mars conditions, O_2^+ DR is by far the most important source of hot oxygen in the Martian thermosphere. Therefore, the O_2^+ ionospheric density profile is a critical parameter for the simulation. The relative importance of the second, third and fourth hot oxygen sources and escape processes by ion loss, sputtering and Energetic Neutral Atoms (ENA) mechanisms, respectively, were the object of a recent extensive 3D study describing the interaction of the solar wind with the Martian corona [*Chaufray et al.* 2007]. Their cumulative effect is smaller by at least one order of magnitude than the contribution due to O_2^+ DR for modern conditions [*Leblanc and Johnson* 2001; *Chaufray et al.* 2007], and they are therefore neglected in this study. It can be noted that these models are in reasonable agreement with several reported observations made by the Phobos 2 and Mars Express missions [*Lundin et al.* 1989; *Barabash et al.* 2007; *Lundin et al.* 2008]. Ionospheric outflow is not considered in this work as it is shown to be about an order of magnitude less than even the secondary processes, both at present and in the past. The study of *Chassefière et al.* [2007] shows such a comparison using the results of *Ma et al.* [2004].

The excess energies (in square brackets) and the measured branching ratios (in parentheses) of *Kella et al.* [1997] are used for the main branches of the O_2^+ DR reaction:

$$O_2^+ + e \rightarrow \begin{cases} O(^3P) + O(^3P) + [6.98eV] & (.22) \\ O(^3P) + O(^1D) + [5.02eV] & (.42) \\ O(^1D) + O(^1D) + [3.05eV] & (.31) \\ O(^1D) + O(^1S) + [0.83eV] & (.05) \end{cases} \quad (3.6)$$

It is important to note that the O_2^+ DR reaction rate coefficient, used by the thermosphere/ionosphere model for O_2^+ loss and by the exosphere model for the hot O source, should be consistent [*Valeille et al.* 2009a; *Fox*, private communication 2009]. In this work, this common value is taken from *Mehr and Biondi* [1969]:

$$\begin{cases} \alpha = 1.95 \times 10^{-7} \, (300/\mathrm{Te})^{0.7} & \mathrm{cm^3\ s^{-1}} \quad \text{for Te} < 1200\ K \\ \alpha = 0.75 \times 10^{-7} \, (1200/\mathrm{Te})^{0.56} & \mathrm{cm^3\ s^{-1}} \quad \text{for Te} > 1200\ \mathrm{K} \end{cases} \quad (3.7)$$

When the electron density is used in the thermosphere inputs, instead of assuming O_2^+ as dominant ion, it leads to a ~10% increase in the production, in agreement with Viking measurements that suggested that O_2^+ constitutes about 90% of the total ion density [*Hanson et al.* 1977]. It is important to note that the adoption of the most recent (and controversial) rate factor [*Peverall et al.* 2001] of 2.4 x 10^{-7} $(300/\mathrm{Te})^{0.7}$ $\mathrm{cm^3.s^{-1}}$ might enhance the escape rates by 20% (as they are proportional to the hot oxygen density). In this study, conservative estimates are used to underline the importance of O_2^+ DR compared to secondary processes for oxygen escape. Therefore, the smallest O_2^+ DR coefficient is taken.

III.5. Global approach

The different cases considered in this thesis are first simulated in 3D with the MTGCM. All the thermospheric parameters were then compiled in regular arrays matching the model resolution: 5° in latitude and longitude and 1 km in altitude (from 135 km to 200 km). Extensions to 600 km altitude for density profiles are calculated using the local density scale height. Those parameters were the ones needed to describe the hot oxygen atomic production and collisions with the background species in the

thermosphere: O_2^+, O and CO_2 densities, neutral, ion and electron temperatures, horizontal and vertical winds.

III.5.1. Transitional domain

Instead of seeing the exobase as a level at a fixed altitude separating the collisional thermosphere and collisionless exosphere where hot particles are injected as a function of their distribution, a region, which will be called a transitional domain, is considered. The two main factors responsible for the formation of the hot corona, *i.e.* production and collision, occur mostly here. It overlaps with the upper thermosphere that is described by the MTGCM and used as inputs. A traditional collisionless domain describes the exosphere above it. The transitional domain, where collisions although rare still occur, extends from its lower boundary at the altitude of 135 km, under which the produced particles are assumed to be thermalized before they reach the exobase (the typical average number of collisions being above ten), and its upper boundary at 600 km, where the concentration of background species is considered too low to consider collisions anymore (the collision frequency being negligible). This range of altitudes defining the domain was also found optimal after different test runs and is confirmed once again by a spatial profile of hot oxygen production in next chapter.

No iteration with the MTGCM code is considered in this study. However, a preliminary simulation of the energy deposition of the return flux in the thermosphere showed that hot particle precipitation might be comparable to the main heat sources on the nightside (see Section IV.1).

III.5.2. Cold and hot particles

In the simulation cells of the transitional domain, two new oxygen atoms are created for each O_2^+ ion at a random location within the cell if the probability of the event occurrence is verified by Equation (3.5) at that place and during the time step. Ion temperatures and horizontal and vertical wind velocities at this point are used to generate random velocities for the reactants. The exothermic energy that is derived between the pair of new hot atoms is set by the probability distribution of the branching ratios in Equation (3.6).

By momentum conservation, the excess energy from Equation (3.6) is divided equally between each of the fast neutral oxygen atoms created and moving in opposite directions in the frame of reference of the parent ion. The exothermic velocities of the first two most energetic branches of the reaction, which account for 64% of O_2^+ DR, exceed the escape velocity at the Martian exobase (5 km s^{-1}, *i.e.* 2 eV for O). However most of those particles will lose energy and most likely be thermalized by collisions with the background gases (*i.e.* atomic oxygen and carbon dioxide) in the transitional domain before they reach its upper boundary, beyond which they finally escape if their remaining energy is sufficient.

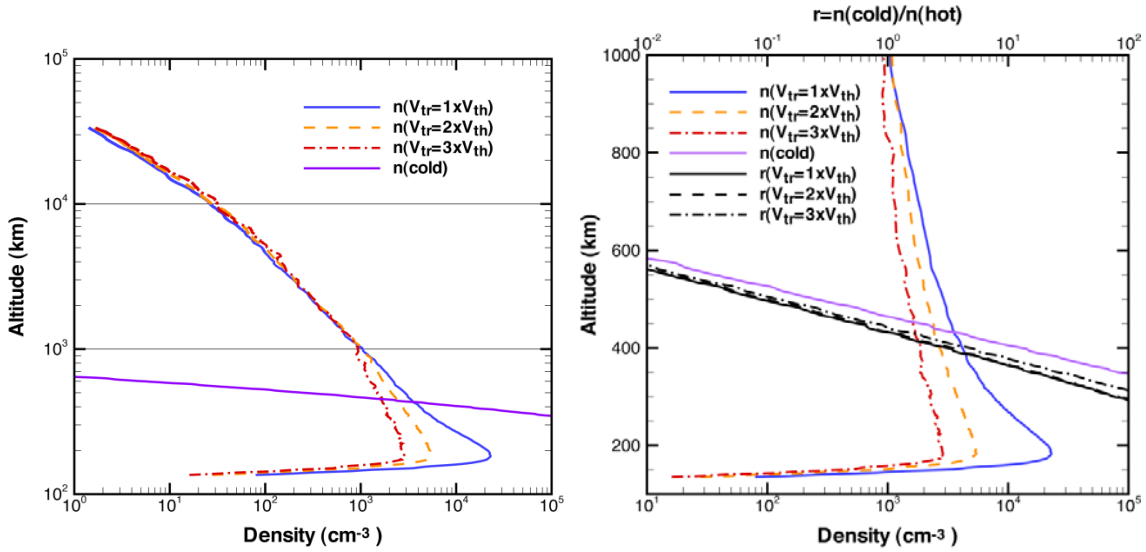

Figure 3.5. Density profiles and cold/hot ratios for different definitions of hot oxygen between 100 and 100,000 km altitude (a) and between 100 and 1000 km altitude (b).

In this work, a particle is considered to be part of the hot population if its speed remains above a local characteristic speed, $V_{threshold}$, in the transitional domain. The definition of $V_{threshold}$ is somewhat arbitrary, but should remain between the local thermospheric thermal speed, V_{th}, and the escape speed, v_{esc}. Most past studies used a convenient speed that shortens their computational time. In this work, three different cases were studied for a better understanding of the impact of the definition on the results.

Figures 3.5a and 3.5b show results of three simulations, where $V_{threshold}$ is set up to 1x V_{th} (blue solid line in Figures 3.5a and 3.5b), 2x V_{th} (orange dashed line in Figures 3.5a and 3.5b) and 3x V_{th} (red dashed-dotted line in Figures 3.5a and 3.5b). The density of the

cold thermospheric atomic oxygen is also shown for comparison (purple solid line in Figures 3.5a and 3.5b).

Above an altitude of 1000 km, no significant difference can be seen between the density profiles of the three definitions adopted and the speed of all oxygen particles are therefore above 3x V_{th} (Figure 3.5a). By contrast, density profiles part from each other in the region below 1000 km (Figure 3.5b) and the difference is as high as one order of magnitude at the exobase between 1x V_{th} and 3x V_{th}. It can be noted that a 1x V_{th} cutoff might artificially take too much of a part of background species (which densities are fixed by definition) into account. The difference in the density profiles between the 2x V_{th} and 3x V_{th} cases is smaller than the one between 1x V_{th} and 2x V_{th}, and it can be inferred that for a threshold higher than 3x V_{th}, density profiles should not change significantly.

Table 3.2. Number of iterations reached by a simulation, function of $V_{threshold}$

$V_{threshold}$	1x V_{th}	2x V_{th}	3x V_{th}	v_{esc}
Iterations	12 000	17 000	18 000	40 000

$V_{threshold}$ is usually set to twice the local thermal speed and corresponds to less than the hottest 1% of the Maxwellian distribution of thermospheric particles. This definition also ensures a clear separation between hot and cold species in determining the total density profile for oxygen. Furthermore, for specific evaluation of the escape rate only, $V_{threshold}$ can be set as high as the local escape speed, which allows saving of more than half of the computational time to reach equilibrium (Table 3.2).

The trajectory of each hot atom in the gravitational field of Mars is traced from collision to collision until it escapes at the external boundary, r_{ext}, of the domain of study (*i.e.* 3 or 10 radii for a 2D or 3D simulation, respectively), becomes part of the thermosphere when its speed falls below $V_{threshold}$, or becomes ionized in the sunlit portion of the exosphere. Subsolar photoionization rates are assumed at 5.9 x 10^{-7} and 2.7 x 10^{-7} s^{-1} for solar high and low, respectively, as derived from *Hodges* [2000], and changed accordingly with the heliocentric distance of the orbital position considered.

III.5.3. Collision process

Scattering collisions are approximated as elastic hard sphere encounters [*Nagy et al.* 1981]. *Krestyanikova and Shematovitch* [2005] noted that the collision cross sections are critical parameters. Values of the O/O collision cross sections found in the literature vary from 1.2 to 3 x 10^{-15} cm^2 [*Lammer et al.* 2000]. In this study, both O/O and O/CO_2 collision cross sections are 2 x 10^{-15} cm^2, derived from *Kharchenko et al.* [2000] (Figure 3.6), and consistent with the values of *Hodges* [2000]. In Figure 3.6a, the O-O statistically averaged elastic cross section is between 6 and 9 x 10^{-15} cm^2 for the range of energy of consideration, *i.e.* between 0.4 and 3.5 eV from the DR branching ratios (3.4). Figure 3.6a shows the differential cross section (in cm^2 str^{-1}) and most of the contribution is due to low scattering angle (less than 30°). Between 0 and 30°, there are more collisions, but less deflection and loss of energy, so not that much change. In a sense, a strong forward peak is essentially like little or no deflection, *i.e.* almost like no collision. Provided our cross section is somewhat smaller than the detailed one of *Kharchenko et al.*, the simulation results should not change much. An integration over the remaining 30-180° of an approximate 1 - 2 x 10^{-16} cm^2 str^{-1}, leads to 1.3 - 2.5 x 10^{-15} cm^2, close to the adopted 2 x 10^{-15} cm^2 value.

Hot atoms can also be created by fairly direct collision of the hot particles with the background thermospheric oxygen atoms if the speed of the colliding background atom is above $V_{threshold}$. This secondary source of hot oxygen atoms is found to be far from negligible and accounts for about 20% of the total escape [*Hodges* 2000, *Valeille et al.* 2009a].

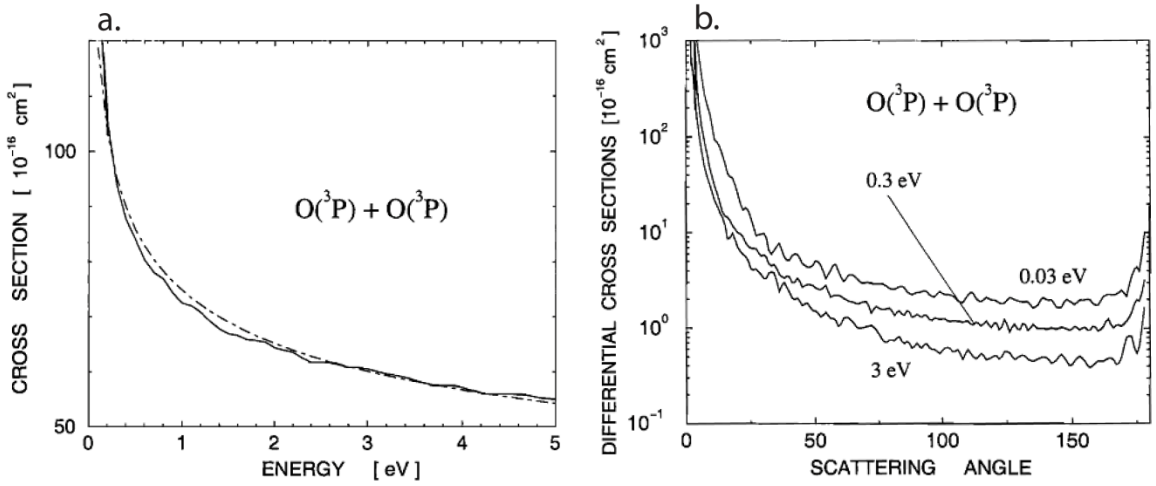

Figure 3.6. Statistically averaged elastic (a) and differential (b) cross sections of oxygen atoms, as a function of the relative energy (a and b) and of the scattering angle (b). The dashed curve shows the cross sections calculated with the Landau-Schiff approximation [Source: *Kharchenko et al.* 2000].

Unlike previous approaches, all the thermospheric parameters needed to calculate production and collision of hot oxygen in the transitional domain were taken from the same and unique source, the MTGCM model, without any extrapolation, making them very consistent with each other. The nightside ion concentration is assumed to be negligible (compared to the dayside), and the terminator clearly delimits the illuminated and dark side of the planet.

III.5.4. Framework

In this work, the 3D cartesian frame for the exosphere description is associated with the Sun. It has its origin at the center of the planet, the X-axis pointing towards the Equator at noon (in case of equinox, this would be towards the Sun), the Y-axis towards the east terminator and the Z-axis towards the North Pole. Latitudes are counted positively in the North hemisphere (0° to +90°, from Equator to North Pole) and negatively in the South hemisphere (0° to -90°, from Equator to South Pole). Longitudes are counted from the meridian taken here, for simplicity sake, as the half of the great circle going through the subsolar point (*i.e.* the noon meridian). They are counted

positively towards East (0° to +180°, from noon to midnight through dusk) and negatively towards West (0° to -180°, from noon to midnight through dawn).

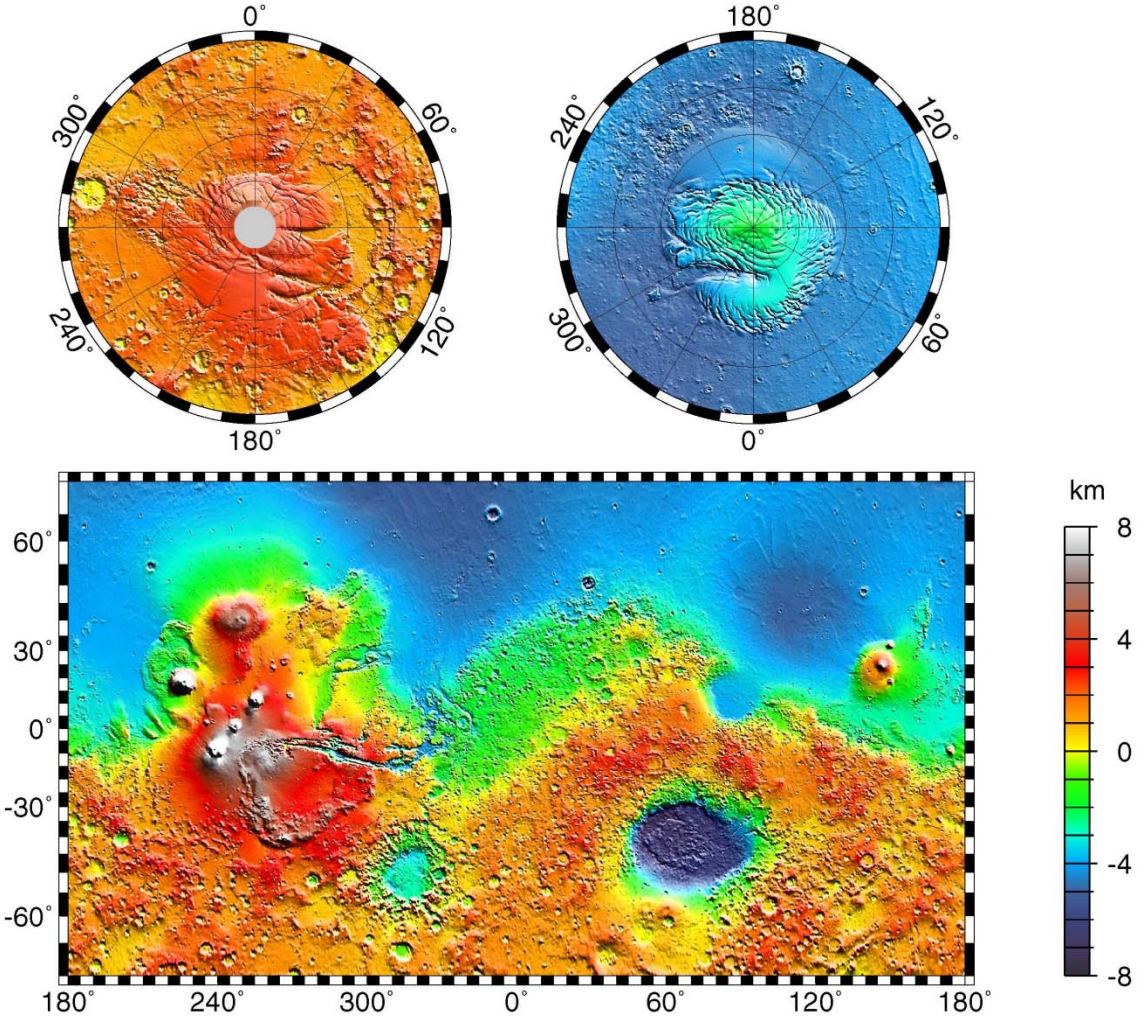

Figure 3.7. Maps of Mars global topography. The projections are Mercator to 70° latitude and stereographic at the Poles with the south Pole at left and north Pole at right. Note the elevation difference between the northern and southern hemispheres. This analysis uses an areocentric coordinate convention with east longitude positive. [Source: http://photojournal.jpl.nasa.gov/jpeg/PIA02031.jpg].

The frame associated with Mars can also be considered for the thermosphere description and rotates around the Z-axis with a sidereal rotation period of ~24.6 h towards East (like Earth), *i.e.* at an Equatorial surface speed of ~240 m s^{-1}. Rigorously, since the topography of the planet (Figure 3.6) affects the lower atmosphere, that in turn impacts the thermosphere, results should vary during the course of a planet day. In this

framework, steady-state is assumed (*i.e.* the results will not be affected by the longitudinal variations during the course of a planet day), and the 0° longitude is fixed at local noon (UT = 12).

III.5.5. 3D validation

As this work is the first 3D coupled description of the Martian thermosphere/ionosphere and exosphere, a comparison can only be made with a similar study of lower dimension. The model presented here was previously run along 2D axisymmetric 'cuts' through the Martian upper atmosphere in the framework of the study of *Valeille et al.* [2009a]. Those results were reasonably consistent with most of the works of the last ten years [*Kim et al.* 1998; *Lammer et al.* 2000; *Hodges* 2000; *Kim et al.* 2001; *Krestyanikova and Shematovitch* 2005; *Cipriani et al.* 2007; *Chaufray et al.* 2007]. The coupling of 3D thermospheric/ionospheric inputs with a 2D exospheric description suggested in particular that varying Equatorial longitude and polar latitude cuts (study path from 0° to 180° SZA along the Equator or through the Poles) presented the greatest contrast of thermospheric/ionospheric features and are essentially the two extreme spatial dimensions of the Martian upper atmosphere environment [*Valeille et al.* 2009a]. These significant differences (yielding about a 30% change in the local escape flux), explained by the seasonal features in the lower atmosphere and the polar warming effect [*Bougher et al.* 2006], illustrate that the use of a 3D model is more appropriate to account for spatial variations of thermospheric/ionospheric parameters. The profiles of the macroscopic exospheric parameters are not homogeneous with respect to the location and a two-dimensional axisymmetric model may be insufficient to describe in detail the entire Martian exosphere.

For testing purposes, the 2D exospheric results of the study of *Valeille et al.* [2009a] with respect to SZA were first reproduced using the full 3D code for the fixed orbital position of equinox for solar low conditions (EL case). Calculations were then performed with full 3D thermospheric/ionospheric inputs with the current 3D DSMC model and compared with the previous 2D axisymmetric calculations along both Equatorial and polar cuts. The integration of the hot oxygen escape flux of our 3D simulation appears

between the two extreme spatial cuts as defined and expected by the 2D study of *Valeille et al.* [2009a], providing a good validation of the computational approach and computer code of the current 3D model.

III.6. Ionization

A substantial nonthermal escape process at essentially unmagnetized planets, such as Mars, is ion pickup by the solar wind [*e.g. Luhmann and Kozyra* 1991]. Coronal atoms can be removed by the solar wind if they are ionized above the ionopause where they are picked up by the motional electric field ($\mathbf{E} = -\mathbf{v} \times \mathbf{B}_{IMF}$) [*Zhang et al.* 1993a, 1993b]. Using the oxygen densities in the calculated exosphere and upper thermosphere, the ion production rates can be integrated above an assumed ionopause at different altitudes to find potential loss rates due to solar wind scavenging of O^+ ions. The ion production mechanisms considered here are photoionization (PI) by solar EUV radiation, charge exchange (CE) with solar wind protons; and electron impact ionization (EI) by solar wind electrons, as explained in detail in the study of [*Valeille et al.* 2009b].

The photoionization process is described by the reaction,

$$O + h\nu \rightarrow O^+ + e \qquad (3.8)$$

The present-day photoionization frequency for O at solar low (Viking lander conditions) of ~2.4 x 10^{-7} s^{-1} [*Torr and Torr* 1985] at a heliocentric distance of 1 AU, adjusted for the heliocentric distance of Mars, is ~1.0 x 10^{-7} s^{-1}. The charge exchange process produces the transformation,

$$H^+ + O \rightarrow \quad H + O^+ \qquad (3.9)$$

with a charge exchange ionization frequency given by $\rho_{sw} v_{sw} \sigma_{sw}$, where ρ_{sw} is the solar wind proton plasma density, v_{sw} is the solar wind plasma velocity, and σ_{sw} = 8 x 10^{-16} cm^{-2} is the cross section of O for charge exchange with protons [*Stebbings et al.* 1964]. In the electron impact ionization process,

$$O + e \rightarrow O^+ + 2e \qquad (3.10)$$

the ionization frequency per electron is a function of electron temperature [*Cravens et al.* 1987; *Bailey and Sellek* 1990]. This value has to be multiplied by the solar wind electron

density to obtain the ionization frequency. The solar wind plasma temperatures, density and velocity are altered in the magnetosheath where the flow is diverted around the planetary obstacle [*e.g. Ma et al.* 2004].

Estimated positions of the ionopause and bow shock [*Zhang et al.* 1993; *Leblanc and Johnson* 2001; *Trotignon et al.* 2006] are used (Figure 3.8). In the region between the ionopause and the bow shock, the solar wind velocity and density are estimated to be 0.25 and 4 times their respective values above the bow shock in each case.

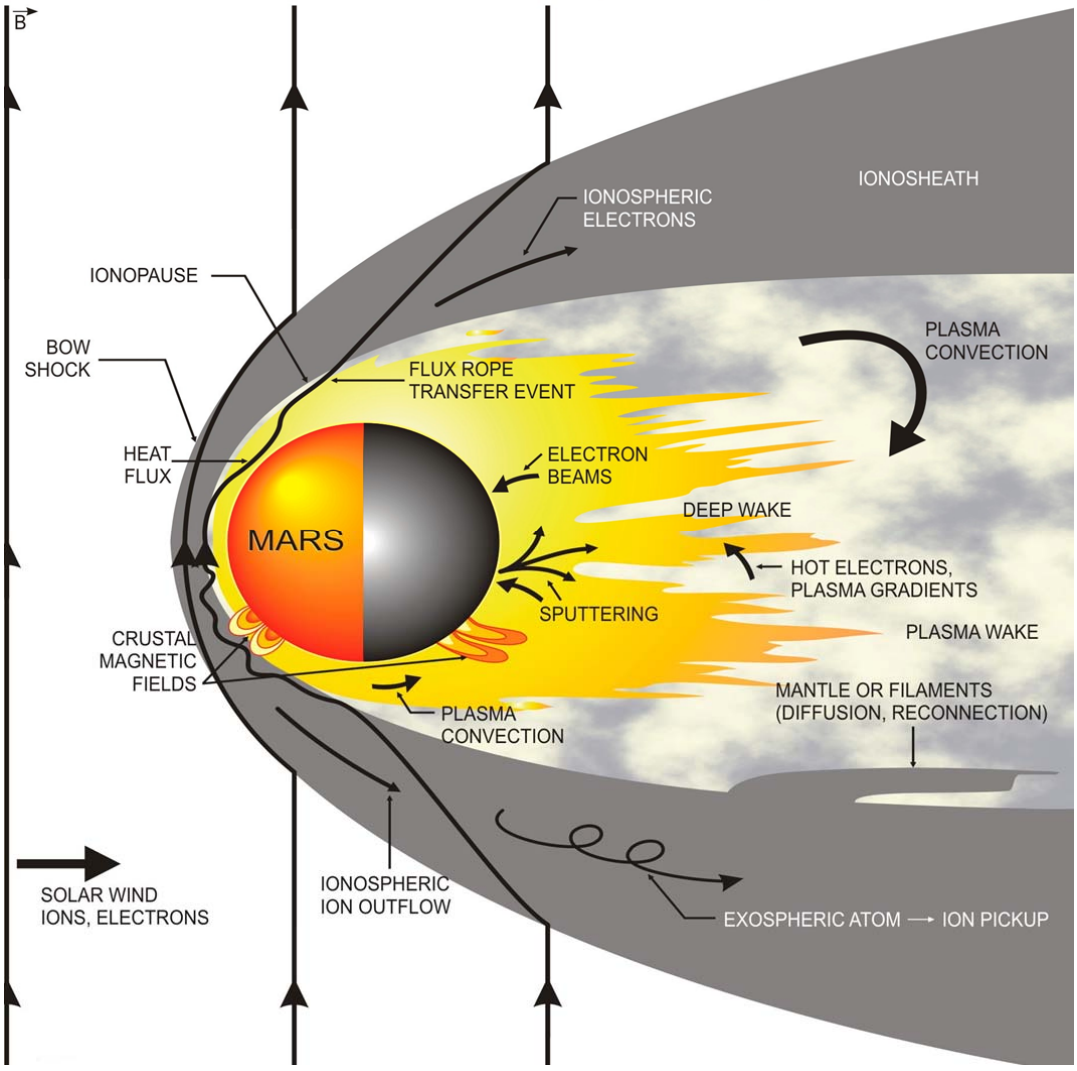

Figure 3.8. Illustration of the solar wind interaction on Mars.

III.7. Preliminary results

A complete 2D map of the upper thermospheric hot oxygen production rate is extracted from the MTGCM direct output as a function of SZA. In the collision transitional domain, O_2^+ is the major ion, and electron number density to first order almost equals its density. Therefore, the O_2^+ DR increases in proportion to the square of the O_2^+ density Equation (3.6). In our MTGCM model, ions are assumed absent in the nightside. While more realistic conditions would not change the global results significantly, local electron precipitation due to crustal magnetic fields are likely to affect the corona densities in the nighside and would be a matter of future work. Figure 3.9 shows that the nightside production of hot oxygen atoms is null, and more specifically that most of the production occurs deep in the thermosphere well below the neutral exobase on Mars, between noon (0° SZA) and 3 pm (45° SZA) and between 135 and 145 km altitude. Hot oxygen production decreases greatly with altitude, and is nearly nonexistent in the vicinity of the exobase (set as 190 km altitude for comparison sake). Therefore it can certainly be assumed null beyond 300 km, providing a good confirmation of the previous definition of the upper boundary of the transitional domain. Being the peak of the ion density on Mars [*Hansen et al.* 1977], the 135 km altitude also corresponds to the peak of the hot oxygen production, which decreases below this altitude. Moreover, the number of particles produced at this altitude that reach the exobase with sufficient energy to escape is negligible. In addition, the average number of collision encounters with the cold ambient neutral gases in this region is above ten. Those two facts also give a strong validation of the altitude of the lower boundary.

Extending the transitional domain above the exobase from 190 km to 300 km altitude increases the total production by less than 2%. However at those altitudes, the collisions are negligible and this fraction of produced particles accounts for a noticeable part of the escape flux. Extending the limit of the transitional domain further up does not change the results significantly (representing less than 4% increase of the total escape rate in the most extreme case). It follows that production above the exobase should be taken into account, as addressed by *Hodges* [2000] and *Kaneda* [2007], and in the discussion below. It is important to note that the collisions right above the exobase, although less likely to

occur than below, are critical to determine the escape rate, as one collision with a thermal particle is generally sufficient for a hot particle to fall below the local escape speed.

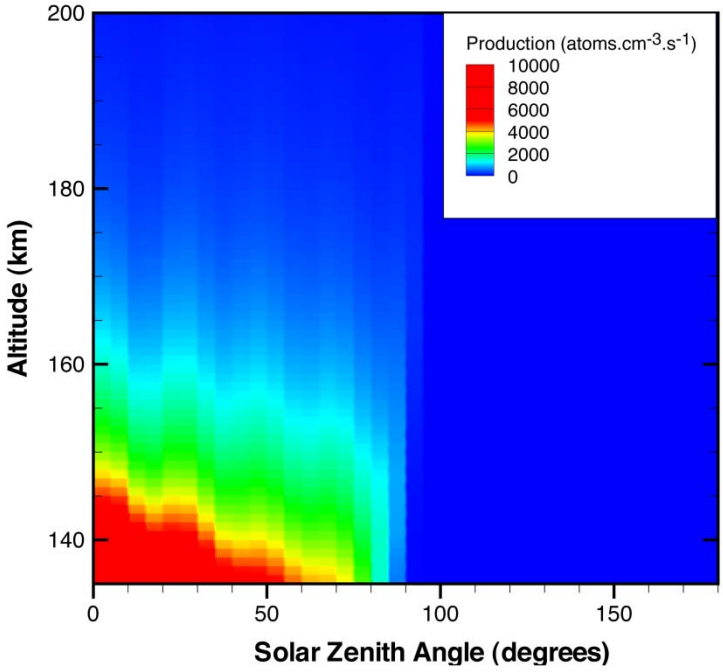

Figure 3.9. Production rate as a function of SZA (along east Equatorial cut) and altitude in the upper thermosphere region (from 135 to 200 km altitude) at fixed orbital position of equinox for solar high conditions (EH case).

Chapter IV

General description and results at equinox for solar low conditions

In this chapter, calculations for fixed orbital position of equinox and for solar low conditions (EL case) are presented and discussed. These specific conditions, corresponding to the only *in situ* measurements available today (the ones of the Viking mission descents in 1976), have been systematically used in the past by modelers and therefore serve as the best example of this work to illustrate the general structure and attributes of a 3D exosphere produced by a self-consistent 3D thermosphere/ionosphere model [*Valeille et al.* 2009a, 2009c]. This case will often be used as a reference throughout the next chapters.

IV.1. Thermosphere/Ionosphere

In this section, the description of the thermosphere by the modern 3D MTGCM is presented. It includes maps of the main macroscopic physical parameters, such as CO_2, O and O_2^+ density profiles, neutral, ion and electron temperatures, and winds, as functions of position on the planet, in the frame associated with Mars. For comparison sake (with Viking measurements and with other models), all calculations are run at the fixed orbital position of equinox and for a low solar activity (*i.e.* solar longitude, Ls, of 180° and F10.7 cm of 70 at Earth).

IV.1.1. Temperatures and winds

The map of simulated MTGCM neutral temperatures in the isothermal region of the Martian upper atmosphere is presented in Figure 4.1. The average temperature, T_∞, of about 170-180 K is mostly located at low and mid latitudes on the dayside and high latitudes on the nightside (green areas in Figure 4.1). High temperatures are found on the dayside along the terminator (yellow areas in Figure 4.1), with maxima of about 250-290 K being at the polar regions and in the vicinity of the evening terminator (red areas in Figure 4.1). Minima of about 115-130 K are situated in the southern hemisphere, at low and mid latitudes on the nightside (blue areas in Figure 4.1).

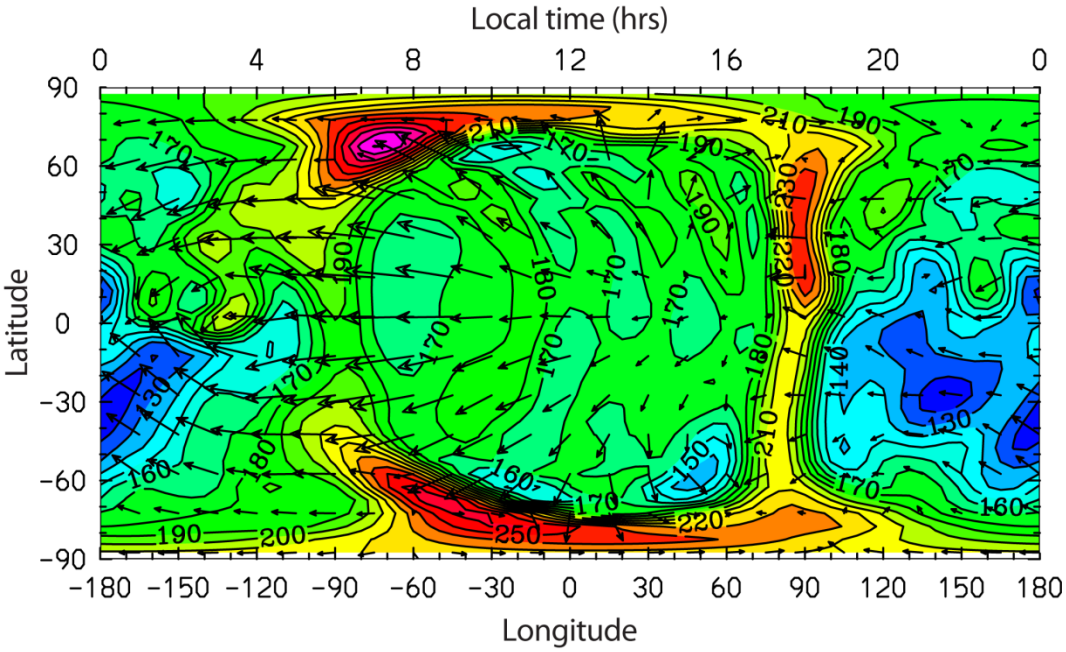

Figure 4.1. Neutral temperature at an altitude of 190 km. Horizontal wind velocities are represented in the frame associated with Mars by arrows (maximum of ~490 m s^{-1}). Minimum temperatures are in blue and correspond to 115-130 K, while maximum temperatures are in red and correspond to 250-290 K (10 K increments).

Day and night time Martian thermospheres were shown to follow similar profile trends in the 120-280 km region, revealing neutral temperature increases with altitude first, and then becoming isothermal above some level [*Valeille et al.* 2009b]. This level is reached at lower altitudes at night (140-150 km) compared to day (160-170 km). However, it is important to note that the upper atmosphere presents an isothermal

structure up to a certain altitude, where the temperature profile presents a sharp transition between the cold and hot populations. This transition occurs at altitudes of about 400-600 km for the conditions considered and is further discussed in Section IV.2.5.

A 3D simulation permits the incorporation of the effects of dynamics, which play an important role, especially for the transport of light species. Dynamics can also be seen as a thermostat, changing the heat budget from the dayside to the nightside. Indeed, while thermal conduction heats the nightside, it is also a major cooling mechanism together with CO_2 IR 15-μ cooling on the dayside, balancing the solar heating due to EUV and NIR radiation.

In the frame associated with Mars, although the Coriolis effect can be seen at high latitudes as a deviation to the right in the north hemisphere and to the left in the south (see Figure 4.1), thermospheric winds flow essentially westward at low to mid latitudes. While the wind speed reaches its minimum along the evening terminator, a maximum of about 490 m s^{-1} is located along the morning terminator. At the Equator, in the vicinity of the exobase, the planetary rotation speed of 240 m s^{-1} is comparable to the average thermospheric wind speed, but is oriented in the opposite direction. Therefore, in the frame associated with the Sun, the cumulative effect of winds and planetary rotation can be roughly seen as a diurnal tide, as thermospheric flow diverges essentially from near the warm subsolar point (*i.e.* 0° SZA) and converges near the antisolar point (*i.e.* 180° SZA) on the nightside. While such a simple assumption is correct to first order, the inputs used in this research account for more complex local features, as shown in Figure 4.1.

Jeans escape is very temperature dependent and, because the thermal contrast in the exosphere can be very important (more than 120 K between extrema, according to Figure 4.1), its spatial variations are dramatic. However, even at its local maximum, the thermal escape remains orders of magnitude smaller than non-thermal processes for atomic oxygen. For lighter species, such as hydrogen, Jeans escape can vary as much as a factor of about x150 for constant bulk density from one location to another. Therefore, accounting for these important variations, the 1D Chamberlain approach used by all hydrogen studies to date [*e.g. Anderson and Hord* 1971; *Anderson* 1974; *Nagy et al.* 1990; *Lichtenegger et al.* 2004; *Chaufray et al.* 2007], and which assumes constant exospheric temperatures and spatially uniform densities, can only provide a one to two

order of magnitude estimate of escape at best. A 3D coupling of both thermosphere and exosphere, as well as a better understanding of the spatial density distribution of atomic hydrogen would be helpful in order to obtain a better characterization of the hydrogen escape.

IV.1.2. O and CO_2 density distribution

The two main constituents in the Martian upper thermosphere are CO_2 and O. Interestingly, although they exhibit a similar average abundance at an altitude of 190 km, their local distribution is very different. The CO_2 molecule is heavier; therefore its concentration is more responsive to the local background temperature. Atomic O is lighter, and thus more responsive to transport (*i.e.* to local temperature gradients). These responses should be put in context using the map of temperature and winds (Figure 4.1) in order to understand the variations in density presented in Figure 4.2 (all parameters are shown at the same altitude of 190 km in both figures).

Atomic oxygen reaches its maximum densities at low latitudes on the nightside near the morning terminator (yellow-orange areas in Figure 4.2), whereas minima are achieved on the dayside close to the evening terminator (light blue areas in Figure 4.2). These extrema occur at the same positions as the strong convergent nightside and weak divergent dayside winds, consistent with the fact that O density variations are driven by the effect of dynamics. As a result, O density variations are also lower (factor ~10 between extrema) and smoother than the heavier CO_2 (factor ~40 between extrema), as transport, more effective on light species, tends to homogenize the densities. Carbon dioxide reaches its maximum densities in the polar regions where temperatures are warmer (orange-red areas in Figure 4.2). Similarly, minima are reached at low latitudes on the nightside near the morning terminator where temperatures are colder (dark blue areas in Figure 4.2). The variations in the local temperature (factor ~2 between extrema, according to Figure 4.1) affect the scale heights of the constituents in proportion. They vary from 15 to 35 km and from 6 to 14 km for O and CO_2, respectively. The mean altitude of the Martian dayside homopause at equinox for solar low conditions (EL case) is evaluated to be at about 120 km [*Stewart* 1987; *Bougher et al.* 2000]. The day and

night atmosphere density profiles of both constituents were presented and discussed in *Valeille et al.* [2009b], in good agreement with the only *in situ* measurements available, by the Viking Lander 1 [*Hanson et al.* 1977; *Nier et al.* 1977].

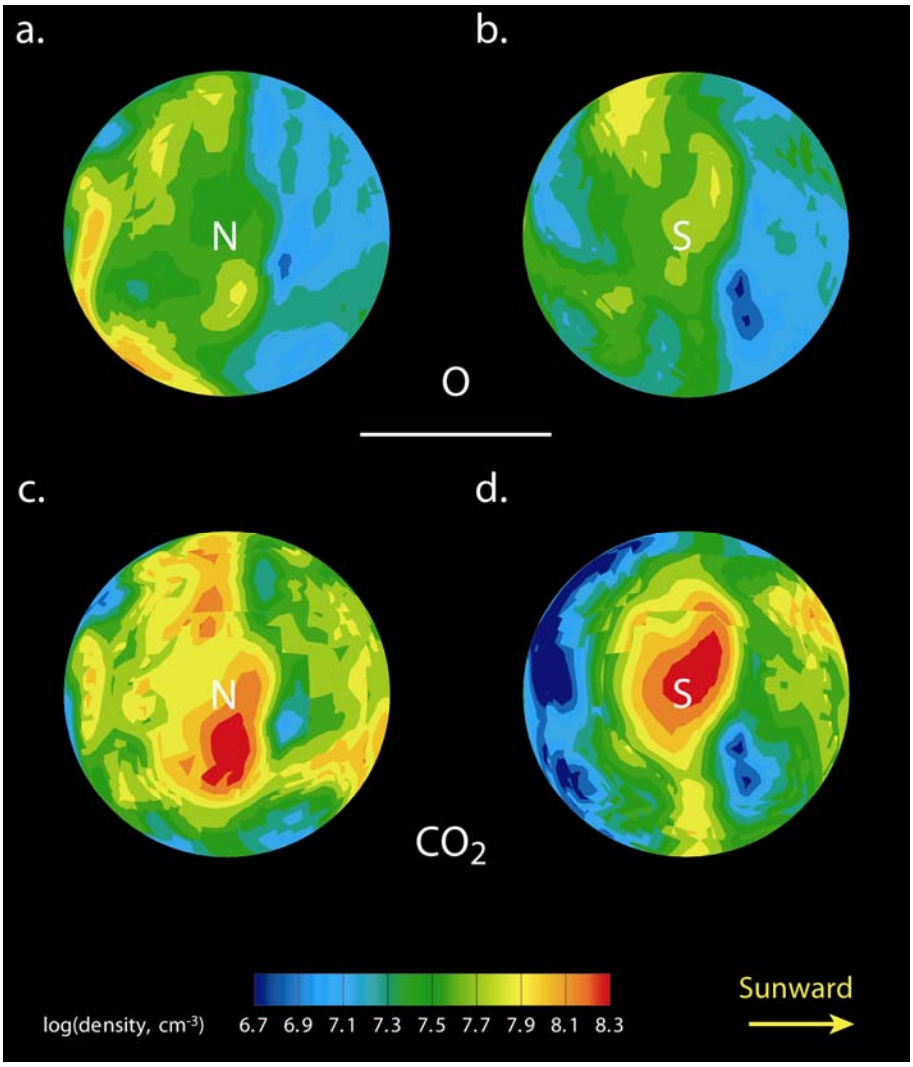

Figure 4.2. O density maps at the North (a) and South (b) hemispheres; CO_2 density maps at the North (c) and South (d) hemispheres at an altitude of 190 km. The same color scale is used for each figure. The North and South Pole positions are indicated by their initials N and S, respectively. The yellow arrow points toward the Sun.

IV.1.3. O_2^+ density distribution and ion peak

O_2^+ is the main ion of the Martian ionosphere. The O_2^+ DR is by far the most important source mechanism for the determination of the hot corona, therefore the O_2^+ ionospheric density profile is a critical parameter for the exospheric simulation. Its production occurs on the dayside and is directly related to the local background densities of CO_2 and O, the main parent in the photodissociation and charge exchange reactions,

$$\begin{cases} CO_2 + h\nu \rightarrow CO_2^+ + e \\ CO_2^+ + O \rightarrow O_2^+ + CO \end{cases} \quad (4.1)$$

A secondary source of O_2^+ ions is also considered by the MTGCM, via the photodissociation and charge exchange reactions,

$$\begin{cases} O + h\nu \rightarrow O^+ + e \\ O^+ + CO_2 \rightarrow O_2^+ + CO \end{cases} \quad (4.2)$$

O_2^+ reaches its maximum density at the same position as CO_2, *i.e.* in the polar regions, as shown at an altitude of 190 km in Figure 4.3a and in Figures 4.2c and 4.2d for O_2^+ and CO_2, respectively. On the dayside, the difference in O_2^+ density can be as high as of a factor of about 6 and the scale height varies from 8 to 19 km.

The ionospheric peak is found deep in the thermosphere at an altitude of ~122 km at the subsolar point (see O_2^+ density map at 120 km altitude in Figure 4.3b). On the dayside, its height is expected to rise with increasing SZA, as a result of the integration over a longer atmospheric slant path. Its magnitude is expected to decrease with increasing SZA, due to the geometry of the problem and to the extinction of ionizing solar radiation. Along the Equator, the ion peak height increases from ~122 to ~126, and then to ~134 km at 0°, 60° and 75° longitude, respectively. The magnitude of the electron concentration is ~1.8 x 10^5 cm^{-3} at the subsolar point (can be compared to the O_2^+ concentration presented in the work of *Valeille et al.* [2009b]) and decreases by a factor ~0.6 and ~0.4 from 0° to 60° and 0° to 75° longitude, respectively. These results are in general agreement with both theory and reported observations from Viking [*Zhang et al.* 1990], Mars Global Surveyor (MGS) [*Withers and Mendillo* 2005] and Mars Express (MEX) [*Morgan et al.* 2008].

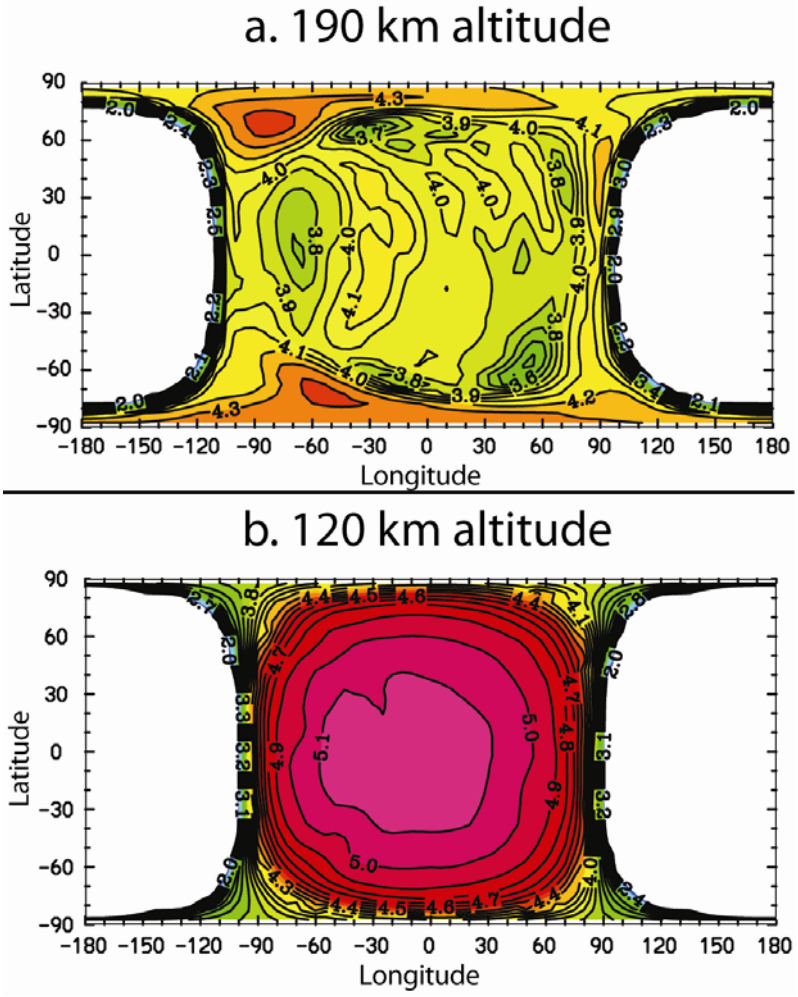

Figure 4.3. Surface map of O_2^+ ion log density (in cm^{-3}) at altitudes of 190 km (a) and 120 km (b). The same color scale is used for each figure. Maximum densities are shown in purple and correspond to ~1.0 x 10^5 cm^{-3}.

Figure 4.3a suggests an important spatial variation along SZA, but also from Equator to Pole. The MTGCM, along with other complex Martian thermospheric models capturing dynamical effects [*e.g. Angelats i Coll et al.* 2005], present similar enhancements for most of the macroscopic parameters. The increase towards the Poles may suggest that polar warming, observed in the Martian upper thermosphere during solstices in the winter hemisphere [*Bougher et al.* 2006], may be present at all seasons due to the dynamics. This shows that the use of 1D assumptions might be too simplistic for an accurate description of the sources of hot oxygen atoms in the Martian thermosphere.

Also, the results presented in this study suggest that because of higher concentrations of ions in the polar region compared to lower latitudes, the magnitude of the ion peak undergoes a milder decrease with SZA along a meridian than along the Equator. For the same reason, a sharper increase of the ion peak height is expected along a meridian. This latter result agrees with the concerns developed from the MARSIS observations on MEX [*Morgan et al.* 2008] and suggests that the Martian ionosphere presents asymmetries that need to be treated locally (rather than being a homogeneous Chapman layer).

It should be noted that reduced nightside O_2^+ is likely produced and modulated by electron precipitation [*Fillingim et al.* 2007], but is not a significant source of hot atomic oxygen.

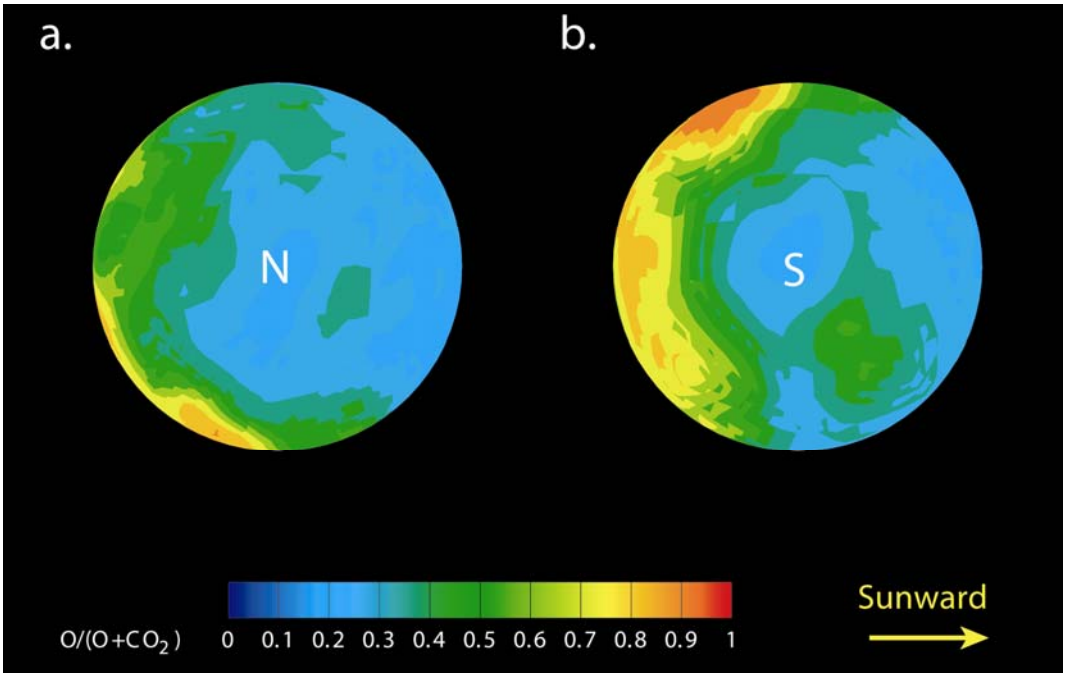

Figure 4.4. Maps of the oxygen mixing ratio, $X_O = O/(O+CO_2)$, at the North (a) and South (b) hemispheres at an altitude of 190 km, above which O becomes the main neutral constituent of the Martian upper thermosphere on the average. The same color scale is used for each figure and is consistent with Figure 4.5. The North and South Pole positions are indicated by their initials N and S, respectively. The yellow arrow points toward the Sun.

IV.1.4. Atom-to-molecule ratio ($r_{a/m}$)

The O to CO_2 ratio, sometimes called atom-to-molecule ratio (noted $r_{a/m}$), is a particularly important parameter of the Martian upper atmosphere, as it affects locally the exobase height, the ion production, the plasma heating, as well as the escape loss due to incident pickup ions [*Leblanc and Johnson* 2002].

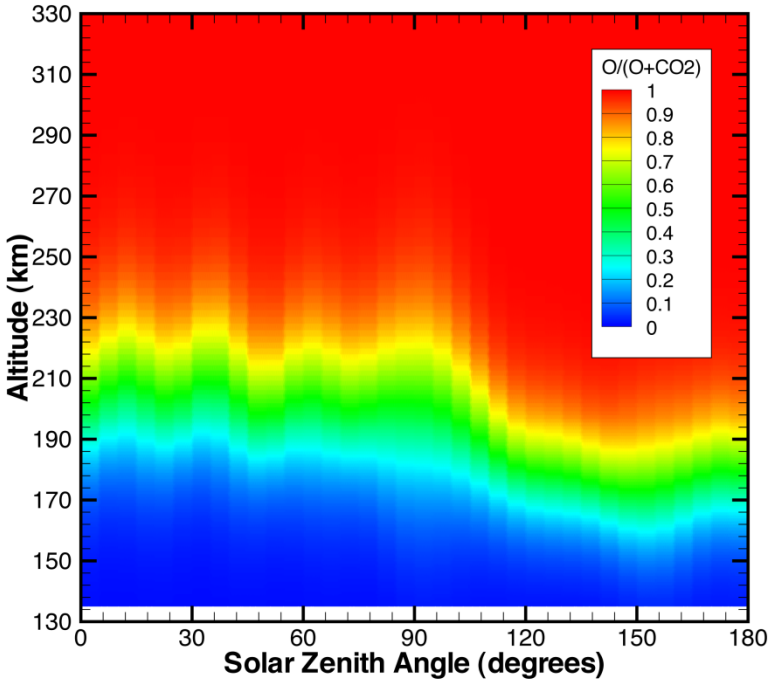

Figure 4.5. Oxygen mixing ratio, X_O = O/(O+CO_2), along a study path at the Equator from noon (0° SZA) to midnight (180° SZA) through dusk in the region where the transition occurs (130-330 km altitudes). The color scale is consistent with Figure 4.4.

The work of *Valeille et al.* [2009b] already noticed that the level, above which O becomes the main neutral thermospheric constituent, undergoes important variations with SZA along the Equator. This study shows that this level may vary from an altitude as low as 150 km to an altitude as high as 230 km locally around the planet. The averaged level is at an altitude of about 190 km. Figure 4.4 shows the O mixing ratio, X_O, a direct function of $r_{a/m}$, at that altitude,

$$X_O = r_{a/m}/(1 + r_{a/m}) \quad (4.3)$$

It shows that at that altitude, often assumed as the 'traditional' exobase height by previous studies [*e.g. Schunk and Nagy* 2009], neither O nor CO_2 can be rigorously

considered as the dominant specie. Indeed from Figure 4.4, X_O varies from less than 0.1 at the polar regions and at low latitudes north (blue areas in Figure 4.4) to more than 0.9 at low latitudes south (orange areas in Figure 4.4). A profile view of the oxygen mixing ratio is shown in Figure 4.5 along a study path at the Equator from noon (0° SZA) to midnight (180° SZA) through dusk in the region where the transition occurs (130-330 km altitudes). These important spatial variations in the X_O ratio are explained by the disparities in O and CO_2 abundances, varying both significantly and for different reasons (see Section IV.1.2). As discussed in Section IV.1.3, the ion production is expected to be higher at places where CO_2 is dominant locally. The plasma heating would also be higher, whereas the sputtering yield and the escape loss due to incident pickup ions should decrease due to a lower atom-to-molecule ratio [*Leblanc and Johnson* 2002].

IV.1.5. Exobase determination

A traditional definition of the exobase for a 1D problem is, for a single constituent (with a cross section σ) atmosphere [*e.g. Schunk and Nagy* 2009],

$$\int_{r_c}^{\infty} \sigma n(r)\, dr = \sigma n(r_c) H(r_c) = \frac{H(r_c)}{\lambda(r_c)} = 1 \qquad (4.4)$$

This is the level where the collision mean free path equals the temperature scale height of the constituent. However and as illustrated above, Mars upper atmosphere presents two major neutral constituents, and their mixing ratio varies greatly both with altitude and with position on the planet. Therefore, definition (4.2) should be modified for a more rigorous determination.

The definition of the local (*i.e.* for a given angular position) exobase level proposed in this thesis is: the level, above which an escaping particle moving straight up (along a radial direction away from the center of the planet) will encounter one collision on average. This is a more general definition; it is in agreement with the previous definition (4.3) for a 1D single constituent problem, and can also be used for a 3D multi-constituent problem. It should be noted that this is a conservative estimate of the exobase height, as in 3D, particles below that level are close to an isotropic distribution and therefore are more likely to collide than a purely radially moving particle. The criterion, e(**r**), a

function of the position, **r**, is defined as follows, and equals to 1 at the local position of the exobase, r_c (*i.e.* when $r = r_c$),

$$e(r_c) = \sigma_{CO_2} n_{CO_2}(r_c) H_{CO_2}(r_c) + \sigma_O n_O(r_c) H_O(r_c) = 1 \quad (4.5)$$

It is defined locally and depends on the density of the bulk atmosphere, the mixing ratio of O/CO_2 and the temperature. So, on Figure 4.6, the local exobase corresponds to the given altitude of 170 km in green areas, is below it in blue areas, and above it in red areas.

Interestingly, in the transitional domain, gravity and temperature stay roughly the same, and the altitude r_p where the probability of collision is p can be written,

$$p = \int_{r_c}^{r_p} n(r)\sigma \, dr = n(r_c)\sigma H(r_c)\left(1 - e^{\frac{r_c - r_p}{H(r_c)}}\right) = \left(1 - e^{\frac{r_c - r_p}{H(r_c)}}\right) \quad (4.6)$$

$$r_p = r_c - H(r_c)\ln(1 - p) \quad (4.7)$$

This result (taking $\sigma = 2 \times 10^{-19}$ m^2) shows that more than 90% of the collisions will occur within ~50 km above the exobase defined as above.

However for high dimension (*i.e.* 2D and 3D), the average vertical speed v_r for an isotropic distribution of speed v is,

$$< v_r >= \frac{\int v_{\parallel} f(\theta) d\theta}{\int f(\theta) d\theta} = \frac{\int v f(\theta) sin\theta d\theta}{\int f(\theta) d\theta} = \frac{v}{2} \quad (4.8)$$

with,

$$f(\theta) = cos\theta \quad (4.9)$$

This means that the particle goes in reality twice the 1D path. The above result means that particles collide on average once between r_c and $r_{0.5}$.

The exobase height follows roughly the temperature variations and reaches its lowest value of 155 km along the dayside terminator and at nightside low-mid latitudes, whereas its highest value of 195 km can be found in the polar regions. An average altitude of about 170 km can be found graphically (where most of the surface is found within a small range of the criterion). A 2D axisymmetric study of the exobase height along the Equator, as done in *Valeille et al.* [2009b], may then slightly underestimate the altitude of this level.

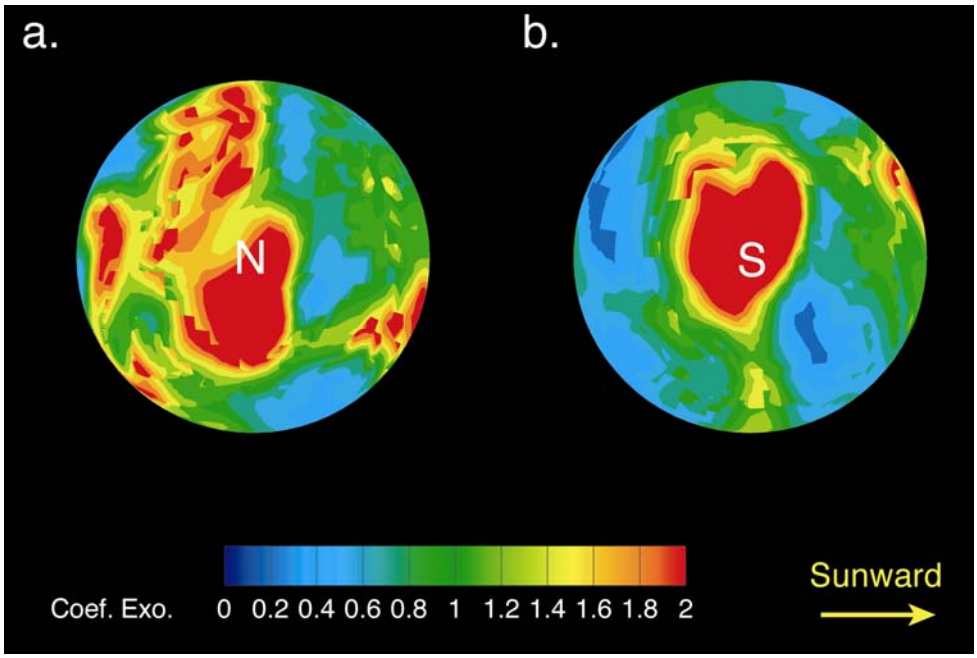

Figure 4.6. Maps of the exobase criterion at the North (a) and South (b) hemispheres at an altitude of 170 km. The same color scale is used for each figure. The North and South Pole positions are indicated by their initials N and S, respectively. The yellow arrow points toward the Sun.

IV.2. Exosphere

The 3D MTGCM calculations provide the respective thermospheric/ionospheric inputs for the 3D DSMC model, which in turn gives a detailed description of the Martian hot corona. In this section, the atmospheric loss due to O_2^+ DR is calculated, as is the ion production above the ionopause, which provides a generous upper limit for ion escape. As already mentioned and for comparison sake (with Viking measurements and with others models), all calculations are run at the fixed orbital position of equinox and for low solar conditions (EL case). These specific conditions have been systematically used in the past by modelers and serve as an example to illustrate the general structure and attributes of a 3D exosphere produced by a self-consistent 3D thermosphere/ionosphere model. Altitude profiles presented in this section come from 2D axisymmetric simulations for better resolution of the thermospheric region.

IV.2.1. Impacts of local thermospheric/ionospheric asymmetries

The principal advantages that a 3D study present compared to 2D include the influences of the thermosphere winds, the planetary rotation and the local features of thermosphere/ionosphere input parameters in general. Most suprathermal oxygen atoms, which define the Martian hot corona, are produced deep in the thermosphere and interact with it by collision. Therefore, the exospheric population is greatly affected by the distribution of the thermosphere/ionosphere parameters. In Section IV.1, the thermosphere/ionosphere is shown to exhibit diurnal patterns (such as dynamical effects and abrupt changes in the ionosphere structure), as well as local non-axisymmetric variations (temperature and wind distributions, planet rotation, polar warming, hemispheric asymmetries). It is natural to expect the exosphere to exhibit similar features.

Asymmetries in thermal and density structure of both the thermosphere (Figures 4.1, 4.2 and 4.4) and ionosphere (Figure 4.3) are responsible for local variations in the production (see Equation 3.1) and collision processes (see Equations 4.4 to 4.7), affecting more significantly the exospheric distribution closer to the exobase.

As mentioned in Section IV.1.1, the planetary rotation Equatorial speed is comparable to the average thermospheric wind speed in the Martian upper thermosphere. The impact of both parameters on a hot oxygen particle position depends on the time the particle spends in the system. The more time the particle spends in the system, the farther it is shifted away from its original 'wind-less' direction. Consequently, these impacts on the ballistic trajectories are more noticeable farther from the exobase and affect the general shape of the entire hot corona. An additional horizontal component of 240 m s^{-1} in the initial speed could result in a significant shift (corresponding to 20° SZA) in the position of a non-escaping particle at a distance of 3 Martian radii from the center of the planet. Therefore, thermospheric winds and planetary rotation exhibit comparable and sizeable impacts on the density profiles and consequently, on the ionization rates and even more on the return flux of particles to the thermosphere.

As far as we know, only one study [*Hodges*, 2000] considered the effects that thermospheric winds could have on the exospheric distribution of velocities by assuming simple diurnal tides (although Figure 4.1 above would suggest a different assumption). Hodges concluded that the velocity distribution would be affected by a slight shift with

respect to the escape speed. The study of *Chaufray et al.* [2007], which considers exclusively planetary rotation, reports an understandable difference between morning and evening terminator density profiles. However, since thermospheric winds and planetary rotation present important similar effects, they need to be addressed together. They are both non-axisymmetric parameters and therefore cannot inherently be produced by 2D simulations.

IV.2.2. Exobase fluxes

As shown in Figure 4.7, the net flux at the exobase is positive on the dayside and negative on the nightside, meaning that thermospheric hot oxygen atoms populate the exosphere from the dayside and some return into the thermosphere at night, yielding a cooling and heating effect from the exosphere, respectively.

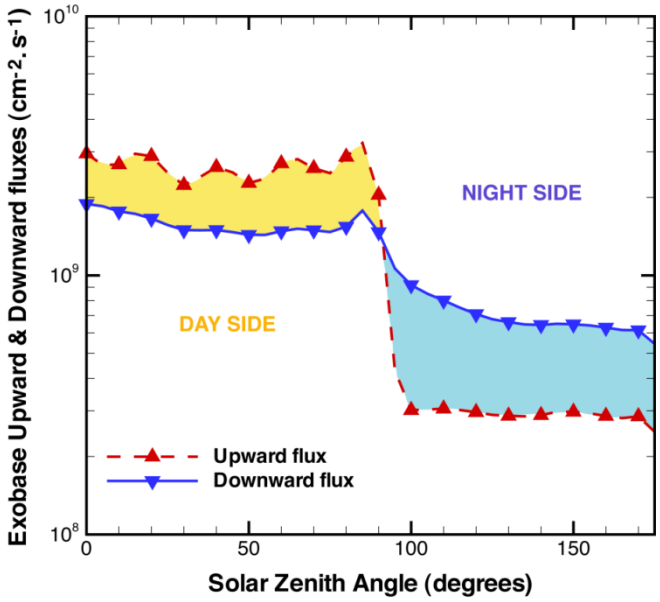

Figure 4.7. Upward (red arrows up) and Downward (blue arrows down) hemispheric fluxes of hot oxygen atoms as functions of SZA for Equinox, Low solar activity, Equatorial east (ELE) conditions in the vicinity of the exobase (190 km altitude). The net upward flux is positive (orange-shaded area) on the dayside and negative (light blue-shaded area) on the nightside. The other conditions: orbital positions (Aphelion, Equinox and Perihelion), solar activity (High and Low) and geographical positions (Polar meridian and Equator) present similar trends. These are 2D axisymmetric results.

The upward flux presents wavy patterns on the dayside, which result from the irregularities of the thermosphere and lower ionosphere underneath. As previously noted (Figure 4.3), the absence of ion production on the nightside produces a sharp drop around dusk (of a factor 10 approximately). But interestingly, despite this absence of production, the upward flux is non negligible (approximately half the downward flux) and nearly constant on the nightside. This will be explained later as a bouncing effect.

Due to its vast extent and collisionless flow regime, the exosphere tends to make the downward flux more uniform, returning flow of non-escaping particles back into the thermosphere, and lessening its amplitude drop at dawn compared to the upward flux.

IV.2.3. Bouncing

Considering the absence of hot oxygen production on the nightside (Figure 3.9), the existence of an upward flux at the exobase on the nightside in Figure 4.7 is of some theoretical interest. Making the distinction between the particles crossing the exobase downward leads to the observation that an important part of them are bouncing back into the exosphere after collisions with the thick atmosphere.

To understand this effect, it is important to keep in mind that among all particles produced in the transitional domain only a small fraction can rise through the collisions to the exosphere. In the same way, it is very hard to descend deep in the thermosphere when the exospheric particles could not escape and come back ballistically to the exobase. For returning particles, the mean free path undergoes a critical reduction in the vicinity of the exobase. And because they are incident from all directions on the nightside, half of them (the upward component of the post collisional distribution) will bounce back upward to the exosphere after the first collision, losing some energy in the process, another half after the second, and so on until their speed falls below $V_{threshold}$.

This bouncing effect would not have been apparent in the previous models [*Lammer et al.* 2000; *Kim et al.* 2001; *Kaneda et al.* 2007] that separated calculations for the thermosphere and exosphere, or more recent studies, which did not have sufficient cell size adaptation to follow a two orders of magnitude reduction in the mean free path

below the exobase (from approximately 200 km to 2 km, from 200 km to 135 km altitude respectively).

If the bouncing changes significantly the hot particles fluxes and populations in the vicinity of the exobase and can lead to night-to-day trajectories, it will also have an effect on the atmospheric loss. Indeed, production above the exobase should be taken into account, as first suggested by *Hodges* [2000]. He stated that the direct escape/exospheric source ratio should be "less [due to exospheric collisions] than 32%, which is the upward going half of the superescape branches of reaction (1)". However, particles generated in the downward direction above the exobase can also participate in the escape after bouncing back upward to the exosphere with a post-collisional speed above escape, and *Hodges* [private communication 2008] reports that this effect was taken into account in *Hodges* [2000].

IV.2.4. Escape flux

IV.2.4.1. Escape flux in 2D

As mentioned previously in this thesis, the first sets of calculations for the Mars hot corona were done using a 2D-axisymmetric version of the DSMC code and so cuts of 2D thermospheric conditions had to be extracted from the MTGCM as a function of SZA. Because they seemed to present the most different thermospheric/ionospheric features, Equatorial longitude and polar latitude dependent cuts were suggested as essentially the two extreme spatial dimensions of the Martian upper atmosphere environment [*Valeille et al.* 2009a]. With these assumptions, any 2D cut on the 3D spherical simulation should produce results that fall between the two curves on Figure 4.8. So the range between the two extremes 2D cuts could be used to define the range resulting from our 2D assumptions (compared to 3D). This approach has the benefit of setting reasonable lower and upper limits for the escape rate as a function of location.

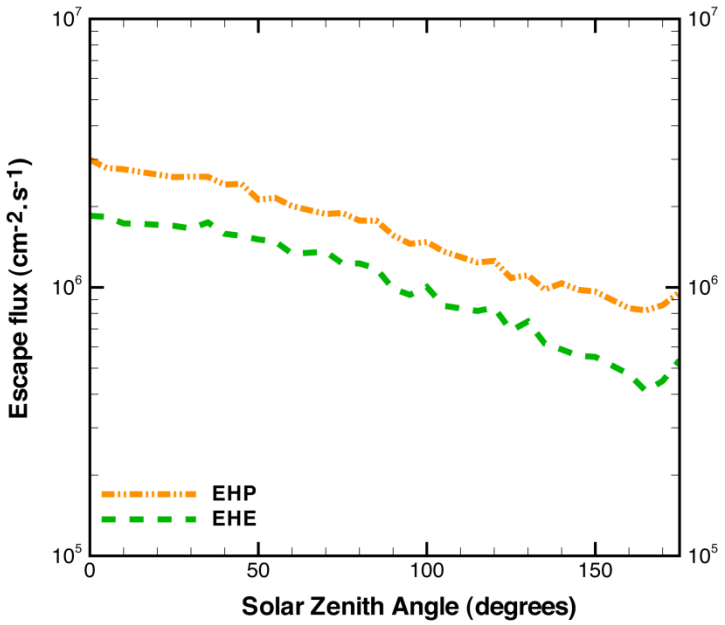

Figure 4.8. Escape fluxes of hot oxygen atoms as functions of SZA for Equinox, High solar activity along the south Polar cut (EHP, orange dashed-dotted-dotted line) and the east Equatorial (EHE, dashed green line) at 10 Martian radii.

A small difference in amplitude of Equatorial and polar plots would mean that the exospheric macroscopic parameters profiles are homogeneous with respect to the location and that a two-dimensional cylindrical model is sufficient to describe the entire Martian exosphere. A large difference, on the other hand, would mean that the use of a higher dimensional model would be more appropriate to account for spatial variations of those parameters. Although the two curves in Figure 4.8 show similarity (a decrease of a factor of about three going from noon to midnight, *i.e.* from 0 to 180° SZA), calculations along the polar cut might result in significantly higher local escape fluxes (about 30% higher) compared to simulations along the Equator. It can be noticed that, compared with the result of the flux of hot species at the exobase (in Figure 4.7), the escaping flux at 10 radii (in Figure 4.8) shows less variation with SZA.

IV.2.4.2. Escape flux in 3D

The integration of the hot oxygen escape flux of our 3D simulation, φ_{3D}, sits between the two extreme spatial cuts, φ_{Equ} and φ_{Pol} (for Equatorial and polar cut, respectively), as defined and expected by the 2D study of *Valeille et al.* [2009a], providing a good validation of the computational approach and computer code of the current 3D model. Interestingly, the Equatorial weight X, that quantifies the respective influence of Equatorial and polar thermospheric features on the whole 3D escape, is found to be ~0.70, in agreement with a simple geometric model where only Equatorial and polar distributions are known on a sphere and weighted accordingly with the surface they cover.

$$\varphi_{3D} = X\varphi_{Equ} + (1 - X)\varphi_{Pol} \tag{4.10}$$

Figure 4.9 shows the results of three different sets of thermosphere/ionosphere inputs onto the escape fluxes of hot oxygen atoms at 3 Martian radii (*i.e.* at an altitude of ~7000 km).

The 2D axisymmetric inputs along the polar meridian (Figure 4.9a) and along the Equator (Figure 4.9c) were characterized as the two most extreme spatial features of the Martian thermosphere/ionosphere in the 2D study of *Valeille et al.* [2009a]. As expected, these 3D simulations of extrapolated 2D axisymmetric thermosphere inputs, similarly adopted by previous studies [*Hodges* 2000; *Chaufray et al.* 2007] give rather simple solutions. Escape fluxes are on average 30% higher for the simulation along the Pole, due mostly to the higher production of hot oxygen by O_2^+ DR in the polar region.

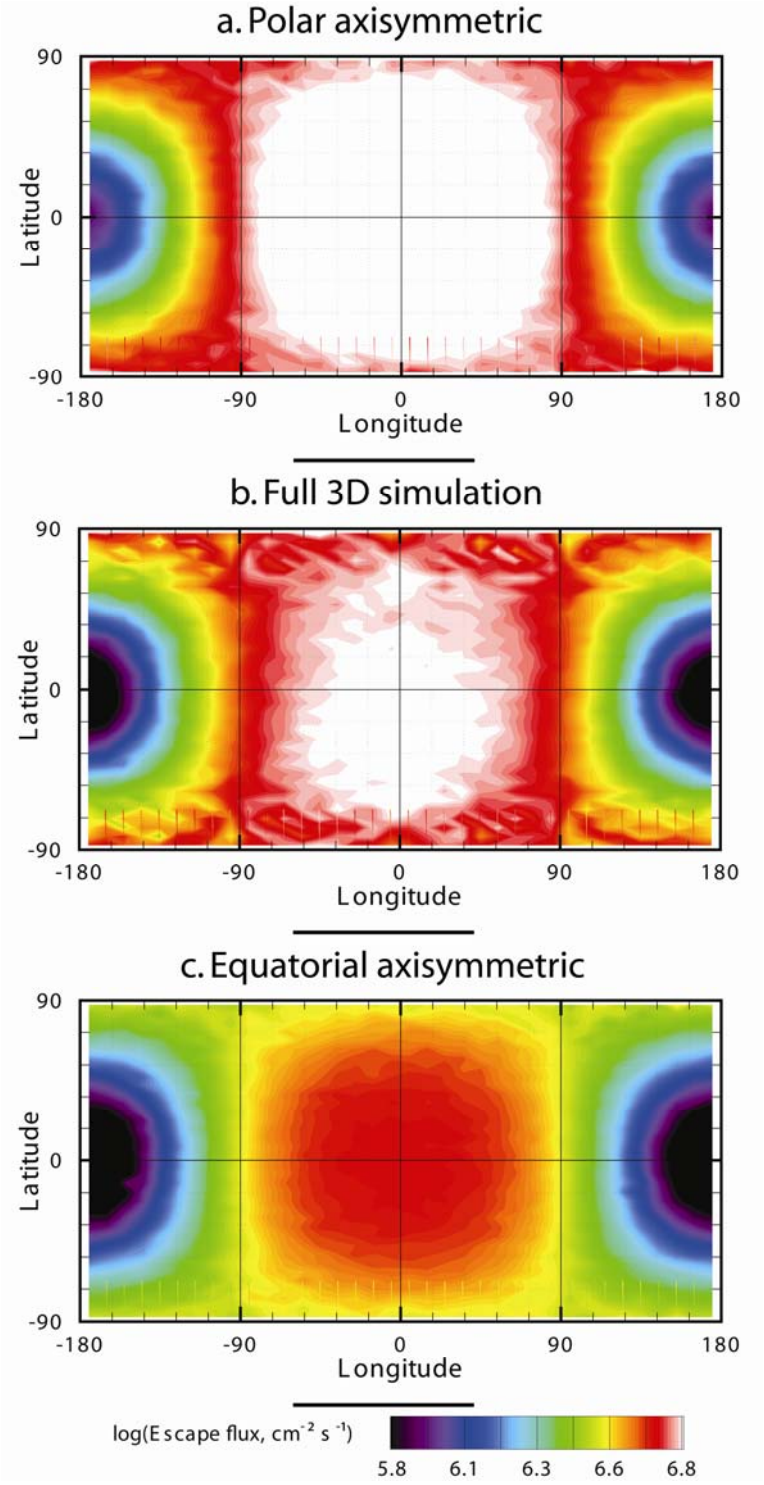

Figure 4.9. Flux of escaping hot oxygen atoms as functions of longitude and latitude at an altitude surface of 2 Martian radii (~7000 km) in the frame associated with the Sun. Results from 2D axisymmetric inputs along the polar meridian and along the Equator are presented in the top (a) and bottom figures (c), respectively; whereas the results from 3D inputs is shown in the middle figure (b). Thermospheric winds and planetary rotation are included in the full 3D calculation only.

As expected from the study of *Valeille et al.* [2009a], the results of the full 3D calculation stand between these two spatial extremes. The spatial integration of the flux leads to an estimated escape rate of 6.0 x 10^{25} s^{-1}. Rather than an axisymmetric circular shape, the escape flux of hot oxygen, as shown in Figure 4.9b, exhibits an oblong shape extended towards the Poles. Also, the atmospheric loss may be slightly larger in the south than it is in the north due to the hemispheric asymmetries, topographic differences and the dust distribution characterized in the lower atmosphere inputs.

Although there is no production on the nightside of the planet, a low escape flux (of about an order of magnitude smaller than on the dayside) is calculated at 3 radii in the vicinity of the antisolar point. In contrast, the study of *Valeille et al.* [2009a] reported a difference of only a factor 3-4 between the subsolar and the antisolar points at an altitude of 10 radii. This abrupt decrease in the diurnal variations of the escape flux with an increasing distance from the center of the planet is explained by the cumulative effect of collisions in the transitional domain, presence of nightside ions in the vicinity of the terminator, and more importantly trajectory curvature due to gravity.

The same calculations in the frame associated with Mars (*i.e.* without the effect of planetary rotation) would roughly yield a similar 3D picture shifted ~5-10° longitude towards the west. This is in excellent agreement with the theoretical exercise made in Chapter II, where an additional horizontal component of 240 m s^{-1} in the initial speed led to a shift of about 500 km (corresponding to 5-10 degree angle) in the position of an escaping particle at 3 Martian radii, affecting the escape flux accordingly. The same speed results in a shift of about 4000 km (corresponding to 10-25 degree angle) in the position of a non-escaping particle at 3 Martian radii. Therefore, thermospheric winds and planetary rotation exhibit comparable and sizeable impacts on the escape fluxes, the density profiles (and consequently the ionization rates) and even more on the return flux of particles to the thermosphere.

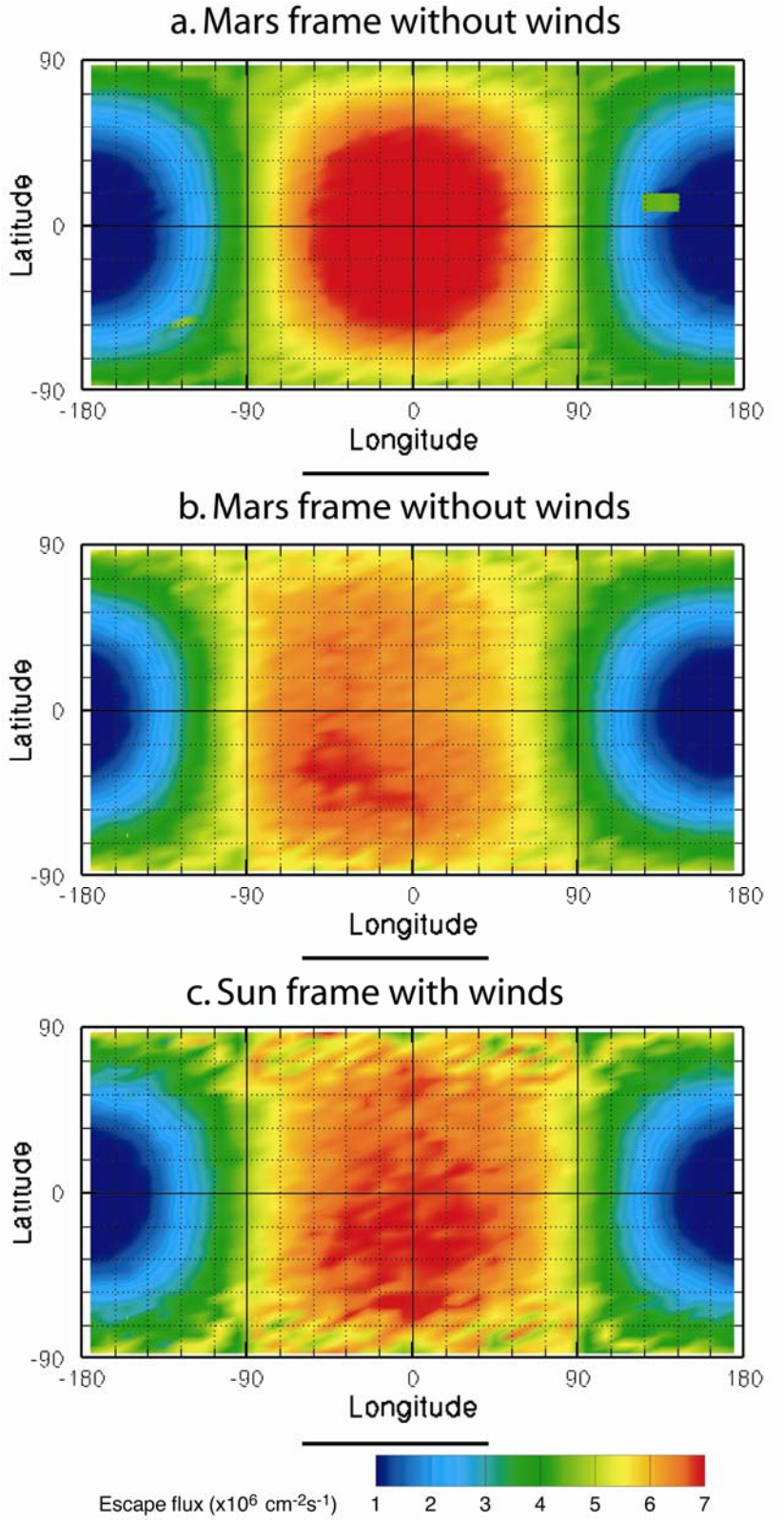

Figure 4.10. Flux of escaping hot oxygen atoms as functions of longitude and latitude at an altitude surface of 2 Martian radii (~7000 km) in the frame associated with Mars without winds (a) and with winds (b), and in the frame associated with the Sun (c).

IV.2.5. Hot corona

IV.2.5.1. Hot corona in 2D

Due to the DSMC method, the thermospheric inputs allow us to describe the gas system of the Martian exosphere and to provide a complete set of its macroscopic parameters. Figure 4.11 shows the spatial distribution of the hot oxygen density formed by O_2^+ DR in the Equatorial plane. Our model shows that if the density difference of hot oxygen atoms between noon and the terminator is of an order of magnitude near the exobase, it reduces abruptly with altitude due to lateral transport, confirming the result of the non-spherical study by *Kim et al.* [2001]. Although hot oxygen atoms are not produced from the nightside, they are transferred from the dayside very efficiently along ballistic trajectories.

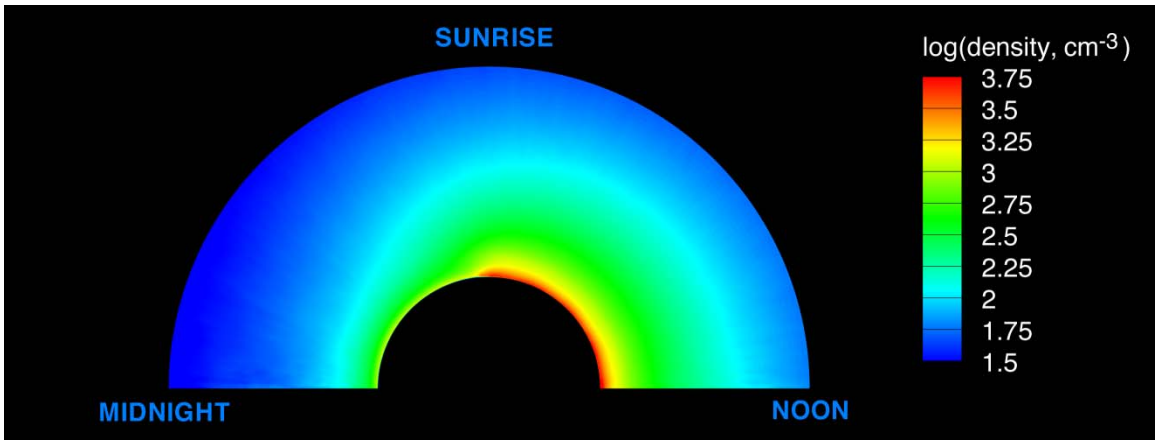

Figure 4.11. 2D plot of the hot oxygen density and temperature profiles for Equinox, Low solar activity, Equatorial (ELE) conditions versus SZA (from noon to midnight through dawn) and the altitude (from 135 to 7000 km).

Figure 4.12 shows oxygen density profiles in the altitude region where both hot and cold population profiles can be approximated linearly (in a semi-logarithmic plot). The transition between the cold and the hot regime in the oxygen density profile can be loosely defined as the range of altitudes where the cold/hot ratio goes from 0.01 to 100 respectively. This transition varies with SZA, solar activity and season, but is generally between 250 and 650 km. The total oxygen density can be considered cold below it and hot above, with approximately constant scale height temperatures in the 200-1000 km altitude region (for the case considered in Figure 4.12, ~170 K and ~4000 K for cold and

hot regime, respectively). The particles that are not followed in this simulation (the ones with speed that fall below $V_{threshold}$, *i.e.* twice the local thermal speed) have a noticeable contribution on the total density only up to about 400 km.

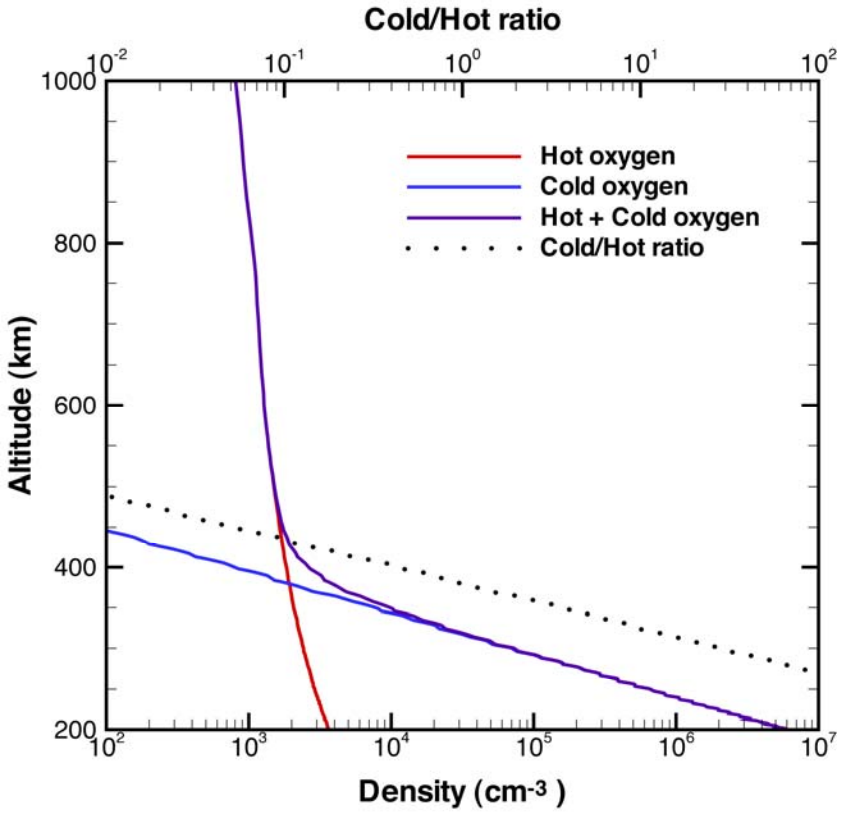

Figure 4.12. Total oxygen density profile (purple solid line) as function of altitude (from 200 to 1000 km) at 60° SZA for Equinox, Low solar activity, south Equatorial east (ELE) conditions. The cold (blue solid line) and hot (red solid line) oxygen population contribution can be clearly seen. The cold/hot ratio is also shown (dotted line).

IV.2.5.2. Hot corona in 3D

The resolution of the 3D unstructured mesh reveals the full density distribution of both cold and hot components (the criteria is defined in Chapter II) of the atomic oxygen population. The latter allows a description of the shape of the Martian hot corona to be made, as is shown in Figure 4.13 with three isodensity levels.

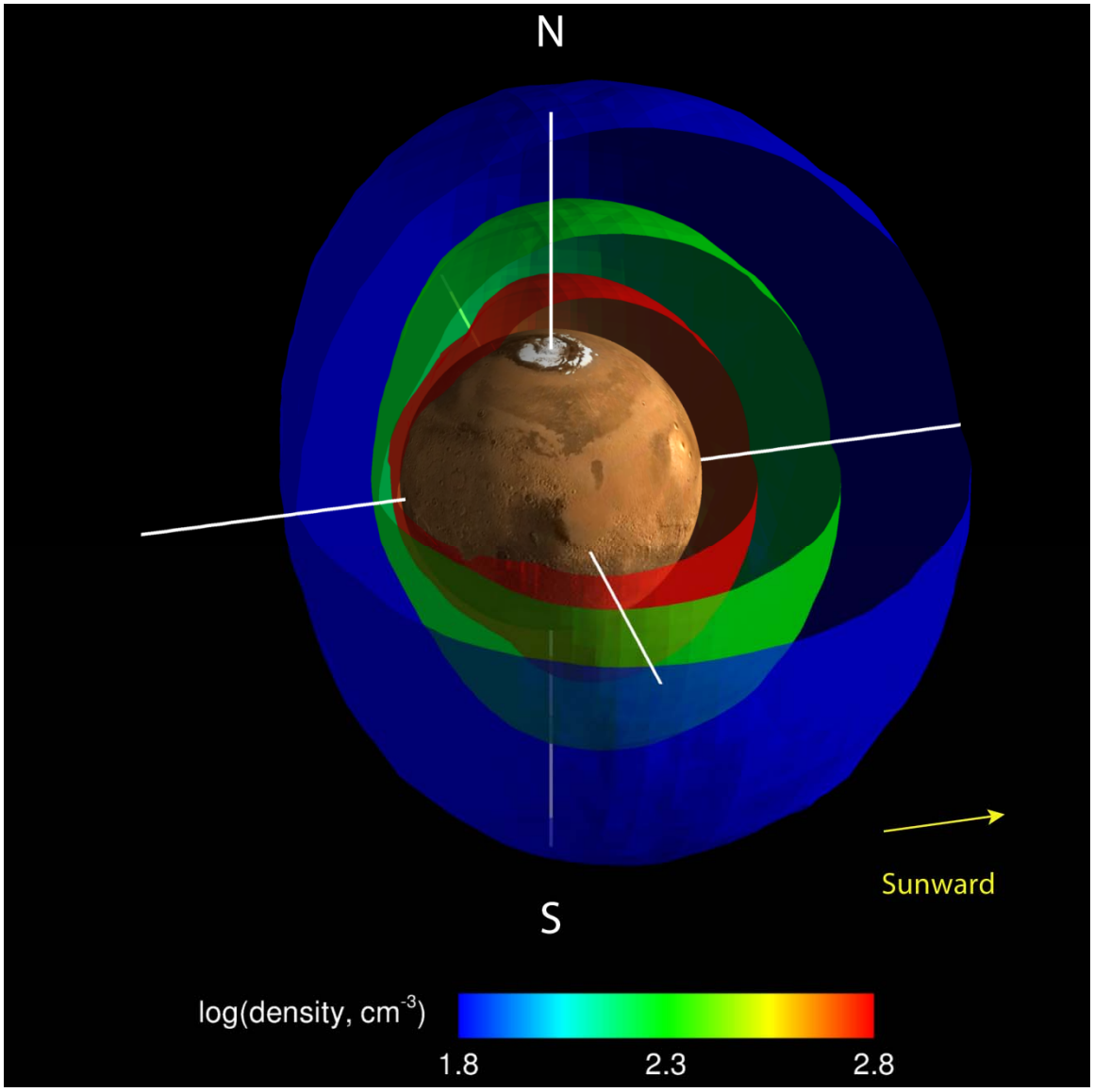

Figure 4.13. Three-dimensional representation of the Martian hot corona. Three isodensity surfaces of hot atomic oxygen are shown, decreasing with increasing distance from the planet: 600 cm^{-3} in red, 200 cm^{-3} in green, 60 cm^{-3} in blue. The North and South Pole positions are indicated by their initials N and S, respectively. The yellow arrow points toward the Sun.

In the vicinity of the exobase (170 km altitude) and below, the oxygen population is cold. Density profiles extracted along 1D columns at different positions around the planet exhibit a scale height temperature that matches the average neutral temperature of T_∞ ~170 K. Density maxima of ~2 x 10^8 cm^{-3} are found at low latitudes on the nightside, whereas minima of ~2 x 10^7 cm^{-3} are reached along the dayside terminator in the vicinity

of the exobase. Therefore, a factor of about 10 is observed in the spatial variation around the planet at this altitude.

In contrast, at higher altitudes (above ~600 km altitude), the oxygen population is hot and the scale height temperature is about T_{hot} ~4000 K. Maxima of ~60 cm^{-3} are located south of the subsolar point and minima of ~12 cm^{-3} are found in the vicinity of the antisolar point at an altitude of 7000 km. As a result, the shape of the hot corona is clearly inflated towards the dayside (Figure 4.13). However, the important diurnal density variation decreases with altitude (from a factor ~30 near the exobase to a factor ~5 at an altitude of 7000 km), due to a very efficient transfer along ballistic trajectories, in agreement with the results of previous studies [*Kim et al.* 2001; *Valeille et al.* 2009a]. Further above (7000 km to 10 radii), temperatures decrease due to expansion and a study over an extended domain [*Valeille et al.* 2009a] reports a scale height temperature of about ~4000 K and a diurnal density variation of a factor ~3.

The hot oxygen component should begin to dominate above the cold background atmosphere at an average altitude of about 500 km [*Lammer et al.* 2000; *Lichtenegger et al.* 2007; *Valeille et al.* 2009a] above the Martian surface for the conditions considered. As both exospheric and thermospheric oxygen profiles change spatially in a 3D description, this transition level varies between ~400 km (vicinity of the subsolar point) to ~600 km altitude. In this region, the cold-to-hot O ratio increases from 0.01 to 100 in less than 50 km. Consequently, the neutral temperatures are expected to exhibit a sharp transition between a cold and hot isothermal structure (from T_{∞} ~170 K to T_{hot} ~4000 K).

While a dramatic diurnal variation is seen in the escape fluxes close to the planet due to the absence of production on the nightside (Section IV.1.3), it is not the case in the density distribution, which is rather smooth by comparison. The main difference is that non-escaping energetic particles keep interacting with the thermosphere after they leave the exobase by bouncing. This mechanism is presented and discussed in the study of *Valeille et al.* [2009a] and contributes significantly to the population on the nightside.

IV.2.6. O^+ ion production

Figure 4.14 shows the simulated total ionization rate in the Martian extended ionosphere after summation of the three main ionization contributions. In this study, both relative contributions of cold and hot oxygen particles can be considered, and they are shown comparable for each ion production process (Table 4.1).

Table 4.1. Ionization of cold and hot atomic oxygen by the three main ionization contributions; PI, CE and EI

	PI	CE	EI	Total
hot O	8.9×10^{22}	6.2×10^{22}	4.7×10^{23}	7.2×10^{23}
cold O	1.8×10^{23}	1.2×10^{23}	1.2×10^{24}	1.5×10^{24}
hot + cold O	2.7×10^{23}	1.8×10^{23}	1.7×10^{24}	2.2×10^{24}

Integration gives a total O^+ ion production of 2.2×10^{24} s^{-1}, in good agreement with the recent study of *Chaufray et al.* [2007] (1.9×10^{24} s^{-1} for solar low activity). This latter study, together with the work of *Valeille et al.* [2009b] that reported a value of 1.5×10^{24} s^{-1}, used axisymmetric Equatorial inputs and therefore is likely to underestimate the total production, due to asymmetries in the atomic oxygen distribution. Under the generous assumption that all ions produced above the ionopause escape, the computed O^+ ion loss would then be in excellent agreement with the value of ~2.4×10^{24} s^{-1} based on data obtained with new energy settings for the ASPERA-3 ion mass analyser on MEX reported in the recent study of *Lundin et al.* [2008]. However, if only 10 to 35% of ions produced are considered to escape, as suggested by some studies [*Chaufray et al.* 2007; *Fang et al.* 2008], then the estimation of the O^+ ion loss should be scaled down by an order of magnitude. This value would be closer to the one of ~1.6×10^{23} s^{-1} derived from the measurements of the same instrument using original energy settings [*Barabash et al.* 2007]. It should be noticed that ionospheric outflow should be also included for a more rigorous description of the ion loss [*Ma and Nagy* 2007]. Even in its most generous estimation (of 2.2×10^{24} s^{-1}), the ion loss remains more than an order of magnitude less than the hot oxygen escape of 6.0×10^{25} s^{-1}.

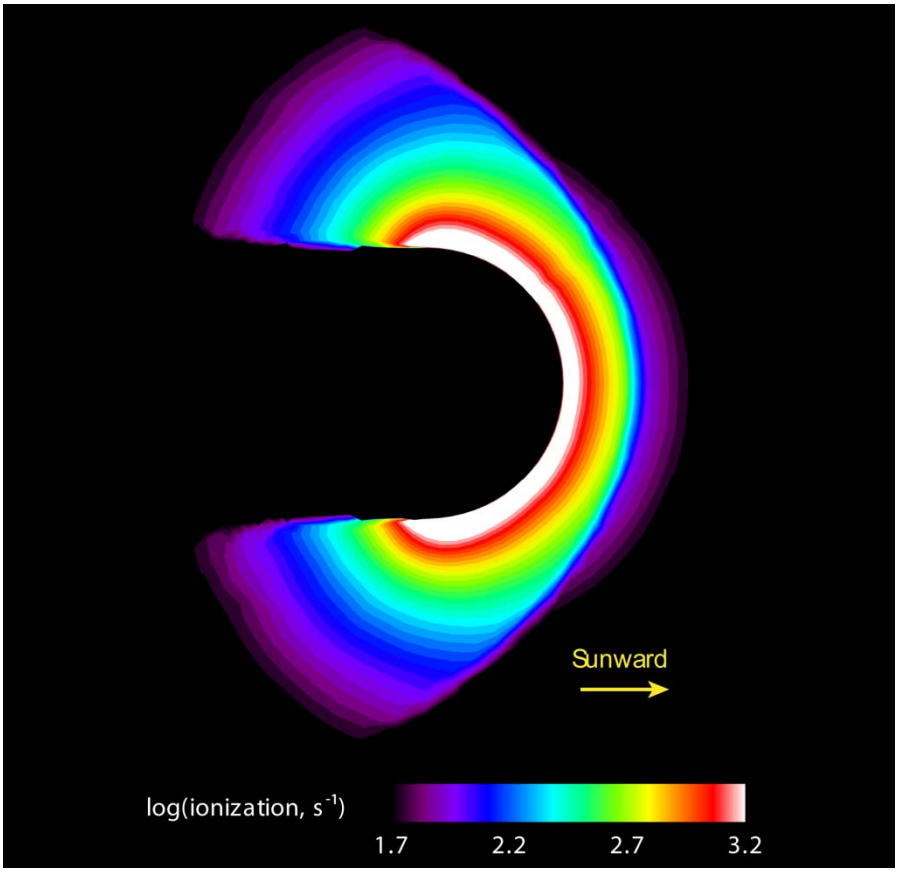

Figure 4.14. O^+ ionization rate (in s^{-1}) in the Equatorial section. The yellow arrow points toward the Sun.

Chapter V
Solar cycle and seasonal variations

While variations of the hot corona with solar activity have been previously studied by two- and three-dimensional models that use extrapolation of 1D thermospheric/ionospheric inputs [*Hodges* 2000; *Kim et al.* 2001; *Chaufray et al.* 2007], this global 3D study is the first to consider both solar cycle conditions, low and high, and seasonal variations, named for the remainder of this work after the corresponding orbital position of aphelion, equinox and perihelion (which constitute for the north hemisphere, summer, spring/autumn and winter, respectively).

Solar cycle influences are characterized at a fixed orbital position of equinox by comparing Equinox solar Low (EL) case with Equinox solar High (EH) case. Seasonal influences are characterized at a fixed low solar activity by comparing Aphelion solar Low (AL) case, with Equinox solar Low (EL) case and with Perihelion solar Low (PL) case. These notations are used in the remainder of the thesis. The combined effects of these long-term variations can be characterized by the two extreme net solar forcing cases of Aphelion solar Low (AL) and Perihelion solar High (PH). A similar approach is used in the studies of *Valeille et al.* [2009a, 2009d] along the Equator and the polar meridian.

In the case of study along a 2D axisymmetric path, the influence of the position of the planet is considered by comparing calculations made along the Equator with ones along the Polar meridian. E or P is then added to the notation to represent Equatorial or polar path, respectively.

V.1. Thermosphere/Ionosphere

V.1.1. Temperatures, heating and winds

In the cold isothermal region of the Martian atmosphere, *i.e.* in the upper thermosphere until approximately 600 km altitude [*Valeille et al.*, 2009a], the average neutral exospheric temperature, T_∞, is about 170-180 K for the EL case (Figure 5.1a). It is mostly located at low and mid latitudes on the dayside and high latitudes on the nightside. High temperatures are found on the dayside along the terminator, maxima of about 250-290 K being at the dayside polar regions and in the vicinity of the evening terminator. Minimum temperatures of about 115-130 K are situated south, at low-mid latitudes on the nightside.

The spatial distribution of temperature averages and extrema, and the temperature structure in general, stays the same from the EL to the EH case (Figures 5.1a and 5.1b). However, the increase in the EUV flux leads to higher dayside average and maximum temperatures of about +100-110 K. The dynamics, which effectively cools the dayside and heats the nightside, tends to homogenize the temperatures, and the nightside is then affected to a lesser extent (about +50 K) by the solar cycle variation (see Table 5.1a).

Due to Mars significant eccentricity, the change in the heliocentric distance with orbital position of the planet leads to a significant variation in the EUV flux at the top of the atmosphere [*e.g. Bougher et al.* 1999, 2000]. While the average temperature changes slightly from 160-170 K for the AL case to 180-190 K for the PL case, the axial tilt (of a maximum of ±25.19° during solstices) changes the spatial distribution dramatically. Polar regions are either at constant night or day, affecting the entire global temperature structure and the global dynamics. Minima are more pronounced (about -20 K) for solstices than for the equinox cases and are located on the nightside Equator between the antisolar point and the opposite hemisphere mid latitudes (dark blue areas in Figure 5.3b, light blue areas in Figure 5.3d). Maxima are on the dayside Equator between the subsolar point and the opposite hemisphere mid latitudes, as well as in the morning in the summer hemisphere (green areas in Figure 5.3b, orange areas in Figure 5.3d). They are also slightly lower than for the EL case (by about -20 K) since the dynamical cooling due to vertical winds is more efficient in these regions. Linear regression of average dayside temperatures, a function of the F10.7cm index scaled to Mars (between F10.7cm = 20

and 110, corresponding to the AL and PH cases, respectively) leads to a slope dT/dF10.7cm of about 1.45-1.68 (Figure 5.2), in good agreement with the reported observation of about 1.5 [*Forbes et al.* 2008].

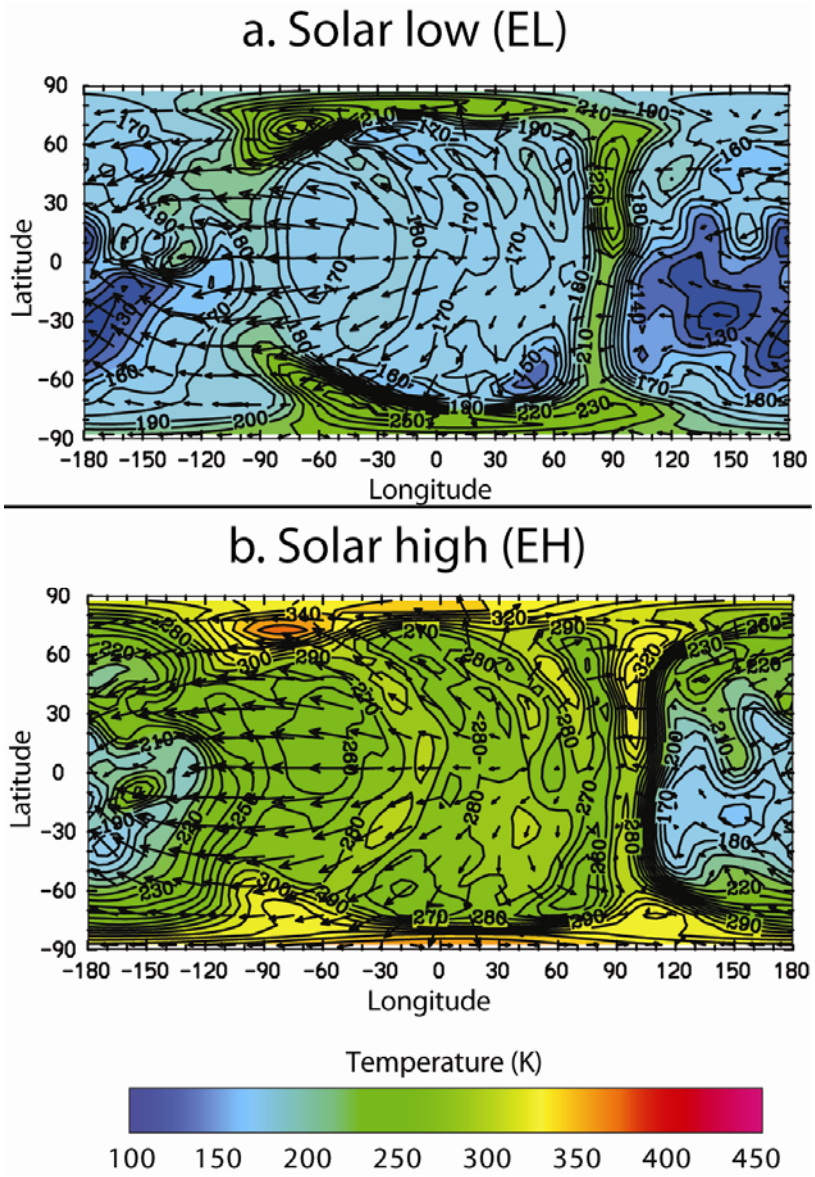

Figure 5.1. Neutral temperature in the vicinity of Mars exobase for low (a) and high (b) solar activity for modern conditions. The results are shown at the respective average exobase level, *i.e.* at an altitude of 170 km for the EL case (a) and of 185 km for the EH case (b). Horizontal wind velocities are represented in the frame associated with Mars by arrows with maxima at ~490 (a) and ~520 m s^{-1} (b). The same color scale is used for each panel and is consistent with that for Figure 5.3 [Source: *Bougher et al.* 2009b].

In the frame associated with Mars, the general circulation pattern in the vicinity of the exobase is essentially toward the west (opposed to the planetary rotation direction and with a comparable magnitude) with a minimum at the evening terminator and maximum (of about 490 m s^{-1}) at the morning terminator. Coriolis effects are noticeable at high latitudes (see Figures 5.3b and 5.3d). The trend stays the same with solar activity, with slightly stronger average winds for the EH case. In the solstice cases, the winds present more complex features than the equinox cases and are mostly oriented towards the winter Pole (see Figures 5.3b and 5.3d). The PL case exhibits stronger winds (maximum at 435 m s^{-1}) than the AL case (maximum at 390 m s^{-1}), as both solar heating and dust opacity are higher, further strengthening the wind system [*Bougher et al.* 2006].

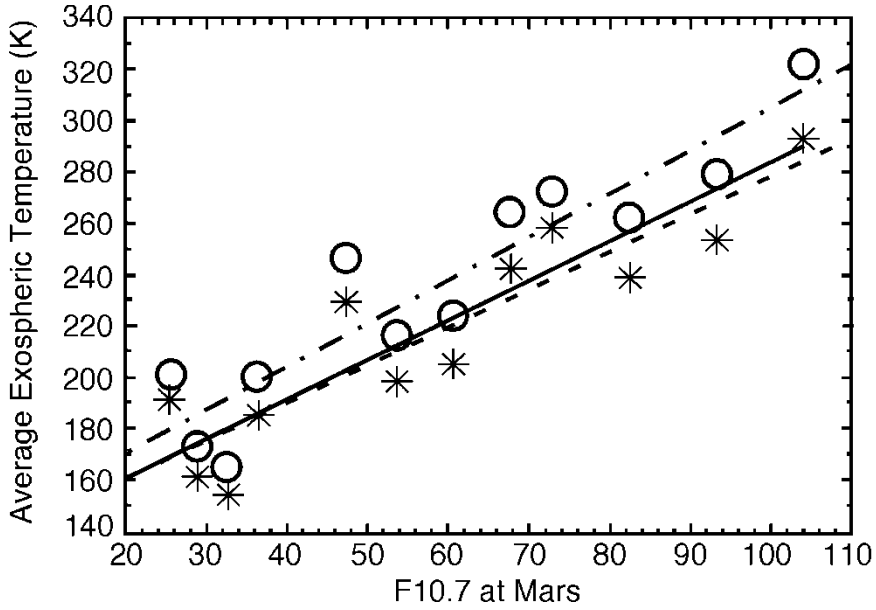

Figure 5.2. Average exospheric temperature function of the F10.7 cm index at Mars [Source: *Bougher et al.* 2009b].

According to *Bougher et al.* [1999, 2000, 2009a], the primary dayside balance for present day Mars occurs between EUV heating and molecular thermal conduction, with CO_2 cooling playing a tertiary role. In addition, Mars adiabatic cooling, due to rising motions on the dayside from the global circulation, should play a progressively more important role as the solar cycle advances. This "dynamical thermostat" cannot be ignored when examining the heat balances, giving rise to solar cycle and seasonal variations of Martian thermospheric neutral temperature. 3D models are thus essential

for a proper investigation of Martian thermospheric heat balances [*Bougher et al.* 2000, 2009a]. Furthermore, it is important to account for these effects as they relate to and produce a proper 3D corona.

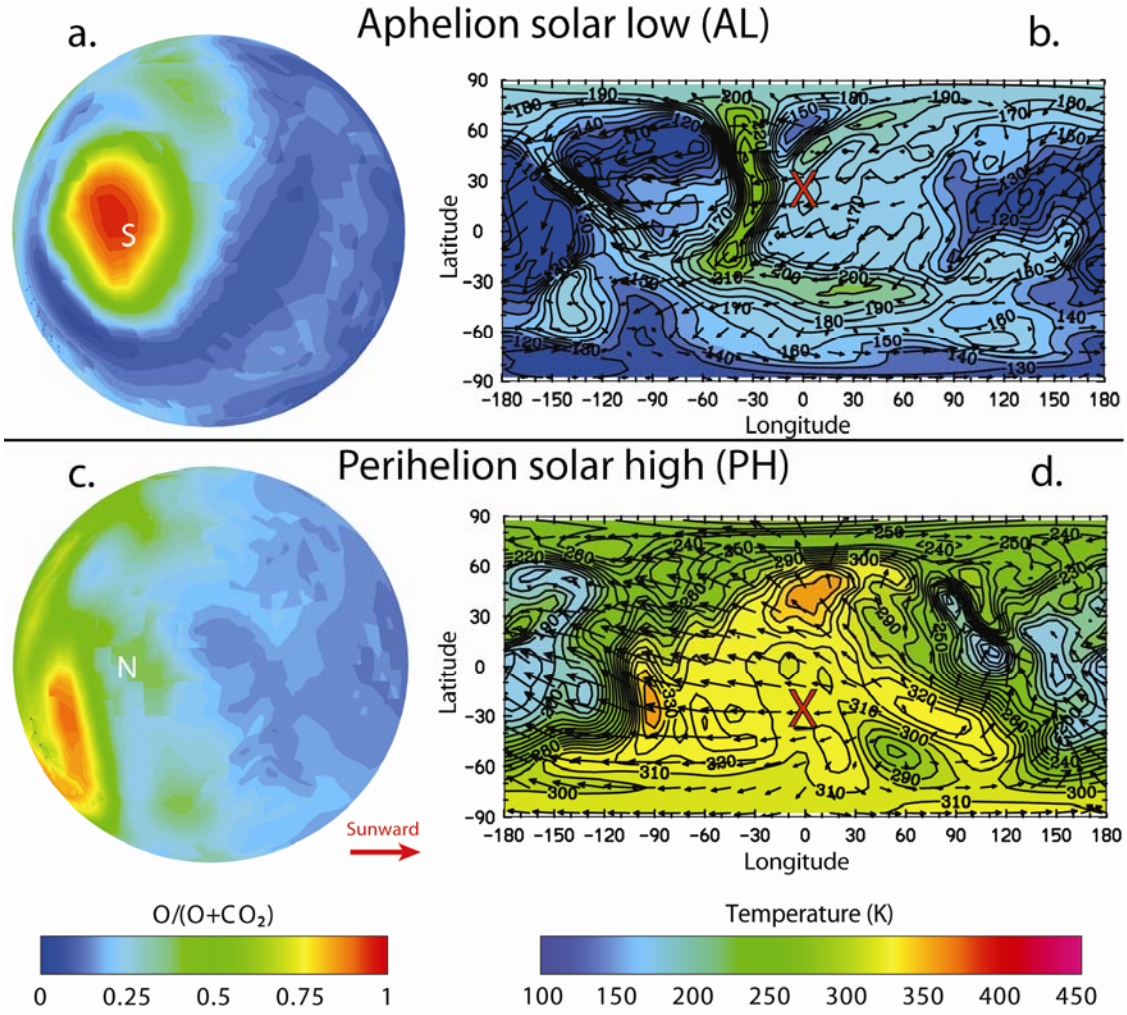

Figure 5.3. Oxygen mixing ratio in the winter hemisphere and neutral temperature in the vicinity of Mars exobase for the two most extreme cases for modern conditions. The results are shown at the respective average exobase level, *i.e.* at an altitude of 165 km for the AL case (a and b) and of 195 km for the PH case (c and d). Horizontal wind velocities are represented in the frame associated with Mars by arrows with maxima at ~390 (b) and ~555 m s^{-1} (d). The same color scale is used for each panel and is consistent with that for Figure 5.1. The red crosses mark the subsolar point. The North and South Pole positions are indicated by N and S, respectively. The red arrow points toward the Sun.

V.1.2. O and CO_2 density distribution

Mars upper atmosphere presents two major neutral constituents, carbon dioxide and atomic oxygen. For the EL case, atomic oxygen reaches its maximum densities at low latitudes on the nightside near the morning terminator where the winds are stronger and converge, whereas minima are reached on the dayside close to the evening terminator where winds are weaker and diverge (Figure 5.4a). Carbon dioxide reaches its maximum densities in the polar regions where temperatures are warmer. Similarly, minima are achieved at low latitudes on the nightside near the morning terminator where temperatures are colder.

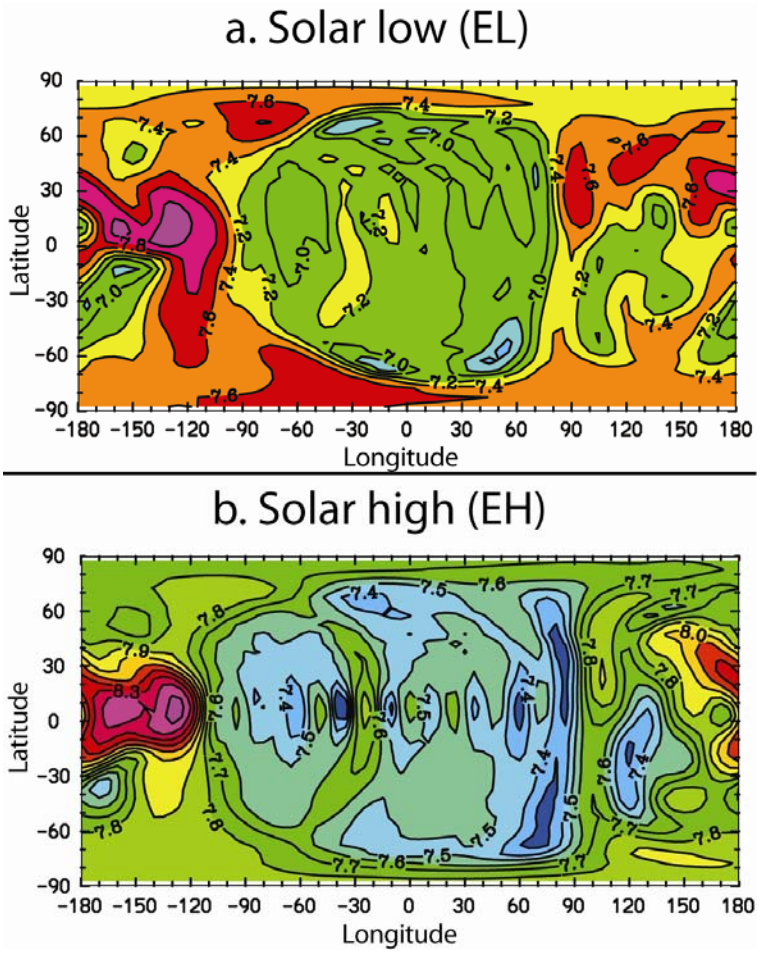

Figure 5.4. Atomic oxygen in the vicinity of Mars exobase for low (a) and high (b) solar activity for modern conditions. The results are shown at the respective average exobase level, *i.e.* at an altitude of 170 km for the EL case (a) and of 185 km for the EH case (b). The color scale used is different for each panel [Source: *Bougher et al.* 2009b].

For the EH case, density profiles extracted along 1D columns exhibit a scale height temperature that matches the average neutral temperature of T_∞ ~260 K. The spatial distribution is very similar to that in the upper atmosphere in the EL case (Figure 5.4b). At a given altitude, an enhancement in density of a factor of about x1.8-2.0 is computed due to solar activity (Table 5.1b). This increase in the background densities at a fixed altitude is due to higher thermospheric temperatures for solar high, that affect the scale heights of the constituents proportionally, resulting in a global expansion of the atmosphere.

It is logical to expect large variations with seasons in the spatial distributions of the background species. Indeed, O and CO_2 densities are driven locally by the respective effect of dynamics and temperature, which are shown to vary significantly (see Figure 5.3b and 5.3d). Atomic oxygen reaches its maximum densities at the winter Pole (*i.e.* south Pole for aphelion, and north Pole for perihelion), whereas carbon dioxide does so at the summer Pole (*vice versa*). Both species reach minima between the summer Pole and the antisolar point. An enhancement in density of a factor of about x1.7-1.8 is estimated, and the differences between extrema are more pronounced for the solstice cases (about x30 for O) compared to the equinox cases (about x10 for O).

As shown in Chapter IV, the O mixing ratio, $O/(O+CO_2)$, not only varies greatly with the altitude (due to different scale heights above the homopause and the CO_2 molecule being heavier than the O atom), but also with the angular position on the planet (due to local features of thermospheric temperature and dynamics). Indeed, CO_2 is more responsive to the background temperature, while O is more responsive to the winds. Figures 5.3a and 5.3c show maps of the oxygen mixing ratio for the two most extreme cases combining the effects of solar activity and seasons for modern conditions. It presents a clear illustration of additional implications of the winter polar warming effect [*Bougher et al.* 2006], exhibiting a peak in the atomic oxygen concentration in the winter polar region. These should be considered in context with Figures 5.3b and 5.3d, which present strong convergent winds and a vortex circulating towards the winter polar regions, where the only heating mechanism is dynamics (as opposed to the EUV heating on the dayside). This is in good agreement with the measurements by the ultraviolet spectrometer (SPICAM) instrument onboard Mars express (MEX) of the nitric oxide

night airglow [*Bertaux et al.* 2005]. Indeed, atomic oxygen and nitrogen, tracers of the circulation, were observed blowing from the dayside towards the winter Pole.

Table 5.1. Impact of season and solar cycle on thermospheric/ionospheric parameters (quantities and units are indicated in parenthesis)

a. Neutral temperature (min/ave/max, in K)

		Orbital position		
		Aphelion	Equinox	Perihelion
Solar activity	Low	90/165/260	115/175/290	100/185/260
	High		155/260/370	155/310/360

b. Global average O density at 165 km (x 10^7 cm^{-3})

		Orbital position		
		Aphelion	Equinox	Perihelion
Solar activity	Low	4.8	6.5	8.4
	High	8.9	13.0	15.0

c. Electron density at subsolar point (x 10^5 cm^{-3})

		Orbital position		
		Aphelion	Equinox	Perihelion
Solar activity	Low	1.8	2.0	2.1
	High	2.7	3.1	3.2

d. Ion peak height at subsolar point (km)

		Orbital position		
		Aphelion	Equinox	Perihelion
Solar activity	Low	116	122	128
	High	116	122	128

e. Average exobase height (km)

		Orbital position		
		Aphelion	Equinox	Perihelion
Solar activity	Low	165	170	180
	High		185	195

V.1.3. O_2^+ distribution and ionospheric peak

O_2^+ is the main ion of the Martian ionosphere and its distribution is closely related to both local solar radiation and density of the bulk atmosphere (O and CO_2 being its parents via photodissociation and charge exchange reactions). As a result, it is located

mostly on the dayside, and its abundance undergoes significant variations spatially and with solar cycle and seasons.

For the EL case (Chapter IV), the ionospheric peak is found to be deep in the thermosphere at an altitude of about ~122 km at the subsolar point (Figure 5.5c). Its magnitude, defined as the local electron density there, is estimated to be 2.0 x 10^5 cm^{-3}. Both height and magnitude are affected by solar radiation. The peak height is controlled by the underlying lower atmosphere, which is not greatly impacted by changing EUV-UV fluxes, but rather IR fluxes, while the peak magnitude and the region above it are more responsive to EUV radiation.

Solar activity is mostly characterized by variations in EUV radiation. So, while the altitude of the peak does not rise appreciably with the solar cycle, the magnitude of the ion peak, the electron density increases to 3.1 x 10^5 cm^{-3} at the subsolar point for the EH case (Figure 5.5d and Table 5.1c).

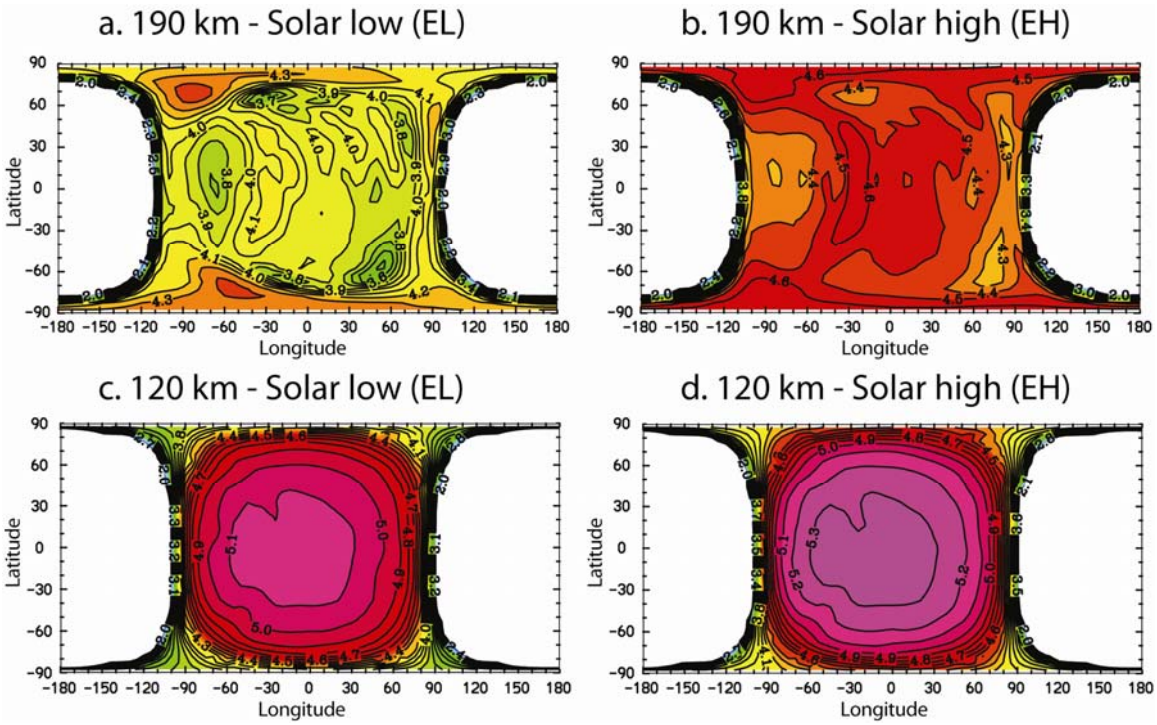

Figure 5.5. Surface map of O_2^+ ion log density (in cm^{-3}) at altitudes of 190 km (a and b) and 120 km (c and d) for low (a and c) and high (b and d) solar activity for modern conditions. The same color scale is used for each panel. Maximum densities are shown in purple and correspond to ~1.0 x 10^5 cm^{-3} [Source: *Bougher et al.* 2009b].

Seasonal influence is mostly characterized by variations in the long-waves and IR fluxes, decreasing with increasing heliocentric distance. This radiation is absorbed in the lower part of the atmosphere, which expands as a result. Therefore the ion peak, homopause and exobase heights rise together by about +12-15 km from the AL case to the PL case (Tables 5.1d and 5.1e). At the subsolar point, the ion peak height is then found at 116 and 128 km altitude for the aphelion and perihelion cases, respectively. The homopause is determined to vary in the very similar range of altitudes (115-130 km [*Stewart* 1987; *Bougher et al.* 2000]).

In all cases considered, the ion peak height increases, while its magnitude decreases with increasing SZA on the dayside, in good agreement with the reported observations of Viking [*Zhang et al.*, 1990], Mars Global Surveyor (MGS) [*Withers and Mendillo* 2005] and Mars Express (MEX) [*Morgan et al.* 2008]. Finally, spatial distribution of O_2^+ follows the background species local abundances and, because of higher concentration of ions in the polar region compared to lower latitudes (especially in the case of solstices), the magnitude of the ion peak undergoes a milder decrease and the ion peak height a sharper increase with SZA along the meridian than along the Equator.

V.1.4. Exobase altitude

Rigorously, the exobase level should be defined locally and for a transitional domain of multiple constituents. For the EL case, the exobase height undergoes significant spatial variations, reaching its lowest value of 155 km along the dayside terminator and at nightside low-mid latitudes, whereas the highest value of 195 km can be found in the polar regions (Section IV.1.5). It depends on the density of the bulk atmosphere, the mixing ratio of O/CO_2 and the temperature.

The exobase height exhibits a similar rise of about +15 km with solar activity and season, but for different reasons (Table 5.1e). The average exobase level rises from about 170 to 185 km altitude from the EL to the EH cases because of higher EUV heating, which occurs in the region above ~140 km, resulting in warmer temperatures and the general expansion of the upper atmosphere. These variations are not as large as 1D models predicted [*e.g. Ip* 1990], since they could not capture the important dynamical

effects. As mentioned above, the lower atmosphere (below 120 km) expands from the AL case to the PL case, resulting in a similar rise of the exobase height from 165 to 180 km altitude, respectively.

V.2. Exosphere

In this section, the description of the exosphere includes maps of the main macroscopic physical parameters, upward and downward exobase fluxes, and escape rate as function of SZA for different solar activities and seasonal conditions, as well as a discussion about the effects of bouncing (returning particles bouncing back from the nightside exosphere).

V.2.1. Variations with solar activity

V.2.1.1. Results

Above the transitional region (*i.e.* above ~600 km altitude), the oxygen population is 'hot', *i.e.* dominated by the suprathermal population (the criteria used in this study is $V_{threshold}$, which is defined as twice the local thermal speed in the transitional domain [*Valeille et al.*, 2009a]), and the scale height temperature is about T_{hot} ~4000 K, independent of the EUV inputs. Spatial distributions of the density for the EL case (Figure 5.6a) and for EH case (Figure 5.6c) are very similar, with density maxima located south of the subsolar point and minima achieved in the vicinity of the antisolar point at an altitude of 7000 km (*i.e.* 3 radii from the center of the planet). The shape of the hot corona is clearly inflated towards the dayside. At a given altitude, a uniform global enhancement in densities of a factor about x3 is estimated over the solar cycle.

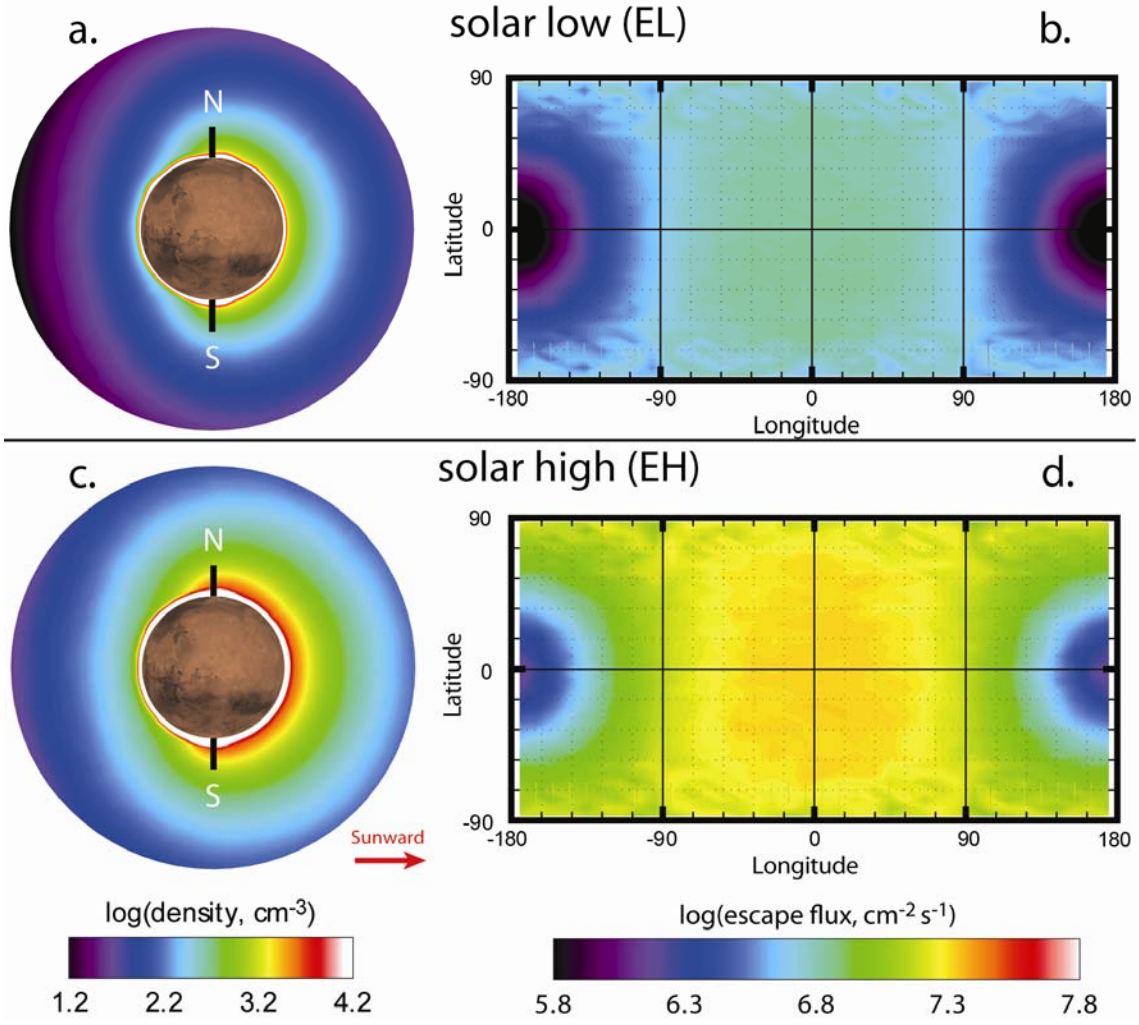

Figure 5.6. Density profiles (a and c) and escape fluxes at 3 Martian radii (b and d) of oxygen atoms at Equinox for solar Low (EL, a and b) and High (EH, c and d) conditions. The same color scale is used for each panel and is consistent with that for Figures 5.9 and 5.11. The North and South Pole positions are indicated by N and S, respectively. The red arrow points toward the Sun.

The spatial distribution of the escape flux is also very similar between the two cases and illustrated at 3 radii in Figures 5.6b and 5.6d, for EL and EH cases, respectively. Rather than an axisymmetric circular shape with respect to the subsolar point, it exhibits an oblong shape centered south of it and extends towards the Poles. The difference between extrema is a factor of about x10 at 3 radii, and decreases to about x4 at 10 radii [*Valeille et al.* 2009a]. The total escape rate increases by a factor x3-4 from 6.0 x 10^{25} s^{-1} for the EL case to 1.9 x 10^{26} s^{-1} for the EH case (Table 5.2).

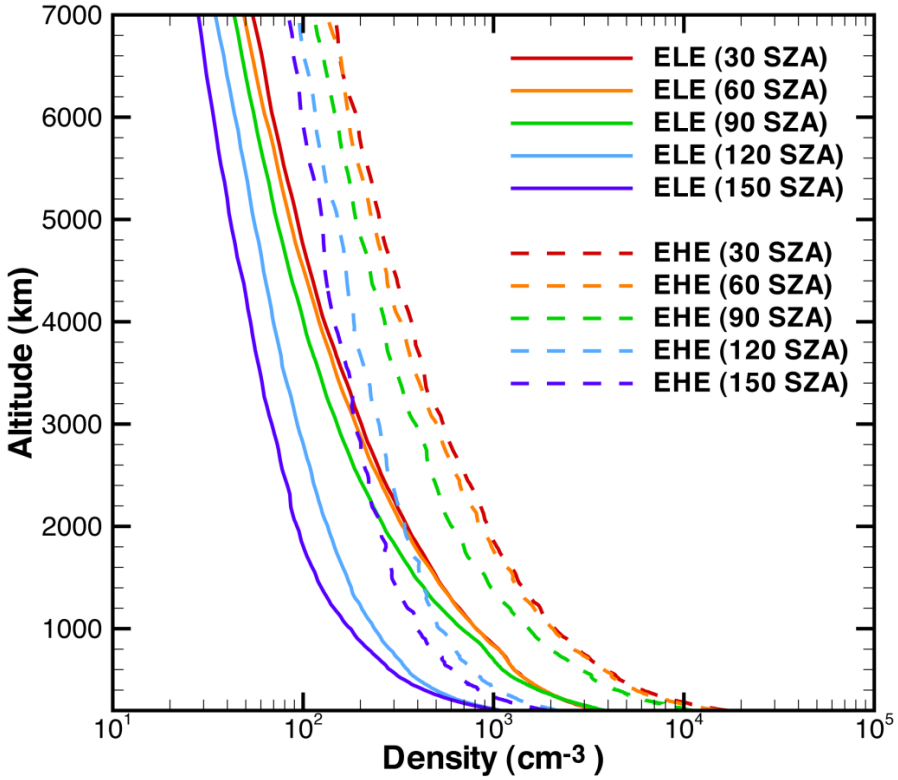

Figure 5.7. Hot oxygen density altitude profiles function of SZA and solar activity between 200 and 7000 km (~3 planet radii) altitude, along the Equator east. Results at 30, 60, 90, 120 and 150° SZA are presented in red, orange, green, blue and purple, respectively. ELE results are in solid lines, whereas EHE results are shown in dashed lines.

A plot showing both influences of SZA and solar activity on the hot oxygen density altitude profiles is presented on Figure 5.7. It can be seen that the day-to-night ratio in densities reduces from a factor of about ten in the vicinity of the exobase to only a factor of about three at 3 radii (~7000 km altitude), independently of the solar activity. Moreover, the factor of about three in densities between solar High and Low conditions seems to stay constant in this range of altitudes.

V.2.1.2. Comparison with other relevant studies

The understanding of the Martian upper atmosphere is an important subject and a number of theoretical quantitative works have been reported over the past ten years in an attempt to describe its extended hot atomic corona. However even today the information

about the hot species that form the Martian corona is very limited, and most of these models assumed an average thermospheric condition over the entire globe or used simple 2D extrapolations of 1D day and night assumptions. Table 5.2 is essentially an update of the comparison of the most recent models made by *Cipriani et al.* [2007] with the results of *Chaufray et al.* [2007] and the present study. Figure 5.8 can be consulted for a more qualitative comparison.

Table 5.2. Comparative study of the Martian hot atomic oxygen escape rates due to O_2^+ DR with other exospheric models of the last ten years with their respective thermospheric inputs and respective dimension (1D, 2D, 3D) of the simulations

Comparative Escape rates due to O_2^+ Dissociative Recombination (10^{25} s^{-1})					
Exospheric models		Thermosphere inputs		Solar LOW	Solar HIGH
Kim et al., 2001	2D	Kim et al., 1998[c]	1D	3.4	8.5
Hodges et al., 2002	3D	Kim et al., 1998[c]	1D	4.4	18.0
Krestyanikova et al., 2005	1D	Kim et al., 1998	1D	0.7	11.0
Cipriani et al., 2007	1D	Krasnopolsky, 2002	1D	0.6	2.6
Cipriani et al., 2007	1D	Kim et al., 1998	1D	2.1	5.0
Chaufray et al., 2007[a]	3D	Krasnopolsky, 2002[c]	1D	0.8	3.3
Present study[b]	2D	Bougher et al., 2006	3D	3.8	13.5

[a] corrected by a factor 1.95/2.4 accounting for a different O_2^+ DR production rate coefficient, inconsistent with the thermospheric inputs (*Peverall et al.* [2001] was taken when the study of *Krasnopolsky* [2002] took *Mehr and Biondi* [1969]).

[b] This is the only study that considers 3D thermospheric inputs and that includes, along with solar activity variability, comparisons between the polar meridian and the Equator at equinox and between the summer and winter polar meridians at perihelion and aphelion conditions respectively.

[c] The thermospheric inputs are 2D extrapolations of dayside and nightside 1D studies via linear interpolation with respect to the cosine of SZA. Dayside inputs are shown in this table. *Kim et al.* [2001] and *Chaufray et al.* [2007] used values from *Zhang et al.* [1990], whereas the values from *Hodges* [2002] are his corrected day-only ionosphere case. They should be increased by a factor of 6 when the values from *Fox et al.* [1993a] are used for the nightside.

The fact that both solar low and high values appear higher compared to the literature (illustrated in Figure 5.8) may come from the choice of the thermospheric input. The difference between solar low and high of a factor x4 is in accordance with other results (between x3 and x15).

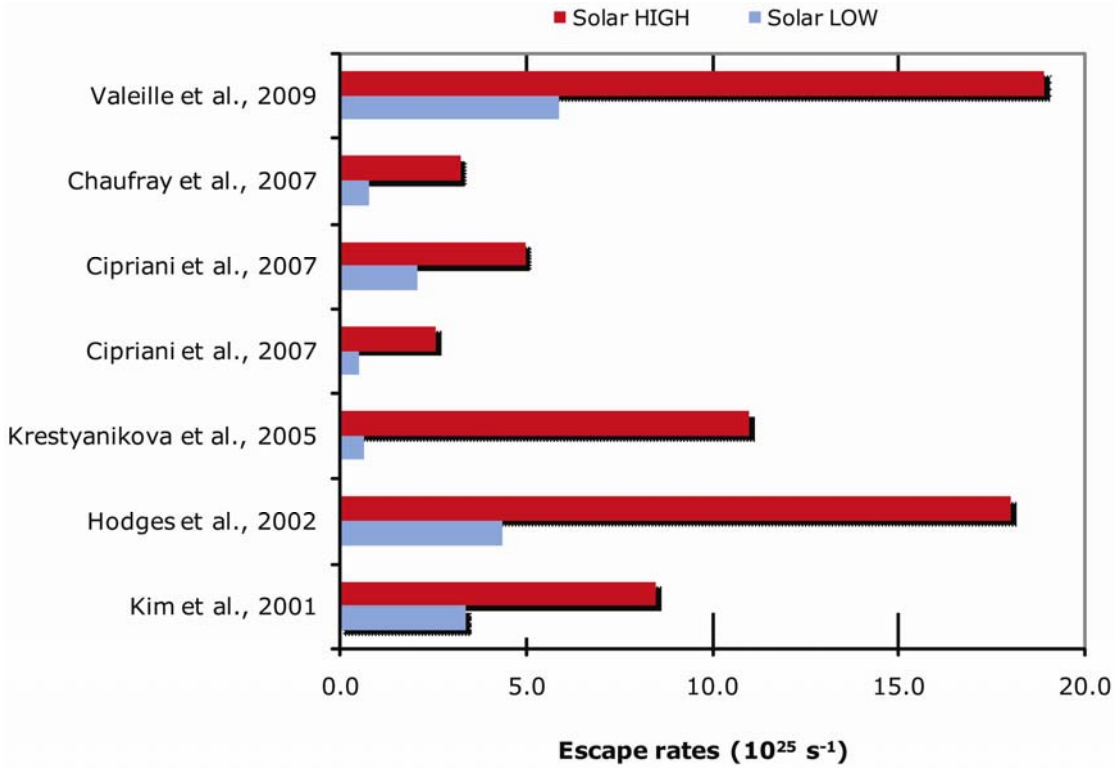

Figure 5.8. Comparative histogram of the hot atomic oxygen escape rates due to O_2^+ DR with other models of the last ten years for low (blue) and high (red) solar activity.

V.2.2. Variations with seasons

While seasonal variations are impacting the spatial distribution of most of the thermosphere parameters, their global effect is milder further away from the exobase, since the exosphere tends to homogenize the density due to average value over wider area. In the frame associated with the Sun, the spatial distribution of the density profiles between different seasons presents only slight variations, as illustrated at solar low activity in Figures 5.9a, 5.9c and 5.9e for the AL, EL and PL cases, respectively. Also, at a given altitude, the local densities undergo a milder increase between AL and PL (seasonal effect) than between EL and EH (solar cycle effect).

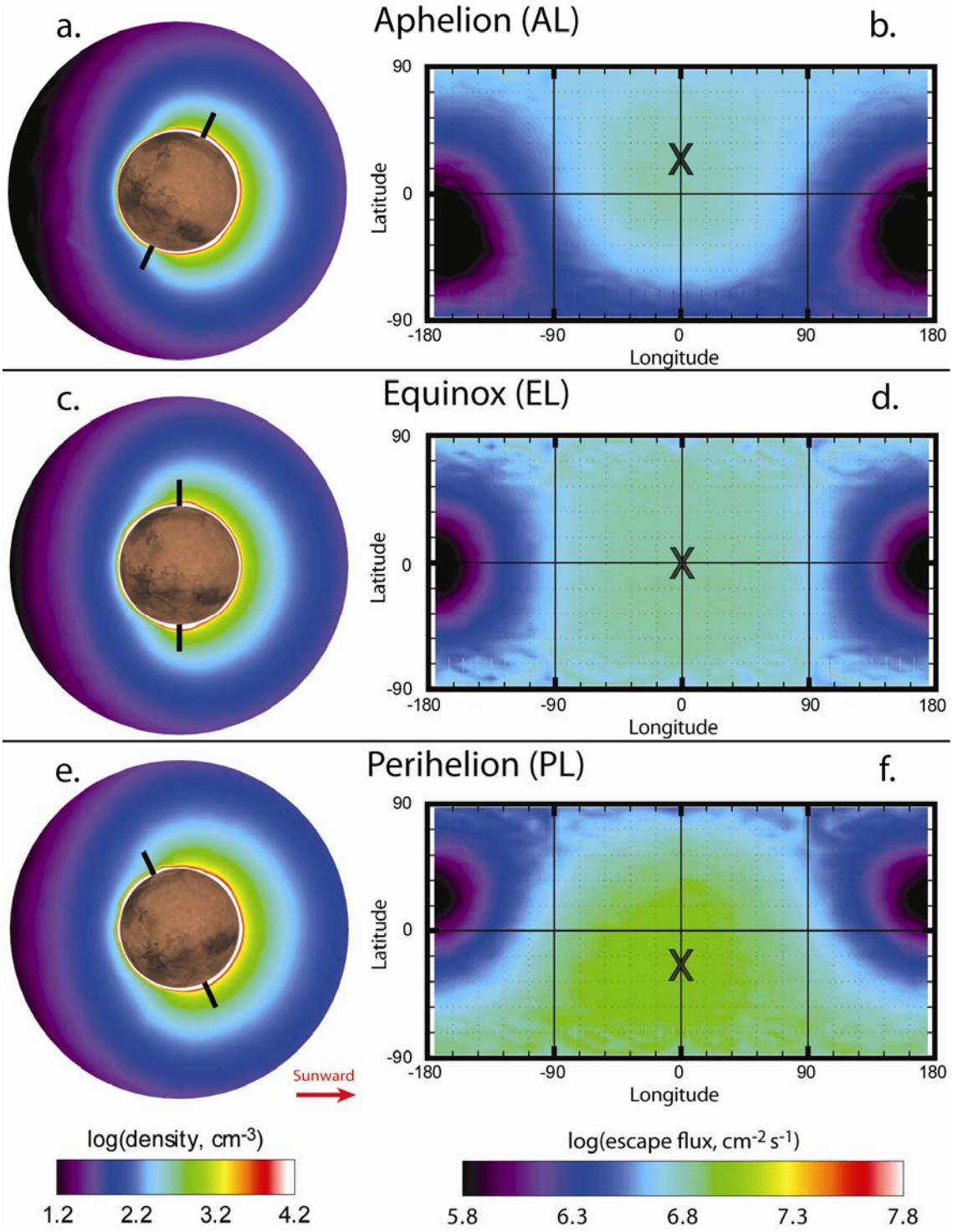

Figure 5.9. Density profiles (a, c and e) and escape fluxes at 3 Martian radii (b, d and f) of oxygen atoms for solar low activity at Aphelion (AL, a and b), Equinox (EL, b and c) and Perihelion (PL, e and f). The same color scale is used for each panel and is consistent with that for Figures 5.6 and 5.11. The black crosses mark the subsolar point. The North and South Pole positions are indicated by N and S, respectively. The red arrow points toward the Sun.

While, to first order, the equinox escape map is roughly axisymmetric with respect to the Mars-Sun axis (as shown for the EL case in Figure 5.9d), the axial tilt corresponding to the solstices cases has a very noticeable impact on the structure of the escape flux map (U shaped for the aphelion case, AL, in Figure 5.9b and N shaped for the perihelion case, PL, in Figure 5.9f). The peak of escape is still at the subsolar point but this location is shifted to +25° north latitude at aphelion and -25° south latitude at perihelion. The total escape rate increases from 4.6 for the AL case to 7.4 x 10^{25} s^{-1} for the PL case (Table 5.3). The relative variation with season in the escape rate is a factor about x1.6, which is close to the theoretical ratio of ~$(1.67/1.38)^2$ ~1.46 if the variation in the heliocentric distance only was considered between the two cases [*Valeille et al.* 2009a]. However, seasonal variations, as defined in this study, include more than the orbital position, but also the effect of the obliquity, dust activity and hemispheric asymmetries that result in important changes in the lower atmosphere, and therefore affect both thermosphere and exosphere [*Bougher et al.* 2006].

Table 5.3. Impact of season and solar cycle on the escape rate of suprathermal oxygen atoms

		Orbital position		
		Aphelion	Equinox	Perihelion
Solar activity	Low	4.6 x 10^{25}	6.0 x 10^{25}	7.4 x 10^{25}
	High		1.9 x 10^{26}	2.6 x 10^{26}

V.2.3. Extreme cases for modern conditions

As noticed previously for EHP and ELP conditions, Figure 5.10 shows that all cases follow the same trend, decreasing by a factor of about three from noon to midnight. Furthermore, at an orbital position of equinox, the influence of the solar cycle is found to be of a factor of about three between high and low solar activities, in agreement with previous studies (compared in Table 5.2). The total seasonal influence on the corona is evaluated to be a factor two when adding the differences between equinox and perihelion cases (summer hemisphere), and equinox and aphelion cases (winter hemisphere), when solar activity is fixed to either high or low respectively. It may be interesting to note that,

in a 1D problem, if the distance of Mars from the Sun was only considered, a ratio of ~ $(1.67/1.38)^2$ ~ 1.46 in the escape rates should be expected between Aphelion and Perihelion cases. However, higher dimensions allow a better description by taking into account other parameters than the heliocentric distance only. The range of obliquity of Mars is substantial (± 25.19 degrees tilt), as is its effect on tidal winds. Both Martian lower and upper atmospheres are also subject to dynamical effects that are modulated by seasons. For example, dust influence is more important at Perihelion than at Aphelion, driving stronger inter-hemispheric (summer-to-winter) winds. Furthermore, polar warming features, resulting from this inter-hemispheric flow, are most pronounced in the winter hemisphere during Perihelion conditions [*Bougher et al.* 2006]. All those seasonal effects are pictured by the ALP and PHP simulations presented here. This result is very close to the influence of the solar cycle, illustrating the necessity of the orbital position to be considered by exospheric models. Both of those long-term temporal variations of the escape rate are considerable and the two most extreme cases illustrated by PHP and ALP conditions present a difference as high as a factor of about six, setting a lower and upper limit for the modern escape rates as a function of time.

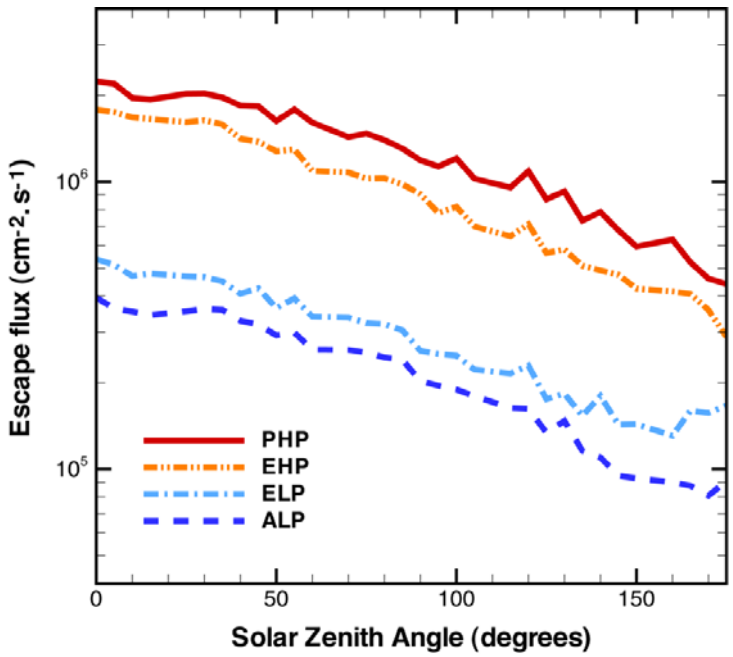

Figure 5.10. Escape fluxes of hot oxygen atoms along the south Polar cut as a function of SZA for PHP (solid red line), EHP (dashed-dotted-dotted orange line), ELP (dashed-dotted light blue line) and ALP (dashed dark blue line) conditions at 10 Martian radii.

The data in Table 5.3 illustrate the effects of two long-term temporal variations of the Martian exosphere and the escape rate of suprathermal oxygen atoms: solar activity (about an 11-year period) and the Martian orbital position (about a 2-year period). From those results, an approximately 22-year average escape rate of about 1.0 x 10^{26} s^{-1} (*i.e.* about 2.7 kg s^{-1}) can be considered. Steady-state conditions, where ionospheric parameters are constant, were assumed for each case considered in this study. Recent papers [*Kaneda et al.* 2007, 2009] indicate a possible mechanism that can cause a short-term (about 2000-seconds period) enhancement of the hot oxygen escape rate in response to a sudden increase in the solar wind dynamic pressure. The escape rate was found to increase by a factor of about two; and it should be noticed that these results, if somewhat smaller than the total influence of the seasonal variation and the solar cycle, are of the same order.

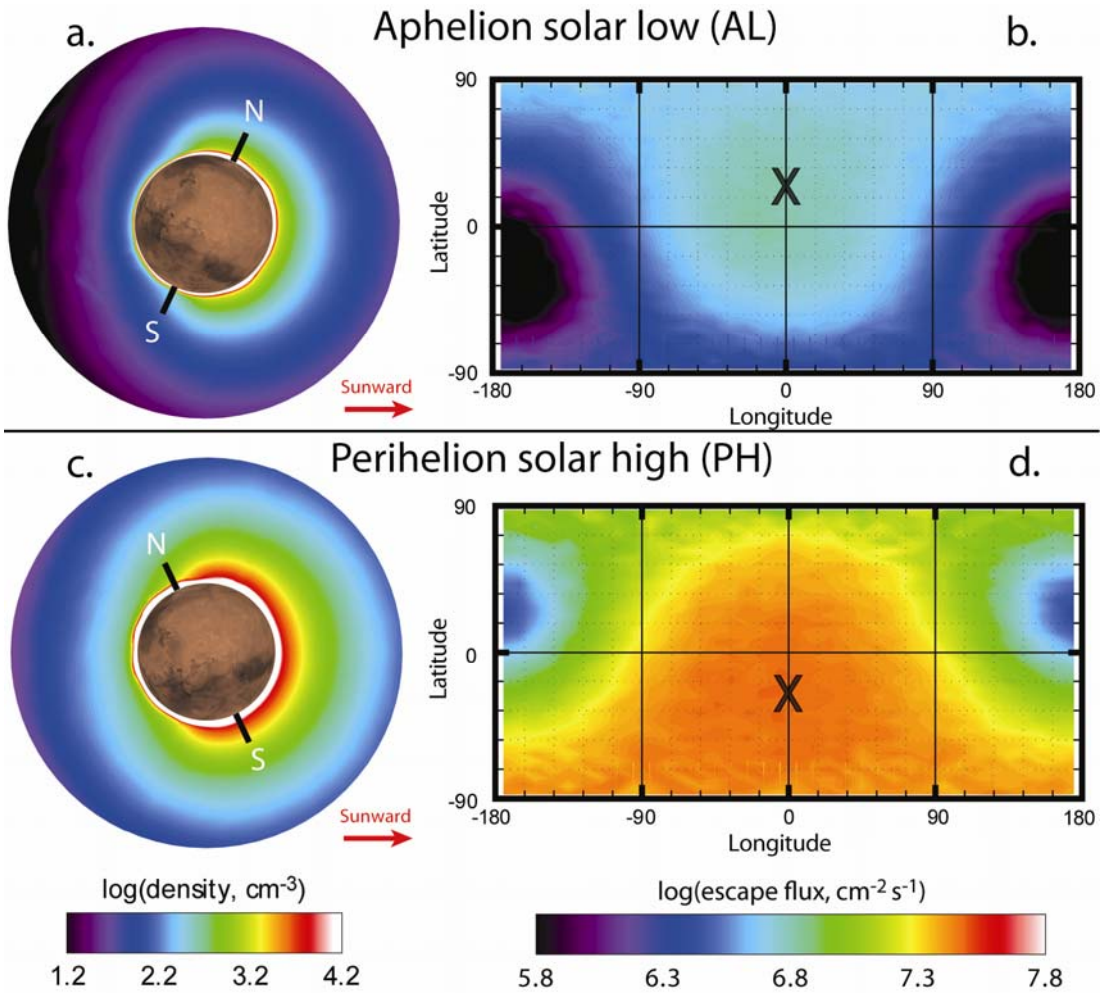

Figure 5.11. Density profiles (a and c) and escape fluxes at 3 Martian radii (b and d) of oxygen atoms for the two most extreme cases for modern conditions, Aphelion solar Low (AL, a and b) and Perihelion solar High (PH, c and d). The same color scale is used for each panel and is consistent with that for Figures 5.6 and 5.9. The black crosses mark the subsolar point. The North and South Pole positions are indicated by N and S, respectively. The red arrow points toward the Sun [Source: *Bougher et al.* 2009b].

V.3. Discussion

Table 5.3 illustrates the comparable impacts on the atmospheric loss of two long-term temporal variations: the solar cycle (about an 11-year period) and the seasonal effect (about a 2-year period). In this section, a periodic trend of these phenomena is estimated and scaled to the results of the simulation in order to get a semi-quantitative understanding of their cumulative variation with time.

The International Sunspot Number, previously known as the Zürich series, is often used as an index of solar activity (in blue in Figure 5.12a). Data are taken from the homepage of the Solar Influences Data Analysis Center (SIDC) [Source: http://sidc.oma.be/]. F10.7 has been shown to follow the sunspot number quite closely and similar prediction techniques can be used. They both are closely related to solar activity. Its short-term and long-term prediction is highly important for space weather applications [*Podladchikova et al.* 2007]. A monthly average (in red in Figure 5.12a) is used in order to eliminate the difference of orbital position of Mars and Earth with respect to the Sun (the Sun rotation being ~25.4 days). A cosine approximation fits reasonably well the variations and the last three cycles in particular, as shown in Figure 5.12. The solar minimum reference (solar low) was taken on June 2006.

Under the simple assumption that escape rate is proportional to solar radiation, the cosine fit is then used to approximate the variation of the escape rate with solar activity at Mars semi-major axis (*i.e.* about 1.52 AU from the Sun) in black in Figure 4b and extended for predictions of the near future. While Earth orbit is nearly circular, Mars orbit is highly elliptical. The modulation due to the seasonal effect is approximated by an ellipse (in red in Figure 5.12b). The heliocentric distance at aphelion is 1.67 AU, while perihelion is 1.38 AU. The period is 687 days and the perihelion reference is taken on August 2003.

This illustrates clearly that solar cycle and seasons have a comparable and significant influence on the escape, and therefore both effects should be taken into consideration for a rigorous description. Indeed, the cumulative effect of these long-term periodic variations is estimated to be a factor of about x6 in the atmospheric loss between the two extreme cases of AL and PH, setting a lower and upper limit for the modern conditions. Those results have important implication for ion production, and therefore the population of the ionosphere that in turn regulates ion escape and sputtering in its interaction with the solar wind.

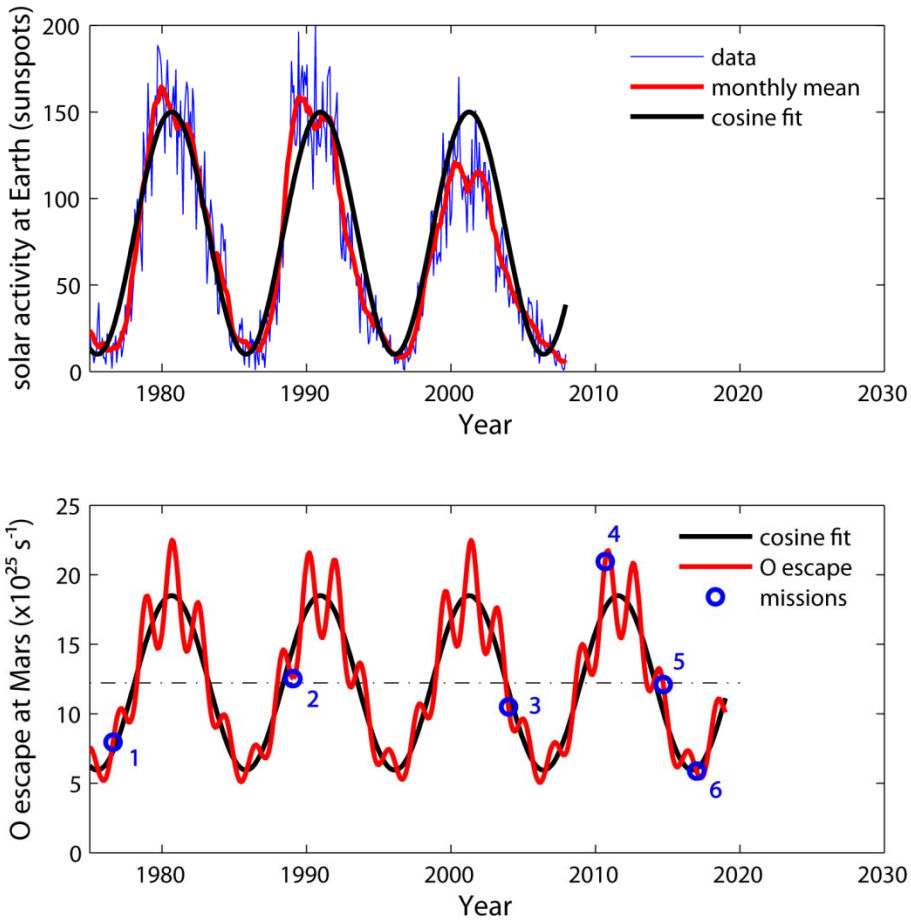

Figure 5.12. (a) Trends of the measured solar activity at Earth (1 AU). The daily sunspot number data, as reported by the Royal Observatory of Belgium, are represented in blue, the monthly averages in red and the cosine fit in black. (b) Extrapolation and prediction of the total oxygen escape rate at Mars by the current study. The average computed escape rated is represented in the black dashed-dotted line. The cosine fit at the average orbit (~1.5 AU) is represented in black and the modulation due to orbital position in red. Arrivals at Mars of past, current and future missions to Mars (equipped with instruments capable of upper atmospheric density measurements) are numbered and represented by blue circles (see details in the text).

Past and future missions to Mars relevant to the oxygen escape are represented as blue circles in Figure 5.12b. The only *in-situ* measurements of the Martian upper atmosphere currently available are from Viking 1 and 2 mission descents corresponding to the EL case (1 in Figure 5.12b). Since then, the ASPERA 1 and 3 instruments onboard Phobos 2 and MEX (2 and 3 in Figure 5.12b, respectively) provided valuable indirect information from ionospheric observations for solar moderate to high and mostly solar low conditions, respectively. While the instruments on the Viking missions could not

detect the hot oxygen corona, the upcoming missions, Phobos-Grunt and Yinghuo-1, Mars Scout Mission (MAVEN) and ExoMars scheduled to arrive in 2011, 2014 and 2017 (4, 5 and 6 in Figure 5.12b, respectively) may be able to measure densities of hot oxygen around Mars for an extended period of time. Indeed, depending of the interval of sampling (looking at Figure 5.12b), measurements over a year might be enough to appreciate significant variations in the densities of the hot corona and in the atmospheric escape.

Although Figure 5.12a provides the long-term periodic variations due to seasons and solar activity, a spacecraft would also have to take into account spatial variations. The most important being the decrease due to altitude (1D symmetrical), then the day-to-night (2D axisymmetric), and finally the local features (full 3D), as demonstrated in the study of *Valeille et al.* [2009c]. Recent papers [*Kaneda et al.* 2007, 2009] indicate a possible mechanism that can cause a short-term (about 2000-seconds period) enhancement of the hot oxygen escape rate in response to a sudden increase in the solar wind dynamic pressure. The escape rate was found to increase by a factor of about two; and it should be noticed that these results, if somewhat smaller than the total influence of the seasonal variation and the solar cycle, are of the same order.

Chapter VI
Evolution over Martian history

VI.1. Introduction

The question of how much water exists on Mars today and in the past is still hotly debated, especially when it implies the possibility of life. A number of comparative studies have been reported over the past ten years in attempt to describe the global evolution of the planet and its climate [*e.g. Jakosky and Phillips* 2001; *Lammer et al.* 2003; *Chassefière and Leblanc* 2004; *Chassefière et al.* 2007]. The oxygen escape rate is known to be a good approximation of water loss from the planet [*Hodges* 2002]. CO_2 is the obvious parent of escaping O, and re-oxidation of the CO produced implies destruction of water.

In this study, generous estimates of the secondary processes of atomic oxygen escape are presented and compared with conservative calculations of the escape due to O_2^+ DR. Finally, even within the most favorable conditions in the past, up to ~3.5 Gyr ago, oxygen is too heavy to escape from Mars thermally (a generous estimate of Jeans thermal escape rate at that time being several orders of magnitude less than the conservative estimate of other escape processes), therefore thermal escape of oxygen is assumed negligible in this work.

To obtain the trend of oxygen escape with time, an exospheric simulation that can incorporate thermospheric/ionospheric inputs for different solar IR/EUV conditions is highly desirable. Until now, only one study [*Zhang et al.* 1993b] combined thermospheric/ionospheric calculations of ancient atmospheres with an exospheric description. Their results were used afterwards by many other studies, together with their

own modern escape rates, to propose various estimates of the water loss over Martian history [*e.g. Hodges* 2002; *Lammer et al.* 2003]. The oxygen escape rates from *Zhang et al.* [1993b] were first corrected by *Luhmann* [1997], setting the value of the x1 present EUV case to ~6 x 10^{24} s^{-1}, close to the 5.3 x 10^{24} s^{-1} value of the study of *Kim et al.* [1998], which used the same method and inputs. This latter value was however corrected by *Nagy et al.* [2001] up by a factor ~6.5 (*Kim et al.* solved a 1D problem and extrapolated the result over both day and night hemispheres). This 1D study of *Zhang et al.* [1993b] involved the calculation by the two-stream method of *Nagy and Banks* [1970] of the exospheric hot oxygen densities and the associated escape rates, with flux inputs at the exobase taken from the past Mars 1D (M1D) code [*Bougher and Dickinson* 1988], precursor of the current MTGCM [*Bougher et al.* 2006] used in the present work.

The same general approach is followed here but with updated 3D thermospheric/ionospheric inputs and our DSMC exospheric code that does not assume a strict separation between collision and collisionless domains as explained in Chapter III. The major difference between the past M1D and the current MTGCM model framework is that thermospheric dynamics is taken into account in the current version. Indeed, 1D models do not capture dynamical effects but instead simulate them by employing eddy mixing coefficients. In fact, large-scale winds rather than eddy diffusion are largely responsible for the main mixing effects in the Martian thermosphere. Those effects are important as they redistribute the balance between heating and cooling sources on the dayside and nightside, affecting the entire thermospheric structure, which in turn governs the hot species population of the exosphere. While dynamics can be neglected in the Venus case where EUV heating balances the 15-μm cooling on the dayside, its effect is important on Mars as it balances the heating inputs and is a major dayside cooling mechanism [*Bougher et al.* 1999, 2000].

The two main differences in the assumptions made in this study compared to most of the previous works on the upper atmosphere of ancient Mars, are that: 1- Not only are enhancements in the solar EUV fluxes considered for the early Sun, but also the decrease in the IR, affecting both the thermosphere/ionosphere and the exosphere, and 2- Both solar low and high conditions are estimated for the present and for the past.

Assumption 1 is made to be consistent with the "weak" young Sun [*Guinan and*

Ribas 2002]. Indeed the Sun radiation changed not only in the EUV but also in the IR, and both variations are considered in this study. IR fluxes are scaled by a factor 0.79.

Assumption 2 is made because, although most exospheric models of the last ten years agree upon a difference of about a factor three to four in escape rates within a solar cycle [*Kim et al.* 2001; *Hodges* 2002; *Cipriani et al.* 2007; *Chaufray et al.* 2007; *Valeille et al.* 2009a, 2009d], the only work on the upper atmospheres of ancient Mars that considered any variation with the solar cycle in the past is the study of *Valeille et al.* [2009b]. Indeed, considering the differences in the solar fluxes between solar low and high conditions, a difference as high as of a factor of about two in the EUV changes the results greatly, as previously noted by the work of *Chassefière et al.* [2007] and demonstrated in the study of *Valeille et al.* [2009b]. This study [*Valeille et al.* 2009b] shows that the magnitudes of these 11-year periodic variations in the hot corona are comparable to those during the evolution over the last ~3.6 Gyr. It is however important to keep in mind that it is difficult to extrapolate to earlier epochs of the solar system without better knowing the evolution of the solar cycle in history, both in period and amplitude.

Therefore, and for the sake of clarity, three epochs of the solar system are defined. Those correspond to: present (denoted by epoch 1), ~2.7 Gyr ago (epoch 2), and ~3.5 ± 0.1 Gyr ago (epoch 3). This new notation is closely related to the one used by past studies tied to the EUV flux enhancement in the past and often denoted 1 EUV, 3 EUV, 6 EUV. Epoch 1 corresponds to present solar conditions (x1 EUV, x1 IR), epoch 2 corresponds to 3 times the present solar EUV flux and 0.79 times the present solar IR flux (x3 EUV, x0.79 IR), and epoch 3 corresponds to 6 times the present solar EUV flux and 0.79 times the present solar IR flux (x6 EUV, x0.79 IR).

For the first time, those epochs are considered for both solar low and high conditions, with the assumption that the amplitude of the solar cycle was the same in the past as at present. The only exception is that epoch 3 corresponds to the numerical stability limit of the MTGCM, which is x6 EUV for solar low and x5 EUV for solar high conditions. Therefore, epoch 3 refers rigorously to ~3.6 Gyr ago for solar low and to ~3.4 Gyr ago for solar high conditions.

Planetary escape mechanisms depend on densities of the main constituents (O, CO_2, O_2^+ on Mars), temperatures and winds in the upper thermosphere. Solar radiation affects

all those parameters, thus the evolution of planetary atmospheres must be understood within the context of the evolving solar energy and solar wind conditions. A model of the evolving EUV luminosity [*Ribas et al.* 2005], taken from a study of the *Sun in Time* program and based on observations of solar-type stars, is used as a guide in adjusting conditions to represent the past. Epochs 1, 2 and 3, as defined earlier, correspond to present, ~2.7 Gyr ago, and ~3.5 ± 0.1 Gyr ago, respectively. About 3.5 Gyr ago, the last cataclysmic impact event might have removed the atmosphere and the magnetic field from the planet. Before this, impact erosion could have played an important role in removing the early atmosphere of Mars, because of its small radius and low gravitational acceleration [*Walker* 1987; *Melosh and Vickery* 1989]. Moreover, Mars would still have had an active magnetic field, which would, at least partially, protect its atmosphere from the solar wind and, therefore, from the sputtering by pickup ions [*Acuña et al.* 1998]. Those conditions can also be roughly related to the three Martian epochs: between epoch 1 and epoch 2 is the Amazonian, between epoch 2 and epoch 3 is the Hesperian, and before epoch 3 is the Noachian.

Furthermore, it seems likely that the predominantly CO_2 atmosphere appeared within 100 Myr of the formation of the planet [*Hodges* 2002]. And, as there are apparently no efficient escape mechanisms for carbon on Mars [*Hanson et al.* 1977; *Fox and Hac* 1999; *Nagy et al.* 2001; *Cipriani et al.* 2007], it is assumed in this study that the background atmosphere composition has not changed since that time. This is a strong assumption as carbon sinks, such as formation of carbonates, CO_2 ice in the regolith or polar caps [*Haberle* 1998], might have played a more important role in the past, and the early atmosphere should have been significantly richer in H, H_2 and O [*Fox* 2003]. Therefore, estimates of water loss should be considered here for Mars atmospheres no younger than ~1 Gyr.

VI.2. Thermosphere/Ionosphere

Similar to the influence of the solar cycle, the influence of the epochs affects the magnitude of most of the thermospheric parameters, while their general spatial distribution is mostly unchanged.

First, the 3D MTGCM is presented for different solar inputs at different epochs (namely epoch 1, 2 and 3) at the fixed orbital position of equinox and for both solar low and high conditions.

VI.2.1. Temperatures, heating and winds

Figure 6.1 compares day and night temperature profiles, as well as their variations with time. Present and past Martian thermospheres see their neutral temperature increase with altitude first, and then become isothermal above some level. This level is reached at lower altitudes at night compared to day (dashed versus solid lines in Figure 6.1), and at present compared to past (for example, while this level is attained at ~160 km for present conditions -epoch 1-, it may have been at ~240 km in the past -epoch 3-).

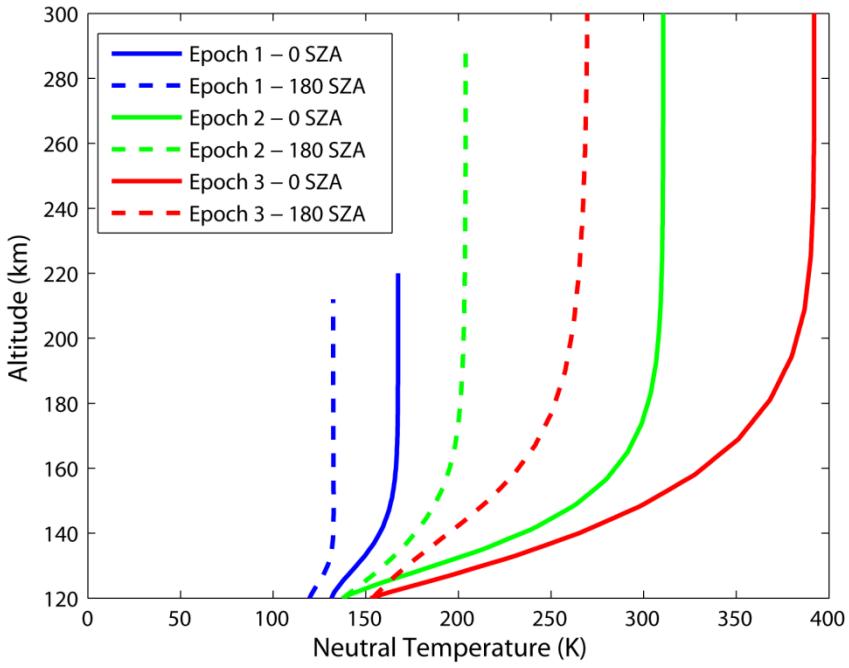

Figure 6.1. Profile of the neutral temperature in the Martian upper thermosphere (120 to 300 km altitude) at the Equatorial noon (0° SZA) for epoch 1, 2 and 3 (blue, green and red lines, respectively) for solar low conditions.

Neutral thermospheric temperatures are found to be higher in the past (for solar low, at Equatorial noon: T_∞ ~170, 310, 390 K for epoch 1, 2, 3, respectively). Those values are significantly less than the ~200, 350 and 600 K dayside average 1D estimates of previous studies [*Zhang et al.* 1993b; *Lammer et al.* 2003]. This is due mostly to the inclusion of the cooling effect of the day-to-night dynamics in the current MTGCM study. In this regard, horizontal and vertical winds can be seen as a thermostat regulating the effect of the increase of the past solar EUV fluxes in the Martian thermosphere.

The night-time neutral temperatures follow the same trends (dashed lines in Figure 6.1), and the day/night difference is more important (T_{day}-T_{night} ~ +40, +100, +120 K) for stronger EUV cases (x1, x3, x6 EUV, respectively).

Several processes determine the Martian thermospheric temperatures and their variability [*Bougher et al.* 1999, 2000, 2009a]. These processes include: (1) solar EUV-UV fluxes producing heating, and its changes with solar cycle, distance from the sun, and local solar declination, (2) molecular thermal conduction, (3) CO_2 15-μm cooling, and (4) horizontal advection and adiabatic heating/cooling associated with global dynamics. According to *Bougher et al.* [1999, 2000, 2009a], the primary dayside balance for present day Mars occurs between EUV heating and molecular thermal conduction, with CO_2 cooling playing a relatively minor role. In addition, Mars adiabatic cooling, due to rising motions on the dayside from the global circulation, should play a progressively more important role as the solar cycle advances. This "dynamical thermostat" cannot be ignored when examining the heat balances, giving rise to solar cycle and seasonal variations of Martian thermospheric neutral temperature. 3D models are thus essential for a proper investigation of Martian thermospheric heat balances [*Bougher et al.* 2009a].

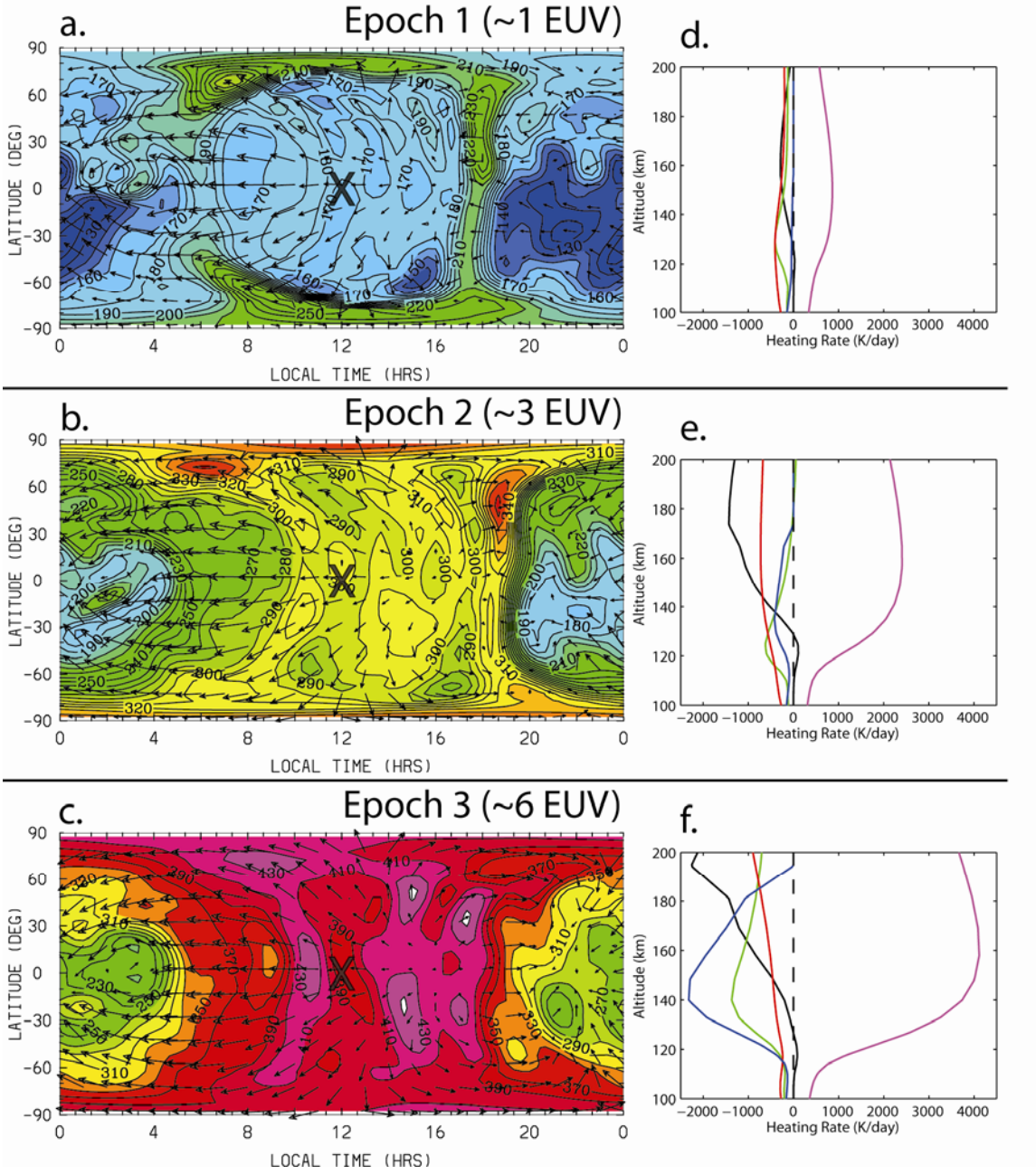

Figure 6.2. Surface maps of the neutral temperature for epoch 1, 2, 3 (a, b, c, respectively) for solar low conditions at 190 km altitude. Horizontal wind velocities are represented by arrows (maximum at ~490, 530 and 600 m s^{-1}), and the same color scale is used for temperatures (10, 10 and 20 K increments for epoch 1, 2, 3, respectively). Minimum temperatures are in dark blue - light blue and correspond to 130-170 K, while maximum temperatures are in red - purple and correspond to 370-430 K. For each case (epoch 1, 2, 3), the black cross represents the location of the Equatorial noon where the heating rate profiles (d, e, f, respectively) are computed between 100 and 200 km altitude. Thermal conduction (black line), horizontal advection (green line), adiabatic warming (red line), total heating EUV + Near Infra Red (NIR) (pink line) and total Infra Red (IR) 15-μm cooling (blue line) are presented.

Figures 6.2a-c illustrate maps of simulated MGCM-MTGCM neutral temperatures at 190 km altitude. Figures 6.3b, 6.3d and 6.3f show also neutral temperatures and winds, but at the respective exobase levels for epoch 1, 2, and 3, respectively. The general temperature structure is not significantly different in the past, with minima situated south at low and mid latitudes on the nightside. Maxima are located on the dayside in the polar regions and in the vicinity of the evening terminator, with the exception for the extreme case of epoch 3 where maxima are closer to the subsolar point (Figure 6.3f). The average neutral temperature, T_∞, (170, 260 and 360 K), the amplitude between extrema (+180, +200 and +260 K) and the maximum wind speed (490, 530 and 610 m s^{-1}) increase significantly with higher EUV fluxes consistent with ancient Mars conditions (for epoch 1, 2 and 3, respectively).

Corresponding thermal balances for Equatorial noontime conditions (*i.e.* 0° SZA) are illustrated in Figures 6.2d-f. It is important to notice that sub-solar temperatures are still under the basic control of local EUV-UV heating and molecular thermal conduction, even as solar fluxes are enhanced for ancient Mars conditions. However, the impact of global winds (*i.e.* upwelling and associated adiabatic cooling) becomes progressively more important as solar fluxes are enhanced (epoch 2 and 3). This is consistent with the growing magnitude of global winds for these ancient Mars simulations.

In addition, CO_2 15-µm cooling becomes progressively more important into the past. This situation results from the growing atomic O abundance as CO_2 net dissociation is enhanced for larger solar EUV-UV fluxes for ancient Mars conditions. In fact, Figure 6.2f (epoch 3) shows a significant role of CO_2 15-µm cooling for balancing dayside EUV-UV heating, a condition similar to present day Venus conditions [*Bougher et al.* 1999]. This important result suggests that the ancient Mars thermosphere (of about 3.5 ± 0.1 Gyr ago) was very similar to the present Venus not only in terms of bulk composition, but also in terms of heat balances. This similarity between present Venus and ancient Mars could be explained by the fact that the solar flux at Venus (~0.7 AU) is about 4.5 times that of Mars (~1.5 AU) for present conditions (and therefore somewhat close to the ancient Mars conditions at epoch 3) [*Valeille et al.*, 2009b].

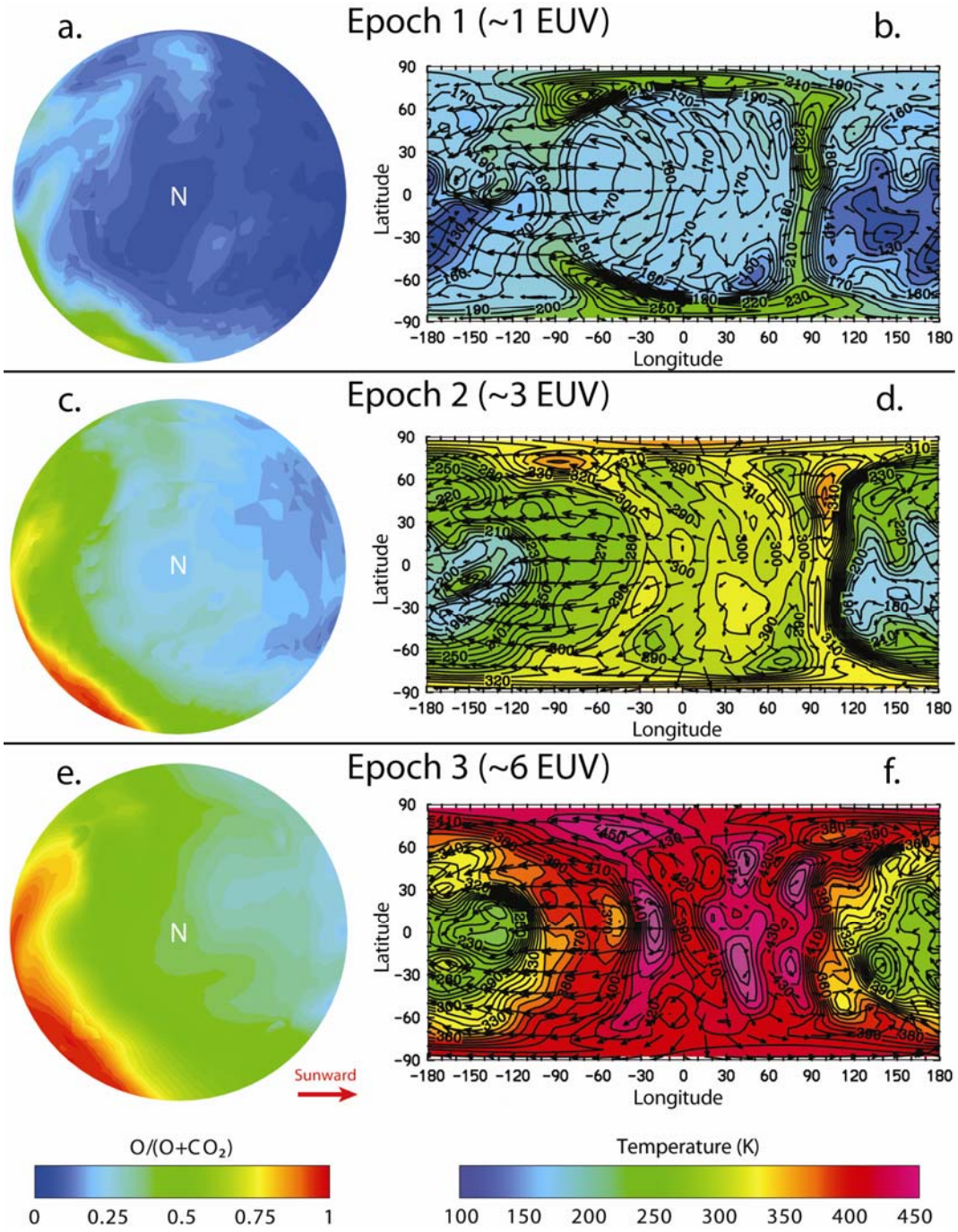

Figure 6.3. Oxygen mixing ratio in the winter hemisphere (a, c and e) and neutral temperature in the vicinity of Mars exobase (b, d and f) at epoch 1, 2 and 3. The results are shown for the EL conditions at the respective average exobase level, *i.e.* at an altitude of 170, 190 and 220 km for epoch 1 (a and b), epoch 2 (c and d) and epoch 3 (e and f), respectively. Horizontal wind velocities are represented in the frame associated with Mars by arrows with maxima at ~490 (b), ~530 (d) and ~610 m s^{-1} (f). The same color scale is used for each panel and is consistent with that for Figure 6.2. The North and South Pole positions are indicated by N and S, respectively. The red arrow points toward the Sun.

VI.2.2. O and CO_2 density distribution

The O to CO_2 ratio is a particularly important parameter of the Martian upper atmosphere, as both species are present at comparable abundances in the vicinity of the exobase. The ratio affects the exobase height, the plasma heating, as well as the escape loss due to incident pickup ions [*Leblanc and Johnson* 2002]. Figures 6.3a, 6.3b and 6.3c present the O mixing ratio at respective exobase heights for epoch 1, 2, and 3, respectively. The O mixing ratio exhibits the same structure in the past and at present, with a clear day-to-night difference. Minima are on the dayside at low northern latitudes, maxima at low south-west latitudes. The average value of the O mixing ratio at the exobase increases due to a higher exobase altitude in the past. Also, stronger winds result in higher O abundances on the nightside.

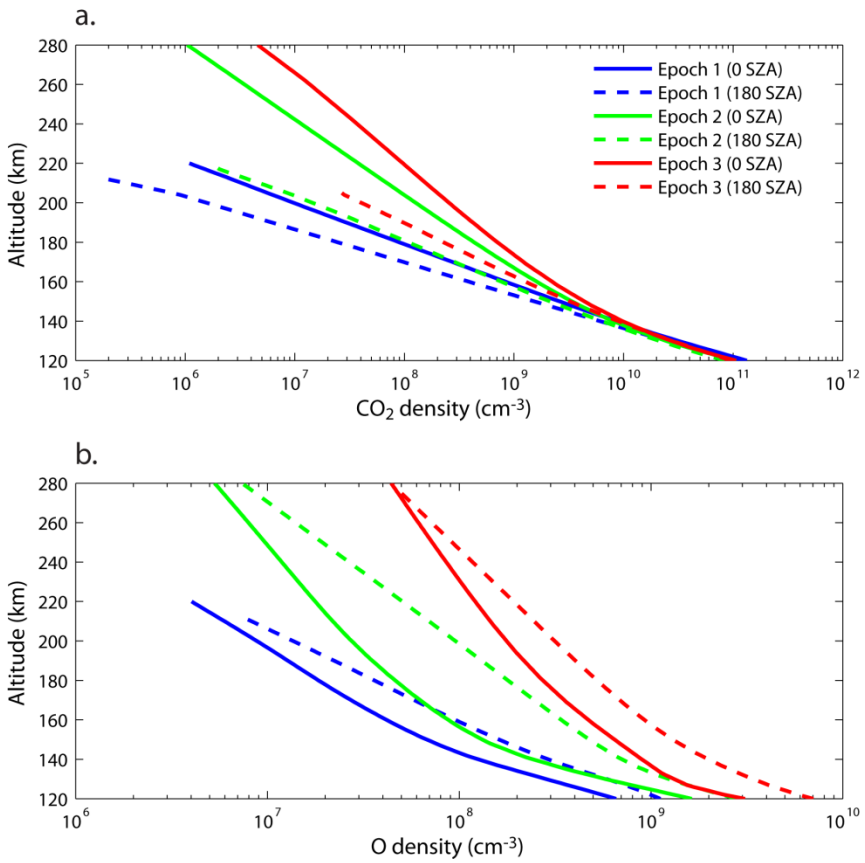

Figure 6.4. Density profiles of the two main neutral constituents of the Martian upper thermosphere (120 to 280 km altitude), CO_2 (a) and O (b), at the Equatorial noon, 0° SZA, and midnight, 180° SZA, (solid and dashed lines, respectively) for epoch 1, 2, and 3 (blue, green and red lines, respectively) for solar low conditions.

At a given altitude, an enhancement in density of a factor about x13 is estimated between epoch 1 and 3. This increase in the background densities at a fixed altitude is due to higher thermospheric temperatures in the past, which affect the scale heights of the constituents proportionally, resulting in a general expansion of the atmosphere. The ion production is expected to be higher at places where CO_2 is dominant locally. The plasma heating would also be higher, whereas the sputtering yield and the escape loss due to incident pickup ions should decrease due to a lower atom-to-molecule ratio [*Leblanc and Johnson* 2002].

The two main constituents in the upper thermosphere of Mars are CO_2 and O. The mean altitude of the Martian dayside homopause at present varies with the seasons at ~115-130 km over the surface [*Stewart* 1987; *Bougher et al.* 2000]. Figures 6.4a and 6.4b illustrate how the ancient upper thermospheres may have evolved over time. The present atmosphere density profiles measured by the Viking Lander 1 [*Hanson et al.* 1977, *Nier et al.* 1977] sit between the noon and midnight profiles presented here (epoch 1). In Figure 6.4a, day and night, past and present CO_2 density profiles are very similar above the ion peak up to 140 km altitude, above which they part with different scale heights given in Table 6.1. Scale heights on the nightside are significantly lower than corresponding ones on the dayside (consistent with cooler nightside temperatures).

Table 6.1. Scale heights (in km) of the main neutral (CO_2 and O) and ion (O_2^+) constituents of the Martian upper thermosphere at noon and midnight for epoch 1, 2 and 3 for solar low conditions

		Epoch 1 (~1 EUV)		Epoch 2 (~3 EUV)		Epoch 3 (~6 EUV)	
		Noon	Midnight	Noon	Midnight	Noon	Midnight
$H(CO_2)$	in the ~140-280 km region (km)	9	7	17	9	20	12
H(O)	in the ~160-280 km region (km)	26	20	49	33	58	42
$H(O_2^+)$	in the ~125-180 km region (km)	23		36		49	

The difference of a factor of about two at 120 km altitude between day and night O density profiles grows larger in the vicinity of the exobase before getting smaller for higher altitudes. This change in the slope of dayside density profiles may be attributed to the effects of dynamics that efficiently transports oxygen atoms towards the nightside, smoothing out the day/night difference in densities. Ancient upper atmospheres present similar trends with larger scale heights (shown in Table 6.1).

Table 6.2. Altitude (km), above which O becomes the main neutral constituent of the Martian upper thermosphere, for epoch 1, 2 and 3 for both solar minimum and maximum conditions (dayside and nightside values are presented along with the average value, rounded to nearest 5 km)

	Solar minimum			Solar maximum		
	day	average	night	day	average	night
Epoch 1 (~1 EUV)	210	190	170	240	205	175
Epoch 2 (~3 EUV)	230	190	145	260	200	140
Epoch 3 (~6 EUV)	240	190	140	270	205	140

The O to CO_2 ratio is a particularly important parameter of the Martian upper atmosphere, as both species present a comparable abundance in the vicinity of the exobase. The ratio affects the exobase height, the plasma heating, as well as the escape loss due to incident pickup ions [*Leblanc and Johnson* 2002]. The level, above which O becomes the main neutral constituent, varies with solar cycle from ~190, for solar low, to ~205 km altitude, for solar high conditions, respectively (Table 6.2). Interestingly, those altitudes stay nearly constant, irrespective of the past solar conditions. This can be understood as a result of two competing processes that control the temperature structure of the thermosphere and the middle-low atmosphere. Indeed, while a younger sun is stronger in the EUV -important at higher altitudes-, it is also weaker in the IR -important at lower altitudes- [*Gough* 1981]. This 'separation' is located around an altitude of 120 km for present conditions [*Bougher* 1999, 2000]. While a 1D study could have reached the same conclusion, a 2D simulation also shows that this transition in the thermosphere happens at higher altitudes on the dayside compared to the nightside, resulting from a more efficient dynamical day-to-night transport of O compared to heavier CO_2. Table 6.2 shows dayside maxima along with nightside minima and illustrates that this significant day-to-night difference in the dominant neutral specie may have been more important in the past due to stronger winds. For example, for solar high conditions, O becomes the main neutral constituent at ~240 and ~175 km at present, while at ~270 and ~140 km at epoch 3, for day and nightside, respectively. This result has evidently important implications for the exobase determination and is even more critical for the estimation of the yields of escaping particles over the incident sputtering flux, as presented in the work of Leblanc and Johnson (2002). As the dayside O/CO_2 ratio levels considered in this

latter study are higher than the one presented here for the past epochs (the level where $O/CO_2 = 1$ is found at ~215 km for epoch 2, and at ~200 km for epoch 3), the yields (and consequently the escape due to sputtering) might have been overestimated. Further down in the thermosphere, at 130-135 km altitude, the oxygen mixing ratio is found to be 0.90-2.10 % on the dayside (while 1.90-3.90 % on the nightside), in good agreement with the dayside average value of 1.25% of *Hanson et al.* [1977].

VI.2.3. O_2^+ distribution and ionospheric peak

As mentioned above in the study of thermospheric/ionospheric variations with solar cycle (Chapter V), the ion peak height is controlled by the underlying atmosphere, and therefore is not responsive to an increase in the EUV flux. The same altitude of about 122 km is logically computed for all three epochs, suggesting that the ion peak level may have stayed constant in the past. However, the magnitude of the ion density increases significantly with EUV, with the simulated electron density at the peak being 2.0, 3.4 and 4.7 x 10^5 cm^{-3} at the subsolar point for epochs 1, 2 and 3, respectively. Those values can be compared to the corresponding values of O_2^+ abundance given in the work of *Valeille et al.* [2009b]. The results presented here fall between theory [*Cravens et al.* 1981; *Schunk and Nagy* 2009] and observations [*Breus et al.* 2004]. The magnitude of the ion peak decreases with SZA, but the decrease is relatively more important at present than in the past by about a factor x0.4 for epoch 1 and x 0.5 for epochs 2 and 3, between 0° and 75° SZA.

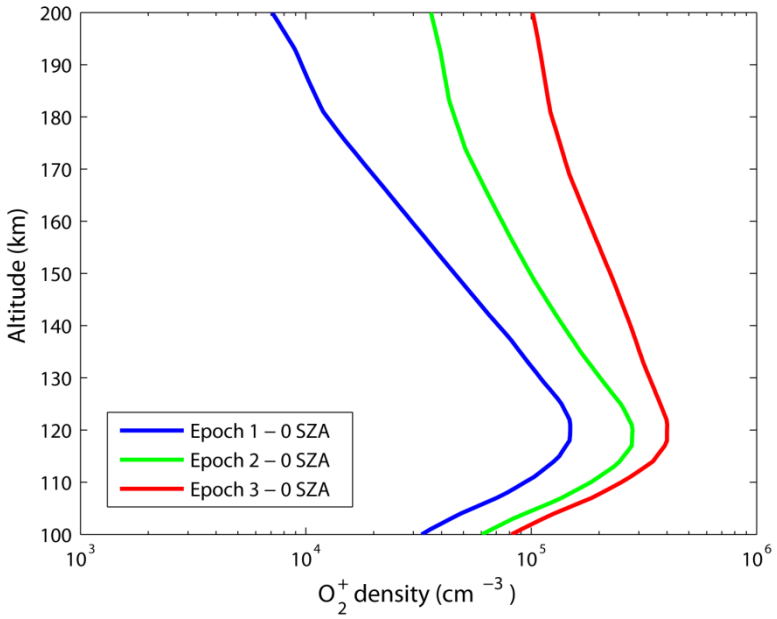

Figure 6.5. O_2^+ density profile in the Martian upper thermosphere (100 to 200 km altitude) at the Equatorial noon (0° SZA) for epoch 1, 2 and 3 (blue, green and red lines, respectively) for solar low conditions.

Figure 6.5 shows how the O_2^+ (main ion of the Martian ionosphere) density profile may have evolved in time. The magnitude of the ion peak is shown to vary with epochs and solar conditions. For solar low conditions, values are 1.5, 2.8 and 4.0 x 10^5 cm^{-3} for epoch 1, 2 and 3, respectively. For solar high conditions, values are 3.1, 4.0 and 5.0 x 10^5 cm^{-3} for epoch 1, 2 and 3, respectively. In theory, the density of the dominant ions should vary with the square root (exponent 0.5) of the solar flux [*Cravens et al.* 1981; *Schunk and Nagy* 2009]. Observations, however, indicate that the exponent is 0.37 ± 0.06 [*Breus et al.* 2004]. The results presented here fall between both. Above the 100-140 km region, higher scale heights drive the ion profiles apart. The ionospheric peak is found to be at an altitude of about 120 km at Equatorial noon (its height increases, while its magnitude decreases, with SZA in agreement with the theory and the observations). This simulated altitude is lower than Viking measurements, but major dust storm activity prior to the mission, as reported by *Martin* [1984], might have raised the ion peak at that time. This occurs because of heating inflation in the lower atmosphere, which increases the density at a constant altitude in the thermosphere [*McElroy et al.* 1977]. For all cases considered, the same altitude of about 120 km is computed, suggesting that the ion peak level may have stayed constant in the past.

VI.2.4. Exobase altitude

The average exobase level is found to be significantly higher for past solar conditions (170, 190 and 220 km altitude for epoch 1, 2 and 3, respectively). Those values are significantly less than the average 1D estimates of previous studies [*Zhang et al.* 1993b; *Lammer et al.* 2003]. This is due mostly to the inclusion of the cooling effect of the day-to-night dynamics in the current MTGCM study. In this regard, horizontal and vertical winds can be seen as a thermostat regulating the effect of the increase of the past solar EUV fluxes in the Martian thermosphere [*Valeille et al.* 2009b].

Table 6.3. Average exobase altitude (km) for the different Martian epochs for both solar minimum and maximum conditions, rounded to nearest 5 km

	Epoch 1 (~1 EUV)	Epoch 2 (~3 EUV)	Epoch 3 (~6 EUV)
Solar minimum	160	190	215
Solar maximum	175	200	225

In the Martian upper atmosphere where CO_2 and O are the two main constituents, the exobase altitude is generally defined where the collision mean free path equals the temperature scale height of the major constituent [*Schunk and Nagy* 2009]. However, Table 6.2 shows that, while CO_2 stays the major constituent until above the 'traditional' exobase altitude (~190 km) on the dayside, O is the dominant species on the nightside. In this thesis, the exobase altitude is defined as the level, above which an escaping particle moving along a radial direction will encounter one collision on average. Note that while the exobase height varies at the different epochs it stays above the ionospheric peak at all times. The SZA-averaged results are presented in Table 6.3 (with a ±20 km variation) and suggest that the exobase was significantly higher for past solar conditions. This can be mainly explained by the increase of thermospheric temperatures, as regulated by the day-to-night dynamics in the past. With higher thermospheric temperatures, the M1D thermospheric model in the study of *Zhang et al.* [1993b] found naturally higher exobase altitudes for the past epochs. The heating of the thermosphere due to the return flux of hot particles and to sputtering might also have increased the altitude of the exobase in the past [*Leblanc and Johnson* 2001]. It is interesting to compare these results (Table 6.3) with the ones of Table 6.2, as they show that the composition of the exobase changes

from a CO_2 molecule-dominated to an O atom-dominated level. This illustrates once more that on Mars the definition of the exobase should be made carefully.

VI.3. Exosphere

The 3D MTGCM calculations, for the different cases presented above, provide the respective thermospheric/ionospheric inputs for the DSMC model, which in turn gives a complete description of the hot oxygen population of the Martian exosphere. The atmospheric loss due to O_2^+ DR is calculated, as is the ion production above the ionopause, which provides a generous upper limit for ion escape. Finally, the escape due to sputtering is estimated, and those three main escape processes are compared at the different epochs, as well as are their total contributions to the water loss from the planet.

VI.3.1. O escape by O_2^+ DR

Figures 6.6a, 6.6c and 6.6e show that the spatial extent of the hot corona may have been very inflated for past epochs. At a given altitude, a uniform global enhancement of density by factors of about x5-6 and x14 is estimated between epochs 1 and 2, and epochs 1 and 3, respectively. The total escape rate (in Figures 6.6b, 6.6d and 6.6f) increases from 6.0×10^{25} s^{-1} for epoch 1, to 2.2×10^{26} s^{-1} for epoch 2, and to 5.7×10^{26} s^{-1} for epoch 3 (Table 6.4).

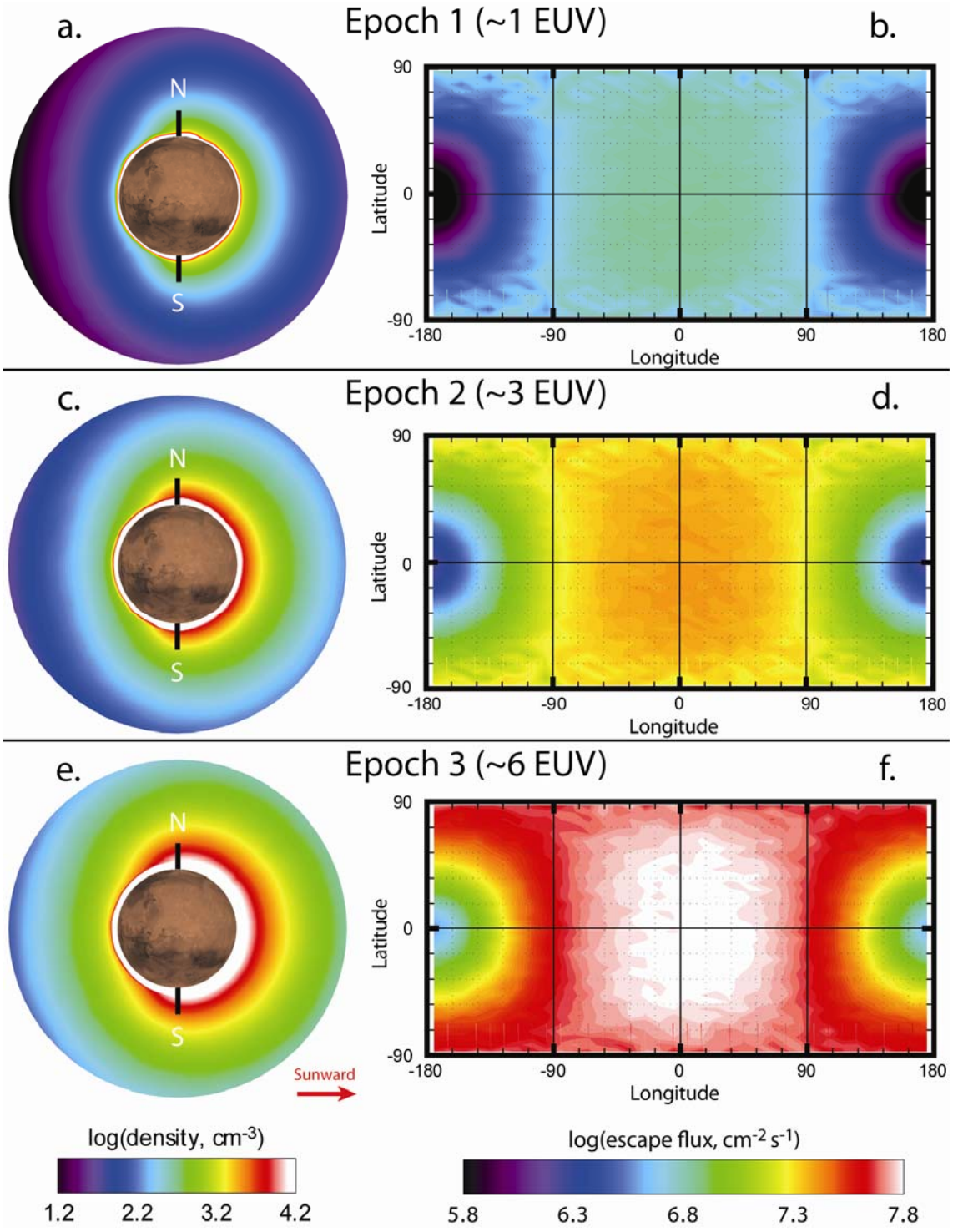

Figure 6.6. Density profiles (a, c and e) and escape fluxes at 3 Martian radii (b, d and f) of oxygen atoms at epoch 1, 2 and 3. The results are shown for the EL conditions. The same color scale is used for each panel and is consistent with that for Figures 2 and 3. The North and South Pole positions are indicated by N and S, respectively. The red arrow points toward the Sun.

Figure 6.7 gives the escape rates as functions of SZA for the different solar conditions considered at both solar low and high conditions (2D axisymmetric simulation). As already noticed earlier, where different extreme conditions were considered (Chapter V), all cases follow the same trend, decreasing by a factor of about three to four from noon to midnight at an altitude of 10 Martian radii. Furthermore, at the orbital position of equinox, the influence of the solar flux variation over the Martian history on the local atmospheric escape is found to be of a factor of about seven between epoch 1 and 3.

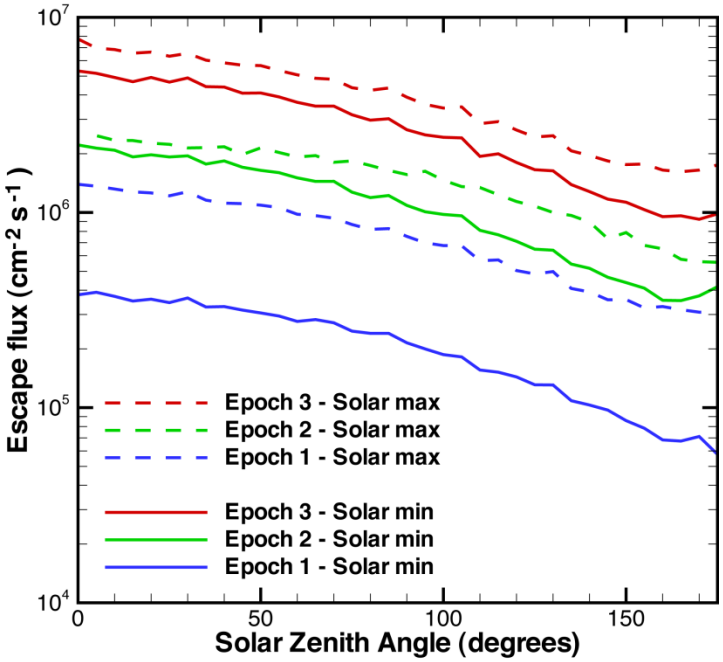

Figure 6.7. Escape fluxes of hot oxygen atoms along the Equatorial cut from 0 to 180 degrees SZA (noon to midnight, through dawn) for equinox at 10 Martian radii for epoch 1, 2 and 3 (blue, green and red lines, respectively) for both solar minimum (solid lines) and maximum (dashed lines) conditions [Source: *Valeille et al.* 2009b].

To get a broader picture of the variation of atmospheric loss with time, a comparison with the shorter-term (~22-year period) variations to this global decrease in oxygen escape rate with the Martian history is needed. Accumulating the effects of solar cycle and orbital position, the two most extreme cases illustrated by PHP (Perihelion, solar High, Polar north) and ALP (Aphelion, solar Low, Polar north) conditions in the study of *Valeille et al.* [2009a] present a difference as high as of a factor of about six. This illustrates that the long-term decrease in the escape rates (of about a factor ten) over the

last ~3.5 Gyr may be comparable to the influence of the solar activity and seasons today (of about a factor six) on a much shorter period of time.

The global escape rate due to O_2^+ DR as a function of solar flux conditions is then derived after integration over SZA and shown in Table 6.4.

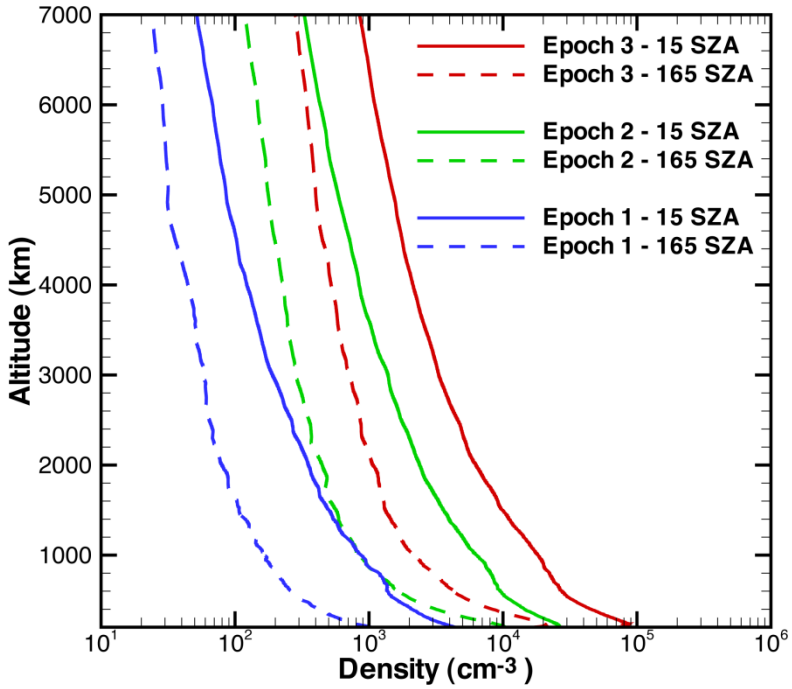

Figure 6.8. Hot oxygen density altitude profiles as a function of SZA between 200 and 7000 km (~2 planet radii) altitude, along the east Equator for solar low conditions. While results at 15 and 165° SZA (*i.e.* at 1 and 11 pm) are represented in solid and dashed line, respectively; results of epoch 1, 2, 3 are presented in blue, green, red, respectively [Source: *Valeille et al.* 2009b].

Figure 6.8 shows both influences of SZA and solar flux on the hot oxygen density altitude profiles for solar low conditions (2D axisymmetric simulation). As expected the density decreases both with time and SZA. While the day-to-night ratio in densities decreases with altitude, the difference between the epochs stays roughly constant with a factor of about 8 and 20 in densities between for epoch 1 and 2, and epoch 1 and 3, respectively.

VI.3.2. O^+ ion production

The model provides maps of the three main ionization processes, *i.e.* photoionization (PI), charge exchange (CE) and electron impact (EI). The PI frequency of f_{PI} ~2.7 and ~5.9 x 10^{-7} s^{-1} at a heliocentric distance of 1 AU [*Bailey and Sellek* 1990] is adjusted for the heliocentric distance of Mars equinox to f_{PI} ~1.2 and ~2.5 x 10^{-7} s^{-1}, for solar low and high conditions, respectively. The proportionality of these rates with solar EUV fluxes is assumed.

CE and EI are solar wind driven processes. As O^+ ions escape is believed to be small compared to the neutral O atoms, and because the solar wind interaction with the Martian atmosphere at past epochs is roughly estimated, generous estimates are used to evaluate the ion production due to those processes.

The present estimated positions of the ionopause and bow shock [*Zhang et al.* 1993a; *Leblanc and Johnson* 2001; *Trotignon et al.* 2006] are used for each case. In the region between the ionopause and the bow shock, the solar wind velocity and density are estimated to be 0.25 and 4 times their respective values above the bow shock in each case. Also in this region, since the solar wind electrons are most strongly heated at the subsolar bow shock, the electron temperature is taken to be constant and equal to its maximum value at the nose. Finally, the solar wind density n_{SW} and velocity v_{SW} are taken to be equal to n_{SW} ~2.5, ~8.0, ~40 cm^{-3} and v_{SW} ~400, ~480, ~700 km s^{-1} for epoch 1, 2, 3, respectively [*Newkirk* 1980; *Lammer et al.* 2003]. Due to the large estimated uncertainty in the fit for n_{SW}, solar wind density is taken for average mass loss rates [*Selsis et al.* 2002; *Guinan and Ribas* 2002] and these parameters are considered independent of the solar activity.

The CE frequency f_{CE} can be defined as $f_{CE} = n_{SW} v_{SW} \sigma$, where $\sigma = 8 \times 10^{-16}$ cm^2 is the cross section for CE with atomic oxygen [*Stebbings et al.* 1964].

The EI frequency f_{EI} can be defined as $f_{EI} = n_{SW} \nu(T_e)$, where $\nu(T_e)$ is the ionization frequency per incident electron as a function of electron temperature [*Cravens et al.* 1987]. The lack of observational data at Mars makes it difficult to estimate ion and electron temperatures both at present and in the past. To provide solar variation, the scheme adopted by *Fox et al.* [1996, also private communication 2008] is used, for which values of electron and ion temperatures are guided by Viking measurements, but tied to

neutral temperature. For T_e ~2 x 10^5 and ~2 x 10^6 K above and under the bow shock, $\nu(T_e)$ is taken to be $\nu(T_e) \sim 2 \times 10^{-8}$ and $\nu(T_e) \sim 8 \times 10^{-8}$ cm^3 s^{-1}, respectively.

The simulated total ionization rate in the Martian ionosphere after summation of the three main ionization contributions is presented in Table 6.4. For present conditions, integration gives a total O^+ ion production of 2.2 x 10^{24} s^{-1}, and 1.0 x 10^{25} s^{-1} for the EL case and the EH case respectively, in good agreement with the recent study of *Chaufray et al.* [2007] (1.9 x 10^{24} s^{-1} and 9.4 x 10^{24} s^{-1}, respectively), which used the hybrid model of *Modolo et al.* [2005]. Under the generous assumption that all ions produced above 300 km escape [*Zhang et al.* 1993b], the computed O^+ ion loss would then be in excellent agreement with the respective values for EL and EH for present conditions of ~2.4 x 10^{24} s^{-1} and ~1.0 x 10^{25} s^{-1} based on data obtained with new energy settings for ASPERA-3 ion mass analyser (IMA) on MEX reported in the recent study of *Lundin et al.* [2008]. In this study, both relative contributions of cold and hot oxygen particles can be considered, and they are shown comparable for each ion production process (see Chapter IV).

Table 6.4. Neutral oxygen escape and O^+ ion production rates (s^{-1}) for epoch 1, 2 and 3

	Epoch 1 (~1 EUV)		Epoch 2 (~3 EUV)		Epoch 3 (~6 EUV)	
	solar Low	solar High	solar Low	solar High	solar Low	solar High
O escape by DR	6.0 x 10^{25}	1.9 x 10^{26}	2.2 x 10^{26}		5.7 x 10^{26}	
O^+ production	2.2 x 10^{24}	1.0 x 10^{25}	3.8 x 10^{25}		3.5 x 10^{26}	

The ion production appears to increase more dramatically (about a factor x160) with higher EUV radiation in the past, from 2.2 x 10^{24} s^{-1} for epoch 1 to 3.5 x 10^{26} s^{-1} for epoch 3. However, even though the O_2^+ DR contribution to the total oxygen escape might have been smaller in the past compared to the present secondary processes, integration over time shows that it is still the most important process in loss of water over the Martian history [*Valeille et al.* 2009b]. It should be noted that this important result differs from the conclusion reached by the only other exospheric simulation in the literature [*Zhang et al.* 1993b], which suggested that ion loss might have been the most important process in loss of water over the same period.

VI.3.3. O escape by Sputtering

Escape due to sputtering by pickup ions and its evolution over the Martian history is still relatively poorly known and the only estimation in the literature today comes from the combination of the results of two studies. The first, by *Johnson and Luhmann* [1998], estimates the intensity of the flux of impacting ions into the Martian atmosphere, while the second, by *Leblanc and Johnson* [2002], calculates sputtering yields (efficiency of impacting ions for ejecting neutral atmospheric particles). The estimate of the escape rate associated with sputtering, deduced from those two studies, was generally accepted and used by other works in their discussion about the atmospheric evolution of Mars [*e.g. Lammer et al.* 2003, *Chassefière et al.* 2007].

In the study by *Leblanc and Johnson* [2002], the O/CO_2 ratio at the exobase was used to deduce the sputtering yields. In the study by *Johnson and Luhmann* [1998], the production of O^+ ions in the ionosphere was used to deduce the impacting flux. Those two critical inputs were taken from the M1D thermosphere presented in the 1D study of *Zhang et al.* [1993b].

However, improvements made in the thermosphere model (from the M1D to the MTGCM) lead to significant differences, especially in exospheric temperatures, exobase height and atmospheric composition. Both the dayside profile of O/CO_2 ratio and exobase height from Figure 4 in the study of *Leblanc and Johnson* [2002] are above the ones presented in Tables 6.2 and 6.3 of this study, and therefore the resulting yields might have been overestimated. This point would be consistent with the smaller yields deduced from the recent study of *Chaufray et al.* [2007] for present conditions. To an even greater extent, ionospheric production of O^+ ions from the 1D study of *Zhang et al.* [1993b] is far higher than the one presented here, or compared to the study of *Chaufray et al.* [2007] for present conditions. This probably led to an overestimation of the impacting flux in the study of *Johnson and Luhmann* [1998], and -together with the yield- to an overestimation of the escape due to sputtering and of its importance in the past.

Another way of estimating the sputtering contribution in the total escape is therefore needed in order to maintain consistency with the description of the thermosphere given in the first part of this chapter. To first order, if sputtering is assumed to be mostly dependent on the EUV variations [*Chassefière et al.* 2007], then results for solar low and

high for modern conditions could be extrapolated for past conditions. Applying the above observation that the difference in the solar fluxes between solar low and high activities is a factor of about two in the EUV if imposed on the results of the study of *Chaufray et al.* [2007], the escape due to sputtering can be estimated for epochs 2 and 3 and is presented in Table 6.5. This method presents the additional advantage of providing an estimate for solar high conditions in the past. The assumptions remain however rather uncertain, and the results presented here shall be used qualitatively (rather than quantitatively). It should underline the necessity of having a new self-consistent study of the subject, coupling not only thermosphere and neutral exosphere (as done in this study), but also ionosphere and the solar wind interaction. Such a study is however well beyond the scope of this work, so these qualitative estimates of what the sputtering would have been in the past will be used here to compare with other escape processes.

The conclusions reached here are quite different from the combined results of the two studies of *Johnson and Luhmann* [1998] and *Leblanc and Johnson* [2002], as the slope of evolution of sputtering with time is much smaller (~2 is estimated here compared to ~7 in *Chassefière et al.* [2007]). However, the fact that this slope is closer to the one of the O^+ production looks more reasonable, as both quantities should behave similarly (the impacting flux comes from the O^+ produced in the ionosphere, and therefore both quantities should follow a similar trend in their evolution, *i.e.* a similar slope on Figure 6.9). It is also important to note that even if the more generous results from past studies [*Leblanc and Johnson* 2002; *Cipriani et al.* 2007] are considered, the conclusion (at least in term of loss of water) would remain the same. Indeed, even if the escape rate due to sputtering would have become more important than the one related to O_2^+ DR, it would have been only very far in the past, and the integration in term of water depth would have shown that more water was lost due to O_2^+ DR escape than sputtering escape.

VI.3.4. Discussion

Interestingly, from the results of epoch 1 on Table 6.5, an approximately 11-year solar cycle average hot oxygen escape rate of about ~9.0 x 10^{25} s^{-1} can be estimated. And if the thermal loss of hydrogen at present is roughly estimated by Jeans Escape to be

about ~1.9 x 10^{26} s^{-1} - almost independent of solar activity - by the recent studies of *Krasnopolsky* [2002] and *Lammer et al.* [2003] (although *Zahnle et al.* [2008] computed a higher flux), then the 2:1 ratio between H to O loss would be nearly entirely fulfilled by O_2^+ DR loss process only. Because the study of *Lammer et al.* [2003] used for O escape due to O_2^+ DR the underestimated value of *Kim et al.* [1998] corrected by the later work of *Nagy et al.* [2001], its H to O loss ratio might have been overestimated and other processes were suggested to account for the missing oxygen (needed for the validation of the 2:1 ratio). The results presented here suggest that, at least at the present epoch and for steady-state modern conditions, most H_2O escapes to space stochiometrically (thermally for hydrogen and by O_2^+ DR for oxygen). However, the important increase in thermospheric temperatures in the past (as previously shown in Figures 6.2 and 6.3) suggests a faster increase in the thermal escape of hydrogen compared to the escape of oxygen due to O_2^+ DR in the past (as Jeans thermal escape rate is very temperature dependent, whereas O_2^+ DR is not). Therefore a better understanding of the hydrogen escape and its evolution might show that oxygen sinks other than escape to space, such as chemical weathering of the surface soil [*Lammer et al.* 2003; *Zahnle et al.* 2008], formation of carbonates, CO_2 ice in the regolith or polar caps [*Haberle* 1998], might have been relatively more important in the past.

Also, from the results of epoch 3 on Table 6.5, an average oxygen escape rate due to O_2^+ DR of about ~5.9 x 10^{26} s^{-1} can be estimated. It can therefore be deduced that the decrease with time in oxygen escape rate due to O_2^+ over the last ~3.5 Gyr is about a factor seven. The study of *Valeille et al.* [2009a] estimated the ~22-year periodic variations in the oxygen escape rate, due to the cumulative effect of solar cycle and orbital position, to be a factor of about six, for present conditions. Therefore the long-term decay of atmospheric loss due to O_2^+ DR throughout the Martian history may be comparable to the short-term periodic variations at present. This illustrates the need of studying both solar low and high conditions (or at least an average) when estimating any EUV dependent process in the Early Mars.

Table 6.5. Neutral oxygen escape and O^+ ion production rates (s^{-1})

	Epoch 1 (~1 EUV)		Epoch 2 (~3 EUV)		Epoch 3 (~6 EUV)	
	Solar min	Solar max	Solar min	Solar max	Solar min	Solar max
O escape by DR (present study)[a]	3.8×10^{25}	1.3×10^{26}	2.0×10^{26}	2.6×10^{26}	4.9×10^{26}	6.9×10^{26}
O escape by Sputtering (Chaufray et al. 07)[b]	2.0×10^{23}	7.0×10^{23}	(1.5×10^{24})	(5.2×10^{24})	(5.2×10^{24})	(1.3×10^{25})
O escape by Sputtering (Leblanc et al. 02)	3.4×10^{23}		1.3×10^{26}		1.7×10^{27}	
O^+ production (present study)	1.5×10^{24}	7.4×10^{24}	2.7×10^{25}	1.2×10^{26}	4.0×10^{26}	4.0×10^{26}
O^+ production (Chaufray et al. 07)[b]	1.9×10^{24}	9.4×10^{24}	(2.4×10^{25})	(1.2×10^{26})	(1.2×10^{26})	(3.9×10^{26})
O^+ production (Lammer et al. 03)[c]	3.0×10^{24}		4.0×10^{25}		8.3×10^{26}	

[a] more detailed results regarding present conditions (epoch 1) and a comparison with models of the last ten years are presented in the study of *Valeille et al.* [2009a].
[b] extrapolations of the results at present conditions were made for epoch 2 and 3 (shown in parenthesis).
[c] those values are ion escape rates rather than ion production.

The results of these calculations suggest the following heuristic scaling law for evolution of the rate, ω, of each of those processes (*i.e.* escape by DR, escape by sputtering and ion production), with respect to the EUV flux:

$$\omega(\chi)/\omega_p = \chi^{\alpha} \tag{6.1}$$

where, for a given solar activity, ω_p is the present rate. (For example, ω_p is 3.8×10^{25} and 1.3×10^{26} s^{-1} for solar low and high respectively for escape by DR). $\chi = \phi/\phi_p$ is the relative solar EUV flux with respect to the present value (in other words: 1, 3, 5 or 6). The linear regression shown in Figure 6.9 gives a coefficient α of ~1.4, ~1.8 and ~3.0 for escape by DR, escape by sputtering and ion production, respectively.

As mentioned above, a model of the evolving EUV luminosity [*Ribas et al.* 2005] is used as a guide in adjusting conditions to represent the past. The following power law expression is deduced from the resultant relative fluxes with very high correlation by *Lammer* [2003]:

$$\chi(t) = \left(t/t_p\right)^{-\beta} \tag{6.2}$$

where t is time (so t_p is ~4.6 Gyr) and χ(t) is the relative solar EUV flux with respect to the present value. The coefficient β is taken to be 1.19, as in the studies of *Lammer et al.* [2003] and assumed independent of solar conditions, whereas *Ribas et al.* [2005] and *Chassefière et al.* [2007] chose t_p = 4.7 Gyr and β = 1.23. This relation indicates that the solar EUV flux ~2.5 and ~3.5 Gyr ago was about 3 and 6 times higher, respectively, than

today. *Zhang et al.* [1993b] derived a very similar law (with β = 1.33) from *Zahnle and Walker* [1982], which also was used by *Hodges* [2002] to evaluate the escape by DR.

Combining equations (1) and (2) gives an estimate of the evolution of oxygen escape rate ω with time:

$$\omega(t)/\omega_p = \left(t/t_p\right)^{-\gamma} \tag{6.3}$$

with γ = αβ. Owing to the continual decay of the solar EUV flux, oxygen escape and water loss have diminished with time roughly as $t^{-\gamma}$, with γ of ~1.7, ~2.1 and ~3.6 for escape by DR, escape by sputtering and ion production, respectively.

These results are plotted in Figure 6.9 for each process and for both solar low and high conditions. All processes were more important in the past, but as their effects increase with different γ slopes with solar EUV inputs, their relative contributions change between present and past conditions. It can be seen that, as DR is by far (more than an order of magnitude) the main escape mechanism at present, its relative contribution is reduced in the past, and becomes comparable to ion production at epoch 3 (~6 EUV).

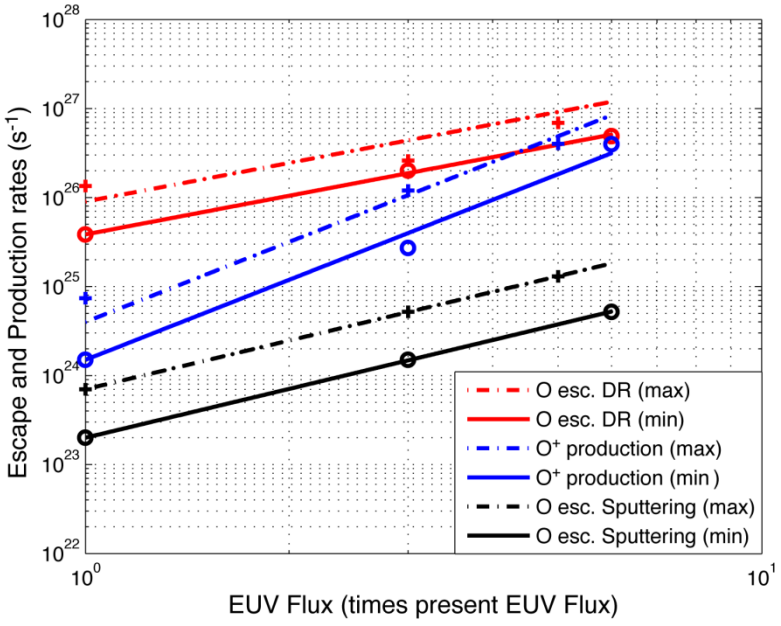

Figure 6.9. Linear regression of neutral O escape rate due to DR (red lines), due to sputtering (black line) and O^+ ions production rate (blue lines) versus EUV flux of epochs 1, 2 and 3 for solar minimum (solid lines) and maximum (dashed-dotted lines) conditions.

Finally, integration over time of the above equation (6.3) gives the estimate of the total amount of water loss, expressed as global average water depth, under the hypothesis that each O atom corresponds to a destruction of molecule of liquid water [Hodges 2000].

$$\Delta(t) = \frac{M}{4\pi R^2 \rho N_A (1-\gamma)} \omega_p t_p^{\gamma} \left(t_p^{1-\gamma} - t^{1-\gamma} \right) \qquad (6.4)$$

where M is the molar mass of water (~18 g mol^{-1}), ρ its density (~1.0 g cm^{-3} at 20 ºC in liquid state), R the radius of Mars (~3,400 km), and N_A the Avogadro number (~6.0 x 10^{23} mol^{-1}). This function is plotted in Figure 6.10, and the relative contribution of water loss of those main three escape mechanisms is shown. It is assumed here that all ions, produced above the ionopause, escape. This is a very generous estimate, as studies have shown that only a ratio of 10 to 35% of ion produced actually escape [*Fang et al.* 2008a; *Chaufray et al.* 2007]. It should also be noted that the Martian crustal magnetic anomalies, which were likely to have played a more important role in the past, were shown to lead to a significant shielding (decrease of about of a factor 2) in the ion loss process at present [*Fang et al.* 2008b]. This effect would have been certainly more extended in the presence of a magnetosphere before -3.6 Gyr ago, but is not considered in the graphs of Figure 6.10.

Even though the O_2^+ DR contribution to the total oxygen escape might have been smaller in the past compared to the present secondary processes, integration over time (equation 6.4) shows that it is the most important process in loss of water over the Martian history (Figure 6.10).

Solar low and high cases are considered in this study to provide lower and upper limits of the water loss. Studies on evolution of solar X-rays, UV [*Guinan and Ribas* 2002], and of ionization rates of neutrals from the top of the atmosphere [*Quémerais et al.* 2006] suggest that the solar cycle can be approximated as a step-like function over time, equally divided for low and high conditions. It may then be legitimate to take the atmospheric escape over the time as the average of the two extreme solar conditions. With this assumption, the global average depth of water can be evaluated to be about 10 m over the period from 1 Gyr to the present. While influx of water by cometary impacts [*Grinspoon and Lewis* 1988] after that time (of about ~0.5 m of water) cannot affect our conclusions, hydrodynamic escape of H_2 formed in the reaction between H_2O and metallic iron could have led to much more water loss in the past [*Krasnopolsky* 2002].

Even if the estimate of water loss before that time is very rough, it appears that the bulk of water escape on Mars may have happened in the first ~0.5-1 Gyr of its history, consistent with atmospheric models about this period [*Tian et al.* 2009, also private communication 2009]. This is also in good agreement with the work of *Donahue* [1995], who calculated water escape rates based on the D/H ratio of the Zagami SNC meteorite considered to be of Martian origin. From Figure 6.10, a qualitative (rather than quantitative) estimation of ~100 m of liquid water might have been lost to space during that period, confirming the geomorphic arguments [*Carr* 1996, 1999; *Solomon et al.* 2005] of the existence of a large quantity of water on the surface of Mars during that early epoch.

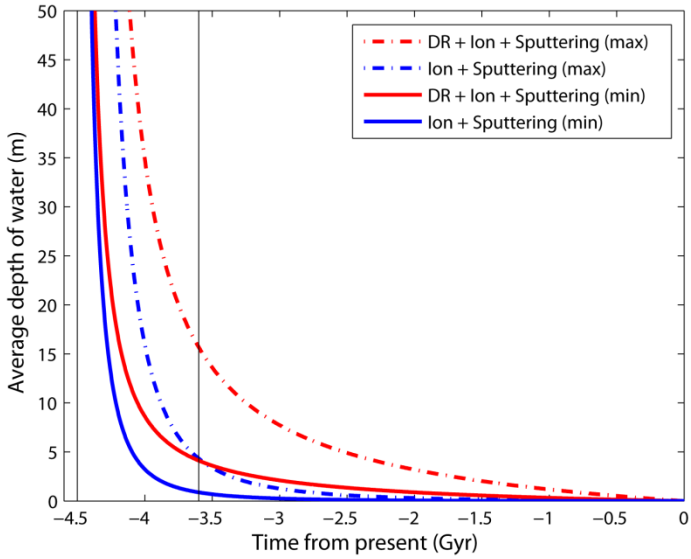

Figure 6.10. Cumulative water loss due to sputtering, ion loss (blue lines) and DR (red lines) for solar minimum (solid lines) and maximum (dashed-dotted lines) conditions. Sputtering before -3.6 Gyr ago is not shown as the presence of a magnetosphere at that time would have protected the planet from its effect. In the first 0.1 Gyr, the atmospheric composition is believed to be far different from the present CO_2 dominated one.

Chapter VII
Complementary studies

The main focus of the thesis is to provide a 3D description of the Martian hot atomic oxygen corona originating from O_2^+ DR for different limiting conditions both in the present and in the past. In this section, the impact of secondary and tertiary sources on the atmospheric loss of hot atomic oxygen is discussed in more detail, together with the escape of other species: hot atomic carbon and hydrogen. Indeed, to a lesser extent, atomic species other than oxygen constitute coronae by themselves. Most processes involved are different from the hot oxygen sources but fairly similar in nature.

Quantitative estimates of the magnitude of these processes are taken from the literature (mostly 1D exospheric/ionospheric studies). Orbital and solar conditions are fixed and correspond to the EL case (see Chapter IV). All these mechanisms can (and certainly should) be simulated by a 3D self-consistent coupling between a thermosphere/ionosphere and an exosphere model. Preliminary results computed by our MTGCM/DSMC model are provided for illustration.

As mentioned in Chapter II, the mechanisms for escape to space can be divided initially into two parts: thermal and nonthermal. The thermal escape or Jeans escape [*Chamberlain and Hunten* 1987] is important for the light atmospheric constituents, such as hydrogen and helium, whereas nonthermal escape processes dominate the escape of the heavier constituents, such as oxygen, carbon and nitrogen [*Chassefière and Leblanc* 2004].

In general, six important nonthermal processes could be or could have been important in the history of the heavy species escape since the end of the Martian dynamo (*i.e.* ~3.5

Gyr ago): (1) dissociative recombination (DR) of molecular ions, (2) acceleration of exospheric pickup ions by the solar wind, (3) charge exchange (CE) of these pickup ions leading to an oxygen energetic neutral atoms (ENA) escape, (4) sputtering of the atmosphere by reimpacting pickup ions, (5) ionospheric outflow and, in the case of nitrogen and carbon escape, (6) molecular photodissociation [*Lammer et al.* 2003; *Chassefière and Leblanc* 2004; *Chassefière et al.* 2006].

VII.1. Secondary source processes for hot O

As demonstrated in Chapters III and VI, O_2^+ DR is the main source of hot atomic oxygen today and probably also in the past as far as about 3.5 Gyr ago. During this period, thermospheric temperatures were not high enough for thermal production of hot atomic oxygen to be significant, even compared to secondary processes and can therefore be considered only as playing a tertiary role. Unlike O_2^+ DR production, which comes mostly (~80%) from below the exobase ('thermospheric escape process' in Figure 7.1), secondary source processes come (directly or indirectly) from the interaction of the solar wind with Mars hot corona ('ionospheric escape processes' in Figure 7.1).

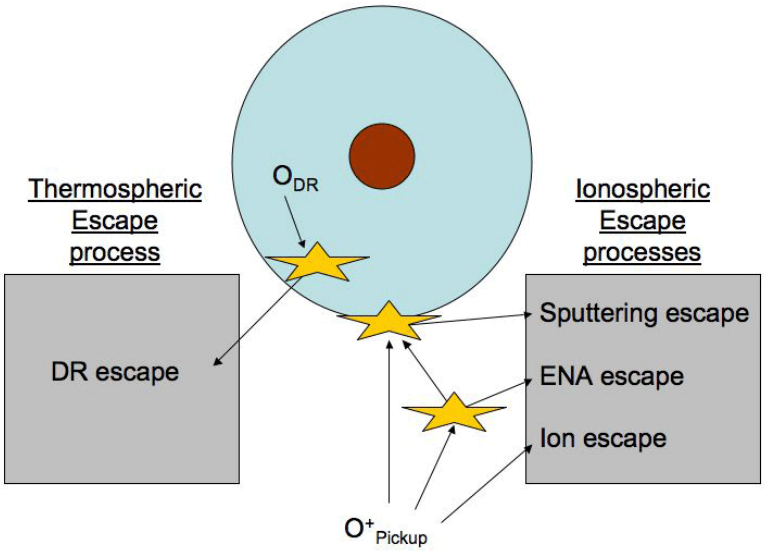

Figure 7.1. The two most important groups of oxygen escape mechanisms on Mars: DR of thermospheric O_2^+ ions and processes due to ionospheric O^+ pickup ions precipitation (more specifically: ions, sputtering and ENA escape processes).

VII.1.1. Ion escape

The neutral exospheric population can be ionized by EUV solar photons, solar wind electron impacts and charge exchange with the solar wind or planetary ions. Evidence for charge exchange between solar wind heavy ions and exospheric neutrals is the discovery of an X-ray halo within 3 Mars radii [*Dennerl et al.* 2006] and detection of ENAs by ASPERA-3 [*Barabash and Lundin* 2006] on Mars Express [*Gunell et al.* 2006; *Brinkfeldt et al.* 2006]. Electronic impact ionization has been detected near the Magnetic Pileup Boundary by the Mars Global Surveyor observations [*Crider et al.* 2000]. A fraction of these newly created ions can be picked up by the solar wind electric field and escape. This escape flux has been measured by the Phobos 2 mission [*Lundin et al.* 1989; *Verigin et al.* 1991] and more recently by ASPERA-3 on Mars Express [*Lundin et al.* 2006, 2008; *Carlsson et al.* 2006; *Kallio et al.* 2006; *Barabash et al.* 2007]. The escape flux associated with this process has been estimated using a number of models: gas dynamic model [*Zhang et al.* 1993b], 3D Magneto-Hydrodynamic (MHD) models [*Ma et al.* 2004; *Harnett and Winglee* 2005] and 3D Hybrid models [*Kallio and Janhunen* 2002; *Modolo et al.* 2005] (see also the review by *Nagy et al.* [2004] of the different mechanisms of interactions between the solar wind and the Martian atmosphere).

VII.1.2. Escape due to charge exchange (ENA escape)

A fraction of the pickup ions can be neutralized in the exosphere leading to the formation of ENAs which can escape giving a third nonthermal escape mechanism.

The two charge exchange reactions as sources for hot atomic oxygen are [*Schunk and Nagy* 2009],

$$O_{hot}^{+} + O \rightarrow O^{+} + O_{hot} \quad (7.1)$$

$$O_{hot}^{+} + H \rightarrow H^{+} + O_{hot} \quad (7.2)$$

This process involves both ions and neutrals and therefore requires a model that could couple both ionosphere and exosphere descriptions.

VII.1.3. Escape due to sputtering

A fraction of the pickup ions and ENAs can reimpact the atmosphere. These reimpacting populations can collide with the neutral atmospheric particles and produce recoils with enough energy to escape or to populate the Martian corona. This process, called atmospheric sputtering by pickup ions [*Johnson* 1990], was applied to Mars for the first time by *Luhmann and Kozyra* [1991] using a test particle approach, then using more realistic cross sections in an analytic model [*Luhmann et al.* 1992]. Subsequently, 1D or 3D Monte Carlo simulations were carried out [*Kass and Yung* 1995, 1996; *Johnson and Liu* 1996; *Leblanc and Johnson* 2001, 2002; *Cipriani et al.* 2007]. Chapter VI shows that for the total production of nonthermal O escape, pickup ion sputtering is much smaller than loss due to O_2^+ DR for modern conditions. However, it also shows that the sputtering process could have been the most important source of oxygen escape in the past [*Luhmann et al.* 1992; *Luhmann* 1997; *Leblanc and Johnson* 2002; *Valeille et al.* 2009b]. Note that all the past calculations were based on studies by *Luhmann et al.* [1992], who derived the reimpacting flux of accelerated O^+ picked up ions at different epochs of Mars history using a gas dynamic approach.

Table 7.1. Comparison of escape fluxes (s^{-1}) of hot atomic oxygen due to sputtering from different studies

	solar Low activity	solar High activity
Chaufray et al. 2007	2.0×10^{23}	7.1×10^{23}
Cipriani et al. 2007	4.9×10^{23}	3.7×10^{25}
Leblanc and Johnson 2002	3.4×10^{23}	4.1×10^{25}
Luhmann et al. 1992	3.0×10^{23}	

VII.1.4. Discussion: exosphere/ionosphere coupling

All these secondary hot atomic oxygen mechanisms involve both ions and neutrals and therefore requires a model that could couple both ionosphere and exosphere descriptions. By using a combination of 3D exospheric Monte Carlo model and 3D Hybrid code [*Modolo et al.* 2005], the work of *Chaufray et al.* [2007] describes far more accurately the interaction of the solar wind with Mars upper atmosphere than previous

studies and shows that the atmospheric escape due to sputtering is negligible compared to DR whereas earlier studies did not reach a clear conclusion. However the 1D thermospheric inputs lead to an important limitation on the results. Results of escape rates of hot atomic oxygen due to sputtering from different studies are compared in Table 7.1.

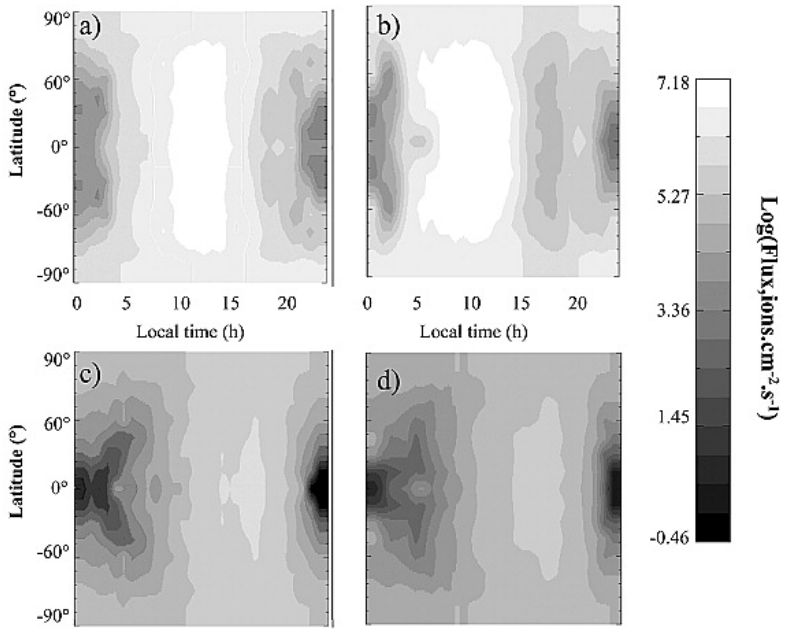

Figure 7.2. Spatial distributions of the precipitating flux at an altitude of 300 km above the Martian surface. The top row represents the distribution for the low-energy incident particles for (a) a period of low solar activity and (b) a period of high solar activity, and the bottom row displays the distribution for the high-energy incident particles for (c) a period of low solar activity and (d) a period of high solar activity. The symmetry about the Equator has been imposed. [Source: *Chaufray et al.* 2007].

O^+ ion production and electromagnetic fields, exospheric parameters resulting from the interaction of the solar wind with the Martian neutral upper atmosphere, are first calculated by a Mars 3D Hybrid model, solving motional and Maxwell equations and describing electrons as a massless fluid and ions as particles. Along with the self-consistent description of the ionization of the Martian corona by electron impact, charge exchange and photoionization, the Mars 3D Hybrid model includes the description of finite gyroradius, which is partially responsible for the asymmetry of the plasma in the vicinity of the planet. Hybrid approaches are very relevant in the case of the Martian ionosphere where the ion gyroradius is of the same scale as the size of the interaction

regions. However, the main limitation of the model is its spatial resolution (300 km x 300 km x 300 km), especially in the vicinity of the planet, where the exobase altitude is only 200 km. An MHD approach would have solved this problem but also brought some other limitations (even with considering the Hall effect). Results of the two approaches are compared in the study of *Ma and Nagy* [2007]. Hybrid approach is well adapted to describe the escape coming from pickup ions, while MHD describe the ionospheric outflow with better accuracy.

The ion escape rate and the distribution of the O^+ and ENA precipitating fluxes at 300 km (Figure 7.2) are then calculated by a test particle simulation, using standard charged particle equations of motion. This step was taken for simplicity and computational sake. However for better consistency it would have been possible to treat the ion particle as a different specie whose motion is influenced by the locally fixed electromagnetic fields in a DSMC code.

Sputtering and ENA escape rates and their contributions to the Martian corona are finally estimated by 3D Monte Carlo simulation. The resulting exospheric densities are shown in Figure 7.3. The study of *Chaufray et al.* [2007] did not justify why no iteration with the Hybrid code was considered. However, as the sputtering contribution accounts for only 10% of the total escape, it can be inferred that iteration with the Hybrid model will only lead to a minor correction.

A similar approach could be followed by using the present study in combination with a detailed ion pickup precipitation model, such as the one described in *Fang et al.* [2008a, 2008b].

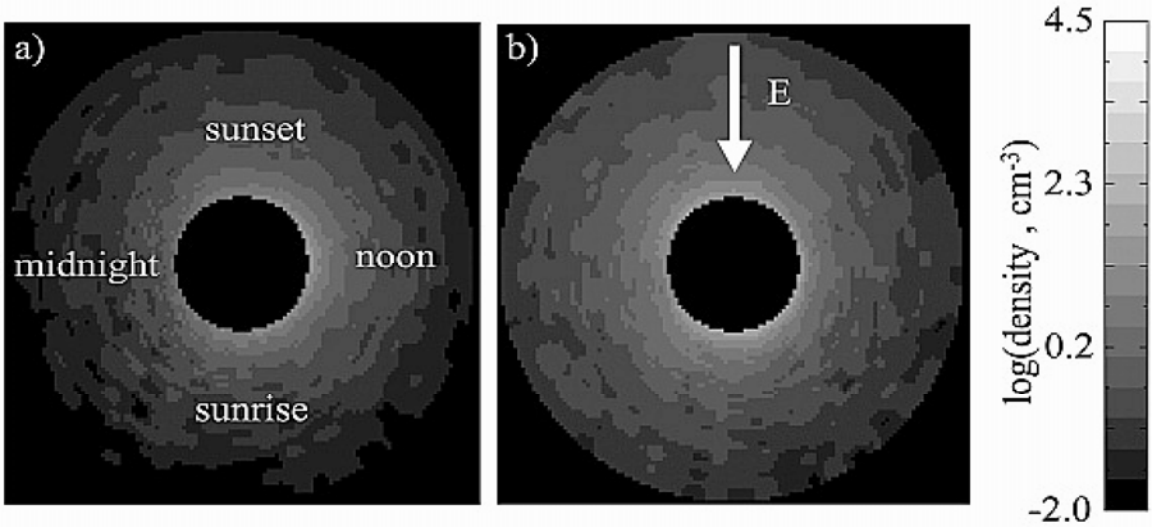

Figure 7.3. Hot oxygen density due to the sputtering for (a) low and (b) high solar conditions in the Equatorial plane (the grey scale is in $\log_{10}$ of cm^{-3}). The dayside is on the right, and the nightside is on the left. Contributions of the sputtering due to low- and high-energy particles have been added. [Source: *Chaufray et al.* 2007].

Finally, this discussion shows the necessity of using a self-consistent 3D model including both 3D thermospheric and ionospheric inputs to get a complete description of the oxygen corona on Mars and its interaction with the solar wind. The preliminary results of the density distribution of escaping oxygen atoms due to sputtering for the EL case are presented in Figure 7.4a. To simulate the sputtering process, a homogeneous planar (in the Sun-Mars direction) impacting flux of 5×10^5 cm^{-2} s^{-1} of 1eV oxygen atoms is taken from the study of *Johnson and Luhmann* [1998]. It can be compared to other studies and the results of the DSMC density distribution of escaping oxygen atoms due to O_2^+ DR for the EL case, presented in Figure 7.4b.

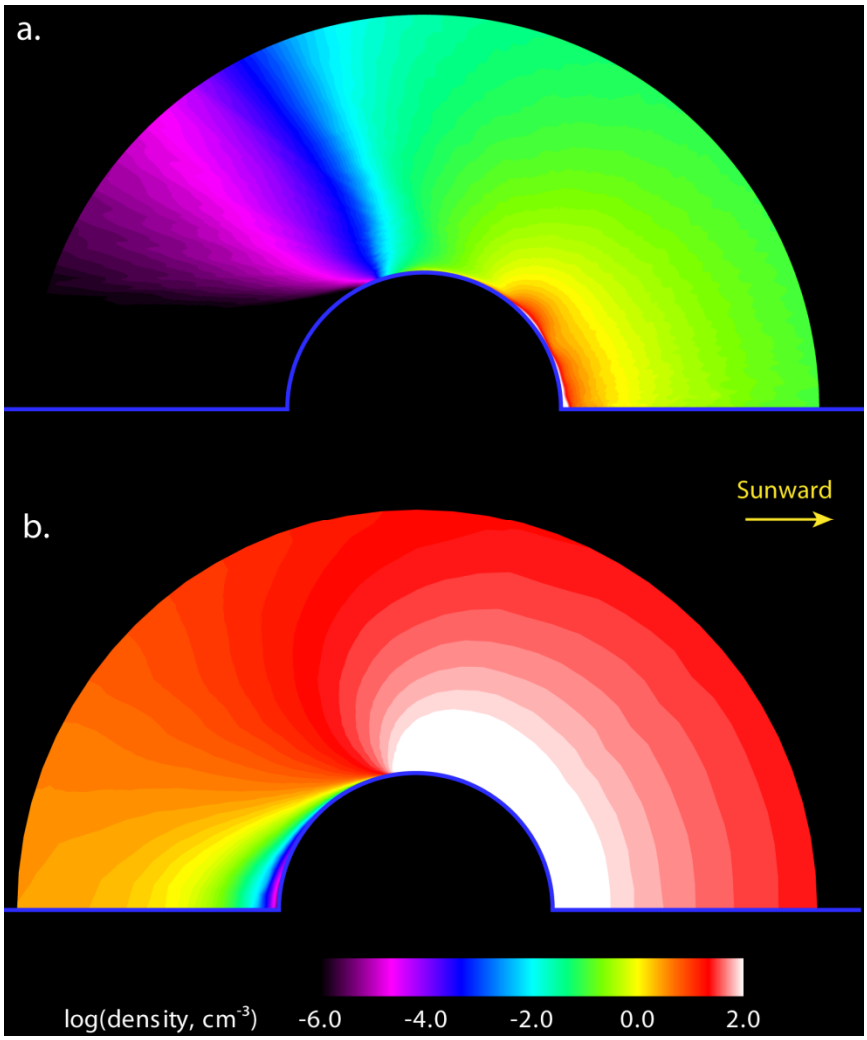

Figure 7.4. Density distribution of escaping oxygen atoms due to sputtering (a) and due to O_2^+ DR (b) for the EL case. The same color scale is used for each panel. The yellow arrow points toward the Sun.

VII.1.5. Ionospheric outflow

Another nonthermal escape process is the ionospheric outflow observed by ASPERA on Phobos 2 at high solar activity [*Lundin et al.* 1989] and more recently by ASPERA 3 on Mars Express at low solar activity [*Lundin and Barabash* 2004; *Dubinin et al.* 2006; *Carlsson et al.* 2006; *Barabash et al.* 2007; *Lundin et al.* 2008]. Such a mechanism is favored when the solar wind penetrates below the Martian ionopause [*Kar et al.* 1996; *Fox* 1997] as reported by *Lundin and Barabash* [2004]. This process has been studied recently by *Ma et al.* [2004] and *Ma and Nagy* [2007] using a 3D MHD model of the

solar wind interaction with Mars. Ionospheric outflows may be responsible for the escape of ionospheric O^+, O_2^+ and CO_2^+ ions as observed by ASPERA-3, but apparently in a less intense way than predicted [*Carlsson et al.* 2006].

VII.2. Carbon

The escape of the atomic carbon plays an important role in the CO_2 planetary inventory. The main expected photochemical escape sources are CO^+ DR reactions [*Cipriani et al.* 2007], photodissociation of CO, and electron impact dissociation (EI) of CO [*Fox* 2004]. CO_2^+ DR is also responsible for the major part of the thermospheric density of atomic carbon.

VII.2.1. CO^+ DR

In the study of *Cipriani et al.* [2007], escape rates and densities are calculated only for hot carbon created by CO^+ DR. Although this is not the major escape source for hot atomic carbon, this source of hot C atoms can interestingly be compared to the carbon loss induced by sputtering. The excess energies (in square brackets) and the measured branching ratios (in parentheses) of *Rosen et al.* [1998] are used for the main branches of the CO^+ DR reaction:

$$CO^+ + e \rightarrow \begin{cases} C(^3P) + O(^3P) + [2.90eV] & (0.76-0.53) \\ C(^1D) + O(^3P) + [1.64eV] & (0.15-0.34) \\ C(^3P) + O(^1D) + [0.94eV] & (0.09-0.08) \\ C(^1D) + O(^1D) + [0.33eV] & (0.00-0.05) \end{cases} \quad (7.3)$$

The corresponding branching ratios are, respectively, 0.761, 0.145, and 0.094 at 0 eV relative energy (in this case, the fourth endothermic channel is not possible) and become 0.53, 0.34, 0.08, and 0.05 at 0.4 eV relative energy. The relative energy of the CO^+ ions and the electrons is computed in our simulation as a function of altitude from the temperature profiles. The branching ratios are then interpolated between the 0 and 0.4 eV values given above. The rate coefficient used is that measured by *Rosen et al.* [1998],

$$\alpha = 2.75 \times 10^{-7} (300/\mathrm{Te})^{0.55} \ \mathrm{cm}^3\ \mathrm{s}^{-1} \quad (7.4)$$

where Te is the electron temperature. The escape rates are 4.6 x 10^{20} and 4.1 x 10^{22} s^{-1} for solar low and high activity, respectively [*Cipriani et al.* 2007].

The DR mechanisms are expected to have an important contribution to the current escape of the heavier components, such as oxygen atoms (as shown in previous chapters), but also as carbon atoms by recombination of CO_2^+ [*Nagy et al.* 2001; *Fox* 2004; *Cipriani et al.* 2007] and as nitrogen atoms by recombination of N_2^+ [*Brinkman* 1971; *McElroy* 1972; *Fox and Dalgarno* 1983; *Fox* 1993b].

This process is extremely similar to the generation of hot atomic oxygen (see Chapter III) and a complete 3D description for hot carbon is possible using our MTGCM/DSMC model.

VII.2.2. CO_2^+ DR

CO_2^+ DR has been assumed in the past to proceed overwhelmingly by the channel that produces C + O_2. *Fox* [2004] has constructed both low and high solar activity models of the Martian thermosphere, and has tested the effect of including the C + O_2 channel on the production of both thermal and escaping C atoms in the Martian atmosphere. They find that CO_2^+ DR is by far the dominant source of atomic carbon in both models, and its inclusion leads to larger densities of ambient C. The contribution of the source to the escape flux of C, however, is found to be small, both because the altitude profile of the production rate falls off rapidly near the exobase and because the O_2 molecule is probably produced with considerable internal energy.

Similar to the CO+ DR, this mechanism can be easily computed by the MTGCM/DSMC model. While hot atomic carbon escape might not vary, the shape of the hot carbon Martian corona is expected to change significantly.

VII.2.3. CO photodissociation

The photodissociation of CO,

$$CO + h\nu \rightarrow C_{hot} + O_{hot} \quad (7.5)$$

results in excess kinetic energy becoming available to the atomic products, the amount of which depends on the wavelength of the dissociating photon and the electronic state of the dissociation products. The hot C production rates caused by this photodissociation process were calculated by the study of *Nagy et al.* [2001] by assuming that the products were in their ground state and by using the photodissociation cross sections presented by *Fox and Black* [1989]. The solar flux values used were the 79050 and the SC21REFW *Hinteregger et al.* [1981] EUV fluxes, for high and low solar activity, respectively, combined with the X-ray values given by *Ayres* [1997]. The thermospheric models used were similar to those used previously [*e.g. Fox* 1997; *Kim et al.* 1998]. The high solar activity model is based on the Mars Thermospheric General Circulation Model (MTGCM) of *Bougher et al.* [1990], and the specific values used were for near the Equator at 1600 LT. The low solar activity, neutral atmosphere is that from the Viking neutral mass spectrometer results, which correspond to a solar zenith angle of 44 [*Nier and McElroy* 1977; *Fox and Dalgarno* 1979].

The escape rates are 4.3 x 10^{23} and 6.3 x 10^{24} s^{-1} for solar low and high activity, respectively [*Nagy et al.* 2001]. The study of *Fox* [2004] found similar results of 5.3 x 10^{23} and 2.5 x 10^{24} s^{-1} for solar low and high activity, respectively.

The preliminary DSMC results (using similar assumptions) of the density distribution of escaping carbon atoms due to CO photodissociation for the EL case are presented in Figure 7.5.

It can be also noted that photodissociation has been suggested as an important source for the nitrogen escape [*Brinkman* 1971; *Fox and Dalgarno* 1983; *Fox* 1993b] and carbon escape [*Fox and Bakalian* 2001].

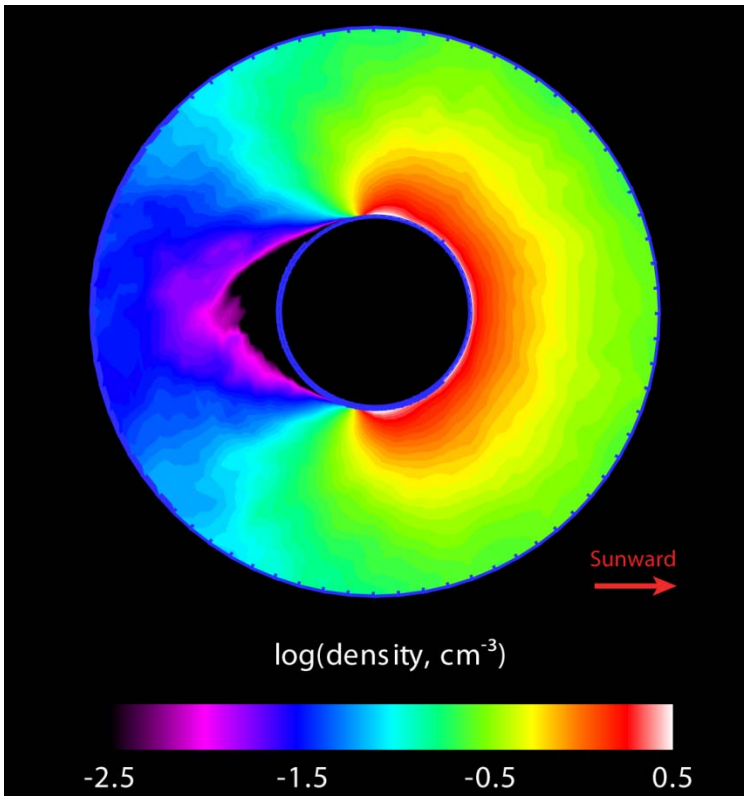

Figure 7.5. Density distribution of escaping carbon atoms due to CO photodissociation for the EL case. The red arrow points toward the Sun.

VII.2.4. Sputtering

Hot carbon loss can also be induced by sputtering. Recent studies report similar escape rates of 8.3 and 8.8 x 10^{22} s^{-1} [*Cipriani et al.* 2007 and *Leblanc and Johnson* 2002, respectively] for the EL case.

This process being strictly similar to the escape of hot oxygen due to sputtering (Section VII.1.3), the same conclusion can be made: a self-consistent 3D model, which would couple thermosphere, exosphere and ionosphere domains is needed to provide a rigorous description of the resulting hot carbon corona.

VII.3. Hydrogen

VII.3.1. Thermal Hydrogen

Hydrogen is lighter than other species of interest (*i.e.* O and C) and its Jean's escape is the major source of hot hydrogen. Jean's approach is a simple way to model escape in 1D. It assumes a fixed density of n_0 at a critical level at r_0, below which the distribution is Maxwellian at a temperature T_0 and above which the domain is colllisionless. The theory is described in Chapter II, while the limitations of the application are discussed in Chapter IV.

The main limitation of the approach is that only the escape flux is provided and not the exospheric densities. As discussed in detail in Chapter IV, the escape rate is very temperature dependent. Since the temperature can vary of a factor x2 from one location to another in the EL case, the difference in the escape flux can be as high as a factor ~150. The density n_0 is also very hard to infer. Indeed, the density of 2.74 x 10^4 cm^{-3} assumed by most of studies is a very rough approximation owing to the fact that they do not include dynamics which has a tremendous effect on such a light species. We showed both theoretically (Chapter II) and computationally (Chapter IV) that it has already an important effect on oxygen.

However, even a 3D model that includes dynamics, such as the MTGCM, cannot compute it presently because of the very important diurnal tide and an artificial hydrogen build up in the nightside. A full coupling with an exospheric model would however solve the problem by allowing an exchange of particles between the boundary of the two models.

VII.3.2. Non-thermal Hydrogen

An interesting recent study [*Kharchenko et al.* 2008] shows that collision with the hot oxygen of the corona is an important source of hot hydrogen in the Martian upper atmosphere, via

$$H + O_{hot} \rightarrow O + H_{hot} \qquad (7.6)$$

A complete computation would require a detailed exospheric description of the hot oxygen atoms, such as the one presented in this work, together with the thermal

distribution of hydrogen in the thermosphere, on which the information available are still very limited today.

Chapter VIII
Conclusions

In this work, the combination of the 3D DSMC kinetic model and the 3D MTGCM is used to provide for the first time a self-consistent 3D description of the Martian upper atmosphere and its variations over long-term and evolutionary timescales.

Previous studies of the Martian hot corona could not incorporate the full effects of realistic upper atmospheric conditions and the spatial distribution of their results based upon the same limitations inherent to the 1D thermosphere/ionosphere inputs. In agreement with the reported modern observations, the 3D calculations of the MTGCM show that important local asymmetries should be taken into account (in addition to the diurnal patterns) for a rigorous description of the upper atmosphere. Local variations in winds, temperatures and background species relative abundances lead to a new perspective on the exobase height determination, atom-to-molecule ratio, and on the ionosphere structure (ion peak height, local ion production), that in turn affect production and collision of hot oxygen atoms, critical exospheric mechanisms at the origin of the hot corona and atmospheric loss.

Asymmetries in thermal and density structure affect more significantly the exospheric distribution closer to the exobase, whereas the comparable and sizeable non-axisymmetric effects of thermospheric winds and planetary rotation are more noticeable farther from it. Isodensity maps illustrate the 3D shape of the Martian hot corona, which is clearly inflated towards the dayside. Rather than an axisymmetric circular shape, the

escape flux of hot oxygen exhibits an oblong shape extended towards the Poles. The computed O escape rate due to O_2^+ DR is 6.0 x 10^{25} s^{-1} and the total O^+ ion production above the ionopause is estimated at 2.2 x 10^{24} s^{-1} for the EL case. Therefore, even in its most generous estimation, the ion loss from ions newly created above the ionopause remains more than an order of magnitude less than the hot oxygen escape due to O_2^+ DR.

Table 8.1. Variations in both magnitude and spatial distribution for themospheric/ionospheric and exospheric parameters due to seasons (comparing aphelion to perihelion), solar cycle (comparing solar low to solar high) and history (comparing epoch 1 to 3)

a. Variations in the thermosphere

		Season (~2 yr)	Solar cycle (~11 yr)	History (~3.5 Gyr)
Temperatures[a]	(ΔT)	small (20 K)	moderate (100 K)	important (190 K)
spatial distribution[b]		*important*	*none*	*small*
Exobase height	(Δz)	moderate (15 km)	moderate (15 km)	important (50 km)
spatial distribution[b]		*important*	*none*	*none*
O density[c]	(n/n0)	moderate (x 1.7-1.8)	moderate (x 1.8-2.0)	important (x 13)
spatial distribution[b]		*important*	*none*	*none*
Ion peak height	(Δz)	moderate (12 km)	none	none
spatial distribution[b]		*important*	*none*	*none*
Electron density[d]	(n/n0)	small (x 1.2)	moderate (x 1.5-1.6)	important (x 2.4)
spatial distribution[b]		*important*	*none*	*none*

b. Variations in the exosphere

		Season (~2 yr)	Solar cycle (~11 yr)	History (~3.5 Gyr)
O density	(n/n_0)	small (x ~1.2)	moderate (x 3)	important (x 14)
spatial distribution[b]		*small*	*none*	*small*
O escape	(φ/φ_0)	small (x 1.6)	moderate (x 3-4)	important (x 6-9)
spatial distribution[b]		*small*	*none*	*none*
O^+ production	(χ/χ_0)		moderate (x 4-5)	important (x ~160)
spatial distribution[b]		*small*	*none*	*none*

[a]results for neutral temperature could be extended to electron and ion temperature if they are assumed tied *Fox et al.* [1996, also private communication 2008].
[b]spatial distribution refers to the angular distribution around the planet in the frame associated with the Sun.
[c]CO_2 density and O mixing ratio can be inferred from the results for O density.
[d]at the ion peak rather than at the exobase altitude.

A brief summary of the variations of the main parameters in the thermosphere/ionosphere and in the exosphere is presented in Table 8.1. The most important conclusion of this work is that spatial, seasonal, solar cycle and evolutionary driven variations are all estimated to be of the same order. For example, the atmospheric

loss is enhanced by a factor about three locally between day and night at 10 Martian radii, by a factor about two between limiting seasonal cases (AL and PL), by a factor about three between the solar cycle equinox cases (EL and EH) and by a factor about nine between present and ~3.5 Gyr ancient thermospheres.

This underlines the importance of taking into account both solar cycle and seasonal effects for a rigorous description of the Martian hot corona and the atmospheric loss for modern conditions. Studying the combined effect of both long-term variations would be useful for future mission planning. The results for modern conditions show that the escape rate varies from 4.6×10^{25} to 2.6×10^{26} s^{-1} between the two extreme cases of net solar forcing (*i.e.* between the AL and PH cases). While the exobase height varies with seasons and solar activity (from 165 to 195 km altitude for the AL and PH case, respectively), the ion peak height varies exclusively with seasons (122 ± 6 km altitude).

The 3D description of the thermosphere/ionosphere by the MTGCM allows a rigorous description the gas system of the Martian upper atmosphere not only at present, but also in the past where solar EUV fluxes were higher. Effects of dynamics are more important for ancient Mars, leading to stronger dynamical cooling on the dayside and heating on the nightside. While the ancient atmospheres are found to be denser and hotter, the variations are not as large as 1D models predicted. The study of the evolution of the heat balance suggests that the ancient Mars thermosphere (of about 3.5 Gyr ago) was relatively similar to the present Venus thermosphere.

The exosphere description by the DSMC model shows that the long-term decay of atmospheric loss due to O_2^+ DR throughout the Martian history (until about 3.5 Gyr ago) may be comparable to the ~22-year periodic variations due to the cumulative effect of solar cycle and orbital position at present. In order to characterize the global loss of water, studies of the ancient upper atmosphere should therefore consider both solar low and high conditions (or at least a solar cycle average in the past) when estimating any EUV dependent process in the Early Mars.

O_2^+ DR is by far the main escape mechanism at present, but its relative contribution may have been reduced in the past compared to secondary escape processes. To address

this, the current study gives conservative estimates of escape by O_2^+ DR and generous estimates of sputtering-related loss and ion production. Despite those considerations, O_2^+ DR is found to remain the main driver of atmospheric escape over this period. The O_2^+ DR escape rate for epoch 3 is estimated to be 5.7 x 10^{26} s^{-1}, corresponding to a total loss of about 10 meters of water to space over the last ~3.5 Gyr. Results before ~3.5 Gyr ago suggest that the bulk of water escape on Mars happened during that early period. However other competing processes (such as thermal escape, impact erosion, etc.) become important at that time and should also be considered.

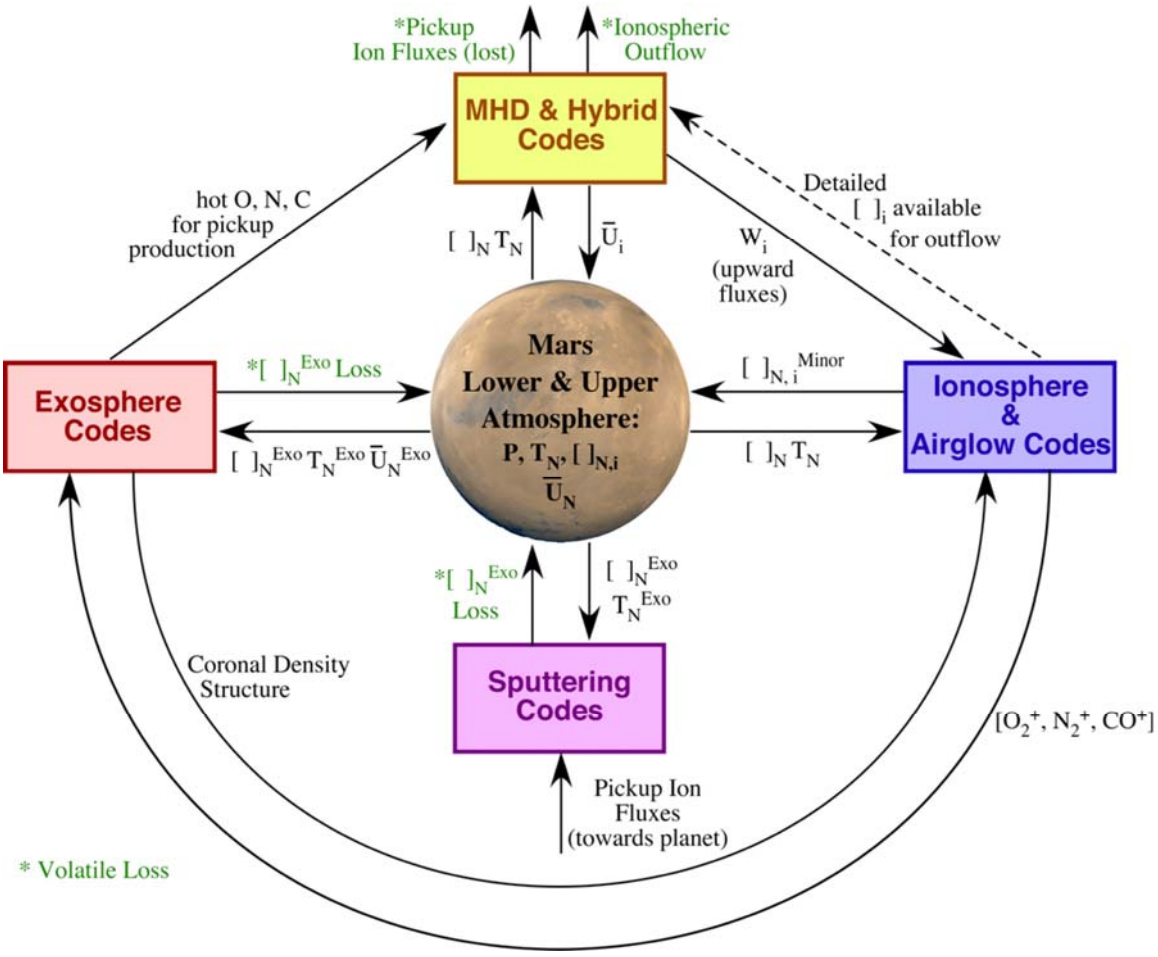

Figure 8.1. Mars upper atmosphere model inter-connections for the simulation of volatile escape rates [Source: *Bougher at al.* 2009b].

Coupled results of the thermosphere/ionosphere with the exosphere, similar to those presented and discussed in this thesis, would be useful for complex 3D plasma models,

since exospheric parameters govern different local ionospheric processes, such as ion loss, atmospheric sputtering and interaction with the solar wind in general (Figure 8.1). It would also permit a better understanding of localized features, such as magnetic crustal fields which can only be modeled in 3D. The combined results of the 3D MTGCM and DSMC are currently being used in the framework of an intercomparison of global models and measurements of the Martian plasma environment, a working group of the International Space Sciences Institute (ISSI) [*Brain et al.* 2008].

References

Acuña, M. H., and 19 colleagues (1998), Magnetic field and plasma observations at Mars: initial results of the Mars Global Surveyor mission, *Science, 279*, 1676-1680.

Anderson, D. E., and C. W. Hord (1971), Mariner 6 and 7 Ultraviolet Spectrometer Experiment: Analysis of hydrogen Lyman-alpha data, *J. Geophys. Res., 76*, 6666–6673.

Anderson, D. E. (1974), Mariner 6, 7 and 9 Ultraviolet Spectrometer Experiment: Analysis of hydrogen Lyman alpha data, *J. Geophys. Res., 79*, 1513–1518.

Angelats i Coll, M., F. Forget, M. A. López-Valverde, and F. González-Galindo (2005), The first Mars thermospheric general circulation model: The Martian atmosphere from the ground to 240 km, *Geophys. Res. Lett., 32*, 4201, doi: 10.1029/2004GL021368.

Ayres, T., Evolution of the solar ionizing flux, *J. Geophys. Res., 102*, 1641, 1997.

Bailey, G. J., and R. Sellek (1990), A mathematical model of the Earth's plasmasphere and its application in a study of He+ at L=3, *Ann. Geophys., 8*, 171-190.

Barabash, S., A. Fedorov, R. R. Lundin, and J.-A. Sauvaud (2007), Martian atmospheric erosion rates, *Science, 315*, 501 – 503, doi:10.1126/science.1134358.

Bell, J. M., S. W. Bougher, and J. R. Murphy (2007), Vertical dust mixing and the interannual variations in the Mars thermosphere, *J. Geophys. Res.*, 112, doi: 10.1029/2006JE002856.

Bertaux, J.-L., F. Leblanc, S. Perrier, E. Quémerais, O. Korablev, E. Dimarellis, A. Reberac, F. Forget,P. C. Simon,S. A. Stern, B. Sandel, and the SPICAM team (2005), Nightglow in the Upper Atmosphere of Mars and Implications for Atmospheric Transport, *Science,* 307, 566, doi: 10.1126/science.1106957.

Bird, G. (1994), Molecular Gas Dynamics and the Direct Simulation of Gas Flows, *Clarendon Press*, Oxford.

Bougher, S. W., and R. E. Dickinson (1988), Mars mesosphere and thermosphere, I, Global mean heat budget and thermal structure, *J. Geophys. Res., 93*, 7325.

Bougher, S. W., R. G. Roble, E. C. Ridley, and R. E. Dickinson (1990), The Mars thermosphere, 2, General circulation with coupled dynamics and composition, *J. Geophys. Res., 95*, 14,811.

Bougher, S. W., S. Engel, R. G. Roble, and B. Foster (1999), Comparative terrestrial Planet thermospheres: 2. Solar cycle variation of global structure and winds at equinox, *J. Geophys. Res., 104*, 16, 591-16, 611, doi: 10.1029/1998JE001019. E7.

Bougher, S. W., S. Engel, R. G. Roble, and B. Foster (2000), Comparative terrestrial Planet thermospheres: 3. Solar cycle variation of global structure and winds at solstices, *J. Geophys. Res.,105*, 17669-17692, doi: 10.1029/1999JE001232, E7.

Bougher, S. W., R. G. Roble, and T. J. Fuller-Rowellm (2002), Simulations of the Upper Atmospheres of the Terrestrial Planets". AGU Monograph: Comparative Aeronomy in the Solar System, *Eds. M. Mendillo*, A. F. Nagy, and J. H. Waite.

Bougher, S. W., S. Engel, D. P. Hinson, and J. R. Murphy (2004), MGS Radio Science electron density profiles: Interannual variability and implications for the neutral atmosphere, *J. Geophys. Res., 109*, doi:10.1029/2003JE002154.

Bougher, S. W., J. M. Bell, J. R. Murphy, P. G. Withers, and M. López-Valverde (2006), Polar warming in the Mars lower thermosphere: Seasonal variations owing to changing insolation and dust distributions, *Geophys. Res. Lett., 33*, doi: 10.1029/2005GL024059. L02203.

Bougher, S. W., P.-L. Blelly, M. Combi, J. L. Fox, I. Mueller-Wodarg, A. Ridley, and R. G. Roble (2008), Neutral upper atmosphere and ionosphere modeling, *Sp. Sci. Rev.*, doi: 10.1007/s11214-008-9401-9.

Bougher, S. W., T. M. McDunn, K. A. Zoldak, and J. M. Forbes (2009a), Solar cycle variability of Mars dayside exospheric temperatures: MTGCM evaluation of underlying thermal balances, *Geophys. Res. Lett.*, doi:10.1029/2008GL036376.

Bougher, S. W., A. Valeille, M. R. Combi, and V. Tenishev (2009b), Solar Cycle and Seasonal Variability of the Martian Thermosphere-Ionosphere and Associated Impacts upon Atmospheric Escape, *ICES*, (under review).

Brain, D., D. M. Holmstrom, A. Boesswetter, S. Bougher, S. Brecht, E. Dubinin, A. Fedorov, M. Fraenz, E. Kallio, A. Nagy, M. Liemohn, Y. Ma, R. Modolo, and H. Nilsson (2008), Intercomparison of Global Models and Measurements of the Martian Plasma Environment, International Team proposal accepted by the International Space Science Institute.

Brecht, S. H. (1997a), Hybrid simulations of the magnetic topology of Mars, *J. Geophys. Res., 102*, 4743-4750.

Brecht, S. H. (1997b), Solar wind proton deposition into the Martian atmosphere, *J. Geophys. Res., 102*, 11,287-11,294.

Breus, T. K., A. M. Krymskii, D. H. Crider, N. F. Ness, D. Hinson, and K. K. Barashyan (2004), Effect of the solar radiation in the topside atmosphere/ionosphere of Mars: Mars Global Surveyor observations, *J. Geophys. Res., 109*, A09310, doi:10.1029/2004JA010431.

Brinkman, R. T. (1971), Mars: Has nitrogen escaped?, *Science, 179*, 944– 945.

Brinkfeldt, K., et al. (2006), First ENA observations at Mars: Solar-wind ENAs on the nightside, *Icarus, 182*, 439–447, doi:10.1016/j.icarus.2005.12.023.

Carlsson, E., et al. (2006), Mass composition of the escape plasma at Mars, *Icarus, 182*, 320– 328.

Carr, M. H. (1996), Water on Mars, *Oxford Univ. Press*, New York.

Carr, M. H. (1999), Retention of an atmosphere on early Mars, *J. Geophys. Res., 104(E9)*, 21,897-21,909.

Chamberlain, J. W. (1963), Planetary coronae and atmospheric evaporation, *Planet. Space Sci., 11*, 901-960.

Chamberlain, J. W., and D. M. Hunten (1987), Book-Review—Theory of Planetary Atmospheres, *Science, 238*, 96.

Chassefière, E., and F. Leblanc (2004), Mars atmospheric escape and evolution; interaction with the solar wind, *Planet. Space Sci., 52*, 1039-1058.

Chassefière, E., F. Leblanc, and B. Langlais (2006), The combined effects of escape and magnetic field histories at Mars, *Planet. Space Sci., 55*, 343–357, doi:10.1016/j.pss.2006.02.003.

Chassefière, E., F. Leblanc, and B. Langlais (2007), The combined effects of escape and magnetic field histories at Mars, *Planet. Space Sci., 55*, 343-357.

Chaufray, J. Y., R. Modolo, F. Leblanc, G. Chanteur, R. E. Johnson, and J. G. Luhmann (2007), Mars solar wind interaction: Formation of the Martian corona and atmospheric loss to space, *J. Geophys. Res., 112*, E09009, doi:10.1029/2007JE002915.

Cipriani, F., F. Leblanc, and J. J. Berthelier (2007), Martian corona: Non thermal sources of hot heavy species, *J. Geophys. Res., 112*, E07001, doi:10.1029/2006JE002818.

Combi, M. (1996), Time-Dependent Gas Kinetics in Tenuous Planetary Atmospheres: The Cometary Coma, *Icarus, 123*, 207.

Cravens, T. E., A. J. Kliore, J. U. Kozyra, and A. F. Nagy (1981), The ionospheric peak on the Venus dayside, *J. Geophys. Res., 86*, 11,323-11329.

Cravens, T. E., J. U. Kozyra, A. F. Nagy, T. I. Gombosi, and M. Kurtz (1987), Electron impact ionization in the vicinity of comets, *J. Geophys. Res., 92*, 7341-7353.

Crider, D., et al. (2000), Evidence of the electron impact ionization in the magnetic pile-up boundary of Mars, *Geophys. Res. Lett., 27*, 45– 48.

Crifo, J., G. A. Loukianov, A. V. Rodionov, and V. V. Zakharov (2005), Direct Monte Carlo and multifluid modeling of the circumnuclear dust coma. Spherical grain dynamics revisited, *Icarus, 176*, 192.

Dennerl, K., C. M. Lisse, A. Bhardwaj,V. Burwitz, J. Englhauser, H. Gunnel, M. Holmstro¨m, F. Jansen, and V. Kharchenko (2006), First observation of Mars with XMM-Newton: High resolution X-ray spectroscopy with RGS, *Astron.Astrophys., 451*, 709–722, doi:10.1051/0004-6361:20054253.

Donahue, M. T. (1995), Evolution of water reservoirs on Mars from D/H ratios in the atmosphere and crust, *Nature, 374*, 432-434.

Dubinin, E., and 39 colleagues (2006), Electric fields within the Martian magnetosphere and ion extraction: ASPERA 3 observations, *Icarus, 182*, 337– 342.

Fang, X., M. W. Liemohn, A. F. Nagy, Y. Ma, D. De Zeeuw, J. U. Kozyra, and T. H. Zurbuchen (2008), Pickup oxygen ion velocity space and spatial distribution around Mars, *J. Geophys. Res., 113*, A02210, doi:10.1029/2007JA012736.

Fang, X., M. W. Liemohn, A. F. Nagy, J. G. Luhmann, and Y. Ma (2009), On the effect of the Martian crustal magnetic field on atmospheric erosion, *Icarus*, doi:10.1016/j.icarus.2009.01.012.

Fillingim, M. O., L. M. Peticolas, R. J. Lillis, D. A. Brain, J. S. Halekas, D. L. Mitchell, R. P. Lin, D. Lummerzheim, S. W. Bougher, and D. L. Kirchner (2007), Model calculations of electron precipitation induced ionization patches on the nightside of Mars, *Geophys. Res. Lett., 34*, L12101, doi:10.1029/2007GL029986.

Forbes, J. M., F. G. Lemoine, S. l. Bruinsma, M. D. Smith, and X. Zhang (2008), Solar flux variability of Mars' exosphere densities and temperatures, *Geophys. Res. Lett.*, 35, doi:10.1029/2007GL031904. L01201.

Fox, J. L., and A. Dalgarno (1979), Ionization, luminosity and heating of the upper atmosphere of Mars, *J. Geophys. Res., 84*, 7315.

Fox, J. L., and A. Dalgarno (1983), Nitrogen escape from Mars, *J. Geophys. Res., 88*, 9027–9032.

Fox, J. L., and J. H. Black (1989), Photodissociation of CO in the thermosphere of Venus, *Geophys. Res. Lett., 16*, 291.

Fox, J.L. (1993a), On the escape of oxygen and hydrogen from Mars, *Geophys. Res. Lett., 20*, 1847-1850.

Fox, J. L. (1993b), The production and escape of nitrogen atoms on Mars, *J. Geophys. Res, 98,* 3297– 3310.

Fox, J. L., P. Zhou, and S. W. Bougher (1996), The Martian thermosphere/ionosphere at high and low solar activities, *Adv. Space Res., 17(11),* 203-218.

Fox, J. L., and A. Hac (1997), Spectrum of hot O at the exobases of the terrestrial planets, *J. Geophys. Res., 102,* 24005.

Fox, J. L., and A. Hac (1999), Velocity distributions of C atoms in CO+ dissociative recombination: Implications for photochemical escape of C from Mars, *J. Geophys. Res., 104*, 24,729-24,737.

Fox, J. L., and K. Y. Sung (2001), Solar activity variations in the Venus thermosphere/ionosphere, *J. Geophys. Res., 106*, 21305-21335.

Fox, J. L., and F. M. Bakalian (2001), Photochemical escape of atomic carbon from Mars, *J. Geophys. Res., 106*, 28,785– 28,795.

Fox, J. L. (2003), Effect of H2 on the Martian ionosphere: Implications for atmospheric evolution, *J. Geophys. Res., 108,* A61223, doi:10.1029/2001JA000203.

Fox, J. L. (2004), CO2 + dissociative recombination: A source of thermal and nonthermal C on Mars, *J. Geophys. Res., 109(A18),* A08306, doi:10.1029/ 2004JA010514.

Gough, D. O. (1981), Solar interior structure and luminosity variations, *Solar Phys., 74*, 21.

Grinspoon, D. H., and J. S. Lewis (1988), Cometary water on Venus: Implications of stochastic impacts, *Icarus, 74*, 21-35.

Guinan, E. F., and I. Ribas (2002), Our changing sun: the role of solar nuclear evolution and magnetic activity on Earth's atmosphere and climate, in: The evolving sun and its influence on planetary environments, *ASP conference series 269*, 85-106.

Gunell, H., et al. (2006), First ENA observations at Mars: Charge exchange ENAs produced in the magnetosheath, *Icarus, 182*, 431– 438, doi:10.1016/j.icarus.2005.10.027.

Haberle, R. M. (1998), Early Mars climate models, *J. Geophys. Res., 103*, 28,467-28,479.

Haberle, R. M., M. M. Joshi, J. R. Murphy, J. R. Barnes, J. T. Schofield, G. Wilson, M. López-Valverde, J. L. Hollingsworth, A. F. C. Bridger, and J. Schaeffer (1999), General circulation model simulations of the Mars Pathfinder atmospheric structure investigation/meteorology data, *J. Geophys. Res., 104*, doi: 10.1029/1998JE900040. E4.

Hanson, W. B., S. Santanini, and D. R. Zuccaro (1977), The Martian ionosphere as observed by Viking retarding potential analyszers, *J. Geophys. Res., 82*, 4351-4363.

Harnett, E. M., and R. M. Winglee (2005), Three-dimensional fluid simulations of plasma asymmetries in the Martian magnetotail caused by the magnetic anomalies, *J. Geophys. Res., 110,* A07226, doi:10.1029/ 2003JA010315.

Hinteregger, H. E., K. Fukui, and B. R. Gilson (1981), Observational, reference and model data on solar EUV, from measurements on AE-E, *Geophys. Res. Lett., 8*, 1147.

Hodges, R. R. (1994), Monte Carlo simulation of the terrestrial hydrogen exosphere, *J. Geophys. Res.*, 99, 23229.

Hodges, R. R. (2000), Distributions of hot oxygen for Venus and Mars, *J. Geophys. Res., 105*, 6971-6981.

Hodges, R. R. (2002), The rate of loss of water from Mars, *Geophys. Res. Lett., 29(3),* 1038, doi:10.1029/2001GL013853.

Huestis, D. L., S. W. Bougher, J. L. Fox, M. Galand, R. E. Johnson, J. I. Moses, and J. C. Pickering (2008), Cross sections and reaction rates for comparative planetary aeronomy, *Space Sci. Rev.,* doi 10.1007/s11214-008-9383-7.

Ichimaru, S. (1973), Basic principles of Plasma Physics – A statistical approach, *W. A. Benjamin, Inc.*, Reading, MA.

Ip, W. H. (1990), The fast atomic oxygen corona extent of Mars, *Geophys. Res. Lett., 17*, 2289-2292.

Jakosky, B. M., and R. J. Phillips (2001), Mars volatile and climate history, *Nature, 412*, 237-244.

Johnson, R. E. (1990), Energetic Charged-Particle Interaction With Atmospheres and Surfaces, *Springer*, New York.

Johnson, R. E., and M. Liu (1996), The loss of the atmosphere from Mars, *Science, 274*, 1932–1933.

Johnson, R. E., and J. G. Luhmann (1998), Sputter contribution to the atmospheric corona on Mars, *J. Geophys. Res., 103*, 3649-3653.

Kallio, E., and P. Janhunen (2002), Ion escape from Mars in a quasi-neutral hybrid model, *J. Geophys. Res., 107(A3)*, 1035, doi:10.1029/2001JA000090.

Kallio, E., et al. (2006), Ion escape at Mars: Comparison of a 3-D hybrid simulation with Mars Express IMA/ASPERA-3 measurements, *Icarus, 182*, 350– 359, doi:10.1016/j.icarus.2005.09.018.

Kaneda, K., N. Terada, and S. Machida (2007), Time variation of nonthermal escape of oxygen from Mars after solar wind dynamic pressure enhancement, *Geophys. Res. Lett., **34***, doi:10.1029/2007GL030576 1038.

Kaneda, K., N. Terada, and S. Machida (2009), Solar-wind control of the hot-oxygen corona around Mars, *Geophys. Res. Lett., 114*, doi:10.1029/2008JE003234.

Kar, J., K. K. Mahajan, and R. Kohli (1996), On the outflow of O2 + ions at Mars, *J. Geophys. Res., 101*, 12,747–12,752.

Kass, D. M., and Y. L. Yung (1995), The loss of atmosphere from Mars due to solar wind-induced sputtering, *Science, 268*, 697– 699.

Kass, D. M., and Y. L. Yung (1996), The loss of atmosphere from Mars: Response, *Science, 274*, 1932–1933.

Kella, D., P. J. Johnson, H. B. Pederson, L. Vejby-Christensen, and L. H. Andersen (1997), The source of green light emission determined from a heavy-ion storage ring experiment, *Science, 276*, 1530-1533.

Kharchenko, V., A. Dalgarno, B. Zygelman, and Y.-H. Yee (2000), Energy transfer in collisions of oxygen atoms in the terrestrial atmosphere, *J. Geophys. Res., 105*, 24,899-24,906.

Kharchenko, V., P. Zhang, and A. Dalgarno (2008), Energy and Momentum Relaxation in Collisions of Fast H Atoms with the Atmospheric H and O Gas, Eos Trans. AGU, 89(53), Fall Meet. Suppl., Abstract P11A-1250.

Kim, J., A. F. Nagy, J. L. Fox, and T. E. Cravens (1998), Solar cycle variability of hot oxygen atoms at Mars, *J. Geophys. Res., 103*, 29339-29342.

Kim, Y. H., S. Son, Y. Yi, and J. Kim (2001), A non-spherical model for the hot oxygen corona of Mars, *J. Kor. Ast. Soc., 34*, 25-29.

Krasnopolsky, V. A. (2002), Mars' upper atmosphere and ionosphere at low, medium, and high solar activities: Implications for evolution of water, *J. Geophys. Res., 107*, 5128, doi:10.1029/2001JE001809.

Krestyanikova, M. A., and V. I. Shematovitch, (2005), Stochastic models of hot planetary and satellite coronas: A photochemical source of hot oxygen in the upper atmosphere of Mars, *Sol. Syst. Res., 39*, 22-32.

Lammer, H., and S. J. Bauer (1991), Nonthermal atmospheric escape from Mars and Titan, *J. Geophys. Res., 96*, 1819-1825.

Lammer, H., W. Stumptner, and S. J. Bauer (2000), Upper limits for the Martian exospheric number density during the planet B/Nozomi mission, *Planet. Space Sci., 48*, 1473-1478.

Lammer, H., H. I. M. Lichtenegger, C. Kolb, I. Ribas, E. F. Guinan, R. Abart, and S. J. Bauer (2003), Loss of water from Mars, implications for the oxidation of soil, *Icarus, 165*, 9-25.

Leblanc, F., and R. E. Johnson (2001), Sputtering of the Martian atmosphere by solar wind pick-up ions, *Planet. Space Sci., 49*, 645-656.

Leblanc, F., and R. E. Johnson (2002), Role of molecular species in pickup ion sputtering of the Martian atmosphere, *J. Geophys. Res., 107(E2) (5)*, 1-6.

Leblanc, F., J. Y. Chaufray, J. Lilensten, O. Witasse, and J.-L. Bertaux (2006), Martian dayglow as seen by the SPICAM UV spectrograph on Mars Express, *J. Geophys. Res., 111*, doi:10.1029/2005JE002664.

Lichtenegger, H. I. M., H. Lammer, D. F. Vogl, and S. J. Bauer (2004), Temperature effects of energetic neutral hydrogen on the Martian exosphere, *Adv. Space Res., 33*, 140– 144.

Lichtenegger, H. I. M. , H. Lammer, Y. N. Kulikov, S. Kazeminejad, G. H. Molina-Cuberos, R. Rodrigo, B. Kazeminejad and G. Kirchengast (2007), Effects of Low Energetic Neutral Atoms on Martian and Venusian Dayside Exospheric Temperature Estimations, *Space Sci. Rev., 126*, 469-501.

Liu, J., M. I. Richardson, and R. J. Wilson (2003), An assessment of the global, seasonal, and interannual spacecraft record of Martian climate in the thermal infrared, *J. Geophys. Res., 108*, doi: 10.1029/2002JE001921. E8.

López-Valverde, M. A., D. P. Edwards, M. López-Puertas, and C. Roldán (1998), Non-local thermodynamic equilibrium in general circulation models of the Martian atmosphere 1. Effects of the local thermodynamic equilibrium approximation on thermal cooling and solar heating, *J. Geophys. Res., 103*, 16,799-16,812.

Luhmann, J. G., and J. U. Kozyra (1991), Dayside pickup oxygen precipitation at Venus and Mars: Spatial distributions, energy deposition and consequences, *J. Geophys. Res, 96*, 5457–5468.

Luhmann, J. G., R. E. Johnson, and M. H. G. Zhang (1992), Evolutionary impact of sputtering of the Martian atmosphere by O+ pick-up ions, *Geophys. Res. Lett., 19*, 2151–2154.

Luhmann, J. G. (1997), Correction to "The ancient oxygen exosphere of Mars: Implications for atmosphere evolution" by Zhang et al., *J. Geophys. Res., 102(E1),* 1637.

Lundin, R., A. Zakharov, R. Pellinen, H. Borg, B. Hultqvist, N. Pissarenko, E. M. Dubinin, S. W. Barabash, I. Liede, and H. Koskinen (1989), First measurements of the ionospheric plasma escape from Mars, *Nature, 341*, 609-612.

Lundin, R., and S. Barabash (2004), Evolution of the Martian atmosphere and hydrosphere: Solar wind erosion studied by ASPERA-3 on Mars Express, *Planet. Space Sci., 52*, 1059– 1071.

Lundin, R., et al. (2006), Ionospheric plasma acceleration at Mars: ASPERA-3 results, *Icarus, 182*, 308–319.

Lundin, R., S. Barabash, M. Holmström, H. Nilsson, M. Yamauchi, M. Fraenz, and E. M. Dubinin (2008), A comet-like escape of ionospheric plasma from Mars, *Geophys. Res. Lett., 35*, L18203.

Ma, Y., A. F. Nagy, K.C. Hansen, D.L. De Zeeuw, and T.I. Gombosi (2002), Three-dimensional multispecies MHD studies of the solar wind interaction with Mars in the presence of crustal fields, *J. Geophys. Res., 107*, 1282-1289, doi:10.1029/2002JA009293.

Ma, Y., A. F. Nagy, I.V. Sokolov, and K.C. Hansen (2004), Three-dimensional, multispecies, highspatial resolution MHD studies of the solar wind interaction with Mars, *J. Geophys. Res., 109*, doi:10.1029/2003JA010367.

Ma, Y., and A. F. Nagy (2007), Ion escape fluxes from Mars, *Geophys. Res. Lett., 34*, L08201, doi:10.1029/2006GL029208.

McElroy, M. B. (1972), Mars: An evolving atmosphere, *Science, 175*, 443– 445.

McElroy, M. B., T. Y. Kong, Y. L. Yung, and A. O. Nier (1976), Composition and structure of the Martian upper atmosphere: Analysis of results from Viking, *Science, 194*, 1295-1298.

Mehr, F. J., and M. A. Biondi (1969), Electron Temperature Dependence of Recombination of O_2^+ and N_2^+ Ions with Electrons, *Physical Review 181*, 264-271, doi: 10.1103/Physrev.181.264.

Markelov, G., Y. Skorov, and H. Keller (2006), DSMC Modeling of Dusty Innermost Cometary Atmosphere Around Non-Spherical Nucleus, *AIAA*, 2006-3392.

Martin, L. J. (1984), Clearing the Martian air: The troubled history of dust storms, *Icarus, 57*, 317.

McElroy, M. B., T. Y. Kong, and V. L. Yung (1977), Photochemistry and evolution of Mars' atmosphere: A Viking perspective, *J. Geophys. Res., 82*, 4379.

Melosh, H. J., and A. M. Vickery (1989), Impact erosion of the primordial atmosphere of mars, *Nature, 338*, 487-489.

Modolo, R., G. M. Chanteur, E. Dubinin, and A. P. Matthews (2005), Influence of the solar activity on the Martian plasma environment, *Ann. Geophys., 23*, 433-444.

Morgan, D. D., D. A. Gurnett, D. L. Kirchner, J. L. Fox, E. Nielsen, and J. J. Plaut (2008), Variation of the Martian ionospheric electron density from Mars Express radar soundings, *J. Geophys. Res., 113*, doi:10.1029/2008JA013313.

Nagy, A. F., and P. M. Banks (1970), Photoelectron fluxes in the ionosphere, *J. Geophys. Res., 75*, 6260-6270.

Nagy, A. F., T. E. Cravens, J. H. Yee, and A. I. F. Stewart (1981), Hot oxygen atoms in the upper atmosphere of Venus, *Geophys. Res. Lett., 8*, 629-632.

Nagy, A. F., and T. E. Cravens (1988), Hot oxygen atoms in the upper atmosphere of Venus and Mars, *Geophys. Res. Lett., 15*, 433-435.

Nagy, A. F., J. Kim, and T. E. Cravens (1990), Hot hydrogen and oxygen atoms in the upper atmosphere of Venus and Mars, *Ann. Geophys., 8*, 251-256.

Nagy, A. F., M. W. Liemohn, J. L. Fox, and J. Kim (2001), Hot carbon densities in the exosphere of Mars, *Geophys. Res. Lett., 82*, 4341-4349.

Nagy, A. F., et al. (2004), The plasma environment of Mars, *Space Sci. Rev., 111*, 33–114, doi:10.1023/B:SPAC.0000032718.47512.92.

Newkirk Jr., G. (1981), Solar variability on time scales of 105 years to 109.6 years. Geochim. Cosmochim, *Acta Suppl., 13*, 293-301.

Nier, A. O., and M. B. McElroy (1977), Composition and structure of Mars' upper atmosphere: Results from the neutral mass spectrometers on Viking 1 and 2, *J. Geophys. Res., 82*, 4341-4349.

Opik, E. J., and S. F. Singer (1959), distribution of density in a planetary exosphere, *Phys. Fluids, 2*, 653-655.

Opik, E. J., and S. F. Singer (1961), distribution of density in a planetary exosphere II, *Phys. Fluids, 4*, 221-233.

Peverall, R., S. Rosén, J. R. Peterson, M. Larsson, A. Al-Khalili, L. Vikor, J. Semaniak, R. Bobbenkamp, A. Le Padellec, A. N. Maurellis, and W. J. van der Zande (2001), Dissociative recombination and excitation of O_2^+: Cross sections, product yields and implications for studies of ionospheric airglows, *J. Chem. Phys., 114*, 6679-6689.

Podladchikova, T., B. Lefebvre, and R. A. M. Van der Linden (2008), Integral activity of the declining phase of sunspot cycles as precursor of the next cycle, *Journal of Atmospheric and Solar-Terrestrial Physics, 70*, 277-284.

Quémerais, E., R. Lallement, S. Ferron, D. Koutroumpa, J.-L. Bertaux, E. Kyrola, and W. Schmidt (2006), Interplanetary hydrogen absolute ionization rates: Retrieving the solar wind mass flux latitude and cycle dependence with SWAN/SOHO maps, *J. Geophys. Res., 111*, A09114, doi:10.1029/2006JA011711.

Ribas, I., E. F. Guinan, M. Gudel, and M. Audard (2005), Evolution of the Solar Activity over time and effects on planetary atmospheres. I. High-energy irradiances (1-1700 A), *The Astrophys. J.*, 622:680-694.

Rosen, S., R. Peverall, and M. Larsson, et al. (1998), Absolute cross sections and final-state distributions for dissociative recombination and excitation of CO+, using an ion storage ring, *Phys. Rev. A, 57*, 4462– 4470.

Schunk, R. W., and A. F. Nagy (2009), Ionospheres, *Cambridge Univ. Press*, New York.

Selsis, F., H. Lammer, I. Ribas, E. F. Guinan, H. I. M. Lichtenegger, L.-M. Lara, M. G. Tehrany, A. Hanslmeier (2002), Radiation and particle exposure of the Martian paleoatmosphere: Implications for the loss of water. Proceedings of the second European workshop on exo/astrobiology, Graz, Austria, *ESA SP, Vol. 518*, 553-554.

Shen, C. S. (1963), An analytic solution for density distribution in a planetary exosphere, *J. Atm. Sciences, 20*, N. 2 p69-72.

Smith, M. D. (2004), Interannual variability in TES atmospheric observations of Mars during 1999-2003, *Icarus, 167*, 148-65.

Solomon, S. C., and 15 colleagues (2005), New perspectives on ancient Mars, *Science, 307*, 1214-1220.

Stebbings, R. F., A. C. H. Smith, and H. Erhardt (1964), Charge transfert between oxygen atoms and O+ and H+ ions, *J. Geophys. Res., 69*, 2349.

Stewart, A. I. F. (1987), Revised time dependent model of the martian atmosphere for use in orbit lifetime and sustenance studies. LASP-JPL Internal Rep., PO# NQ-802429, Jet Propulsion Laboratory, Pasadena, CA.

Stewart, A. I. F., M. J. Alexander, R. R. Meier, L. J. Paxton, S. W. Bougher, and C. G. Fesen (1992), Atomic Oxygen in the Martian Thermosphere, *J. Geophys. Res., 97(A1)*, 91-102.

Tenishev, V., and M. R. Combi (2005), Monte-Carlo model for dust/gas interaction in rarefied flows, *AIAA*, 2005-4832.

Tenishev, V., M. R. Combi, and B. Davidsson (2008), A Global Kinetic model for cometary comae. The evolution of the coma of the Rosetta target comet Churyumov-Gerasimenko A Global Kinetic model for cometary comae. The evolution of the coma of the Rosetta target comet Churyumov-Gerasimenko throughout the mission, *Astrophys. J., 685*, 659-677.

Tian, F., J. F. Kasting, S. C. Solomon (2009), Thermal escape of carbon from the early martian atmosphere, *Geophys. Res. Lett.*, doi:10.1029/2008GL036513, in press.

Tobiska, W. K., T. Woods, F. Eparvier, R. Viereck, L. Floyd, D. Bouwer, G. Rottman, and O. R. White (2000), The SOLAR2000 empirical solar irradiance model and Forecast tool, *J. Atmos. Sol. Phys., 62*, 1233-1250.

Torr, M. R., and D. G. Torr (1985), Ionization frequencies for solar cycle 21: Revised, *J. Geophys. Res, 90*, 6675.

Trotignon, J. G., C. Mazelle, C. Bertucci, and M. H. Acuña (2006), Martian shock and magnetic pile-up boundary positions and shapes determined from Phobos 2 and Mars Global Surveyor data sets, *Planet. Space Sci., 54*, 357-369.

Valeille, A., M. R. Combi, V. Tenishev, S. W. Bougher, and A. F. Nagy (2009a), A study of suprathermal oxygen atoms in Mars upper thermosphere and exosphere over the range of limiting conditions, *Icarus*, doi:10.1016/j.icarus.2008.08.018.

Valeille, A., S. W. Bougher, V. Tenishev, M. R. Combi, and A. F. Nagy (2009b), Water loss and Evolution of the upper atmosphere and exosphere over Martian History, *Icarus*, in press.

Valeille, A., V. Tenishev, S. W. Bougher, M. R. Combi, and A. F. Nagy (2009c), 3D study of Mars upper-thermosphere/ionosphere and hot corona: (1) General description and results at equinox for solar minimum conditions, *J. Geophys. Res.*, under review.

Valeille, A., M. R. Combi, S. W. Bougher, V. Tenishev, and A. F. Nagy (2009d), 3D study of Mars upper-thermosphere/ionosphere and hot corona: (2) Solar cycle, seasonal variations and evolution over history, *J. Geophys. Res.*, under review.

Verigin, M. I., et al. (1991), Ions of planetary origin in the Martian magnetosphere (Phobos 2/TAUS experiment), *Planet. Space Sci., 39*, 131– 137.

Walker, J. C. G. (1987), Impact erosion of planetary atmospheres, *Icarus, 68*, 87-98.

Withers, P. and M. Mendillo (2005), Response of peak electron densities in the Martian ionosphere to day-to-day changes in solar flux due to solar rotation, *Planet. Space Sci., 53*, 1401-1418, doi:10.1016/j.pss.2005.07.010.

Wood, B. E., H.-R. Muller, G. P. Zank, and J. L. Linsky (2002), Measured mass-loss rates of solar-like stars as a function of age and activity, *Astrophys. J., 574*, 412-425.

Zahnle, K. J., and J. C. G. Walker (1982), The evolution of solar ultraviolet luminosity, *Rev. Geophys., 20*, 280-292.

Zahnle, K. J., R. M. Haberle, D. C. Catling, and J. F. Kasting (2008), Photochemical instability of the ancient Martian atmosphere, *J. Geophys. Res., 113(E11004)*, doi:10.1029/2008JE003160.

Zhang, M. H. G., J. G. Luhmann, and A. J. Kliore (1990), An observational study of the nightside ionospheres of Mars and Venus with radio occultation methods, *J. Geophys. Res., 95*, 17095-17102.

Zhang, M. H. G., J. G. Luhmann, and A. F. Nagy (1993a), Oxygen ionization rates at Mars and Venus: Relative contributions of impact ionization and charge exchange, *J. Geophys. Res., 98(E2)*, 3,311-3,318.

Zhang, M. H. G., J. G. Luhmann, S. W. Bougher, and A. F. Nagy (1993b), The ancient oxygen exosphere of Mars: Implications for atmosphere evolution, *J. Geophys. Res., 98*, 10,915-10,923.